Multi-Channel Analysis of Surfaces Wave (MASW) Measurements using Random Receiver Arrays as Applied for Future Lunar Exploration

A Dissertation presented for
the Doctor of Philosophy
Degree
The University of Tennessee-Knoxville

Prasanta Malati Yeluru
December 2012

Multi-Channel Analysis of Surfaces Wave (MASW) Measurements using Random Receiver Arrays as Applied for Future Lunar Exploration

Approved by:

Dr. Gregory S Baker (primary advisor)
Department of Earth and Planetary Sciences
University of Tennessee-Knoxville

Dr. Edmund A Perfect
Department of Earth and Planetary Sciences
University of Tennessee-Knoxville

Dr. Lawrence A Taylor
Department of Earth and Planetary Sciences
University of Tennessee-Knoxville

Dr. Dayakar Penumadu
Department of Civil and Environmental Engineering
University of Tennessee-Knoxville

Date Approved:

DEDICATION

To my husband, daughter and family

ACKNOWLEDGMENTS

I would like to express my sincere gratitude to my advisor, Dr. Gregory S Baker for giving me the opportunity to perform the degree and also for his guidance and support during my doctoral studies. I have benefited tremendously from his experience and clear thought in the research. He has provided for me not only his knowledge but also his deep and kind consideration.

I would like to thank the other members of my committee, Dr. Ed Perfect, Dr. Larry Taylor and Dr. Dayakar Penumadu for their valuable comments and suggestions.

I would also like to thank: Dr. Choon Park for passing to me much of his knowledge of surface wave methods; Dr. George McMechan, University of Texas-Dallas for his ultimate support and for providing me with access to work in his lab; Megan Carr, David Gaines, Rachel Storniolo, Caitlyn Williams and Matt Edmunds for their friendships.

I am deeply indebted to my parents, parents-in-law, and family for their patience, understanding and encouragement. Finally and above all, I would like to thank my husband, Phaniveer Koti and daughter, Snigdha Lahari koti for their love, support, encouragement and smile during this difficult time. They have made this possible.

And most of all, I thank the almighty for His countless blessings bestowed upon me and guided me throughout my educational journey.

ABSTRACT

The geology of Earth's moon has previously been examined via telescopic observations, orbiting spacecraft readings, lunar sample analysis, and also from some geophysical data. Previous researchers have examined layering of the moon and models exist explaining the velocity variations in the mantle and core. However, no studies (or datasets) currently exist regarding the engineering properties of the shallow (<30 m) lunar subsurface. Engineering properties--like shear modulus and Poisson's ratio--are key parameters for civil engineering works, as they characterize the mechanical behavior of geotechnical materials under various types of loading. Therefore, understanding the physical and engineering properties within the upper 30 m of the lunar subsurface will be critical for lunar exploration if deployment of large structures, large-scale excavation, and/or landing of large spacecraft on the surface is desired. Advances in near-surface geophysical techniques, such as Multi-channel Analysis of Surface Wave (MASW), has greatly increased our ability to map subsurface variations in physical properties. The MASW method involves deployment of multiple seismometers to acquire 1-D or 2-D shear wave velocity profiles that can be directly related to various engineering properties. The advantage of this technique over drilling boreholes or any other geophysical technique is that it is less intensive, non-invasive, more cost-effective, and more robust because strong surface-wave records are almost guaranteed. In addition, data processing and analysis is fairly straightforward, and the MASW method allows for analysis of a large area of interest as compared to drilling boreholes. A new scheme using randomly distributed geophones (likely deployed from a mortar-type device) instead of a conventional linear array will be presented. A random array is necessary for lunar exploration because of the logistical constraints involved in deploying a linear or circular array robotically or by astronaut. Initial results indicate that robust dispersion curves (and thus subsurface models of engineering properties) can be obtained from the random array geometry. This random geometry will also be evaluated (a) for potential improvements in the resolution of the dispersion image and (b) as more accurate method for assessing azimuthal variations in the subsurface geology. Based on the extreme logistics imposed by lunar exploration and the anticipated engineering needs of lunar exploration, information obtained on the moon using this technique should prove to be a critical component of data acquisition.

TABLE OF CONTENTS

Acknowledgements iv

Abstract v

List of Tables ix

List of Figures xv

Chapter I: Introduction **1**
- 1.1 Motivation 2
- 1.2 Research Objectives 2
- 1.3 Dissertation Outline 4
- 1.4 Significance of Study 5

Chapter II: Rayleigh wave in Vertically Heterogeneous Media **7**
- 2.1 Introduction 8
- 2.2 Characteristics of Body and Surface Waves 8
- 2.3 Rayleigh Waves in a Homogeneous Half-Space 11
  - 2.3.1 Rayleigh Wave Equation 11
  - 2.3.2 Displacements due to Rayleigh Waves 19
- 2.4 Rayleigh Waves in Layered Media 21
  - 2.4.1 Dispersion Equation 21
  - 2.4.2 Phase Velocities of Rayleigh Waves 24

Chapter III: Multi-channel Analysis of Surface Waves (MASW) **27**
- 3.1 Introduction 28
- 3.2 Historical Context of the Surface-Wave Method 29
  - 3.2.1 Two-Receiver Approach (The SASW Method) 31
  - 3.2.2 The Multi-Channel Approach (The MASW Method) 33
- 3.3 Advantages of MASW 35
- 3.4 Overall MASW Procedure 36
  - 3.4.1 Data Acquisition 37
  - 3.4.2 Data Analysis-Processing 41
  - 3.4.3 Data Analysis-Inversion 43
- 3.5 Types of MASW Methods 45
  - 3.5.1 Why Passive Method? 46
  - 3.5.2 Types of Passive MASW Method 47
- 3.6 Summary 50

Chapter IV: Physical Properties of the Moon **51**
4.1 Introduction 52
4.2 Geologic History of the Moon 52
4.3 Lunar Landscape 53
4.3.1 The Higlands 53
4.3.2 The Maria 53
4.3.3 Impact Craters 54
4.4 The Lunar Regolith 55
4.5 Summary 69

Chapter V: Exploring Multi-channel Analysis of Surface Waves with Random receiver Arrays for Potential Lunar Exploration **70**
Abstract 71
5.1 Introduction 72
5.2 Overview of MASW Method 74
5.3 MASW Data Collected for Random Receiver Arrays 76
5.4 MASW Data Acquired from Linear Receiver Arrays 79
5.5 Comparison of the Dispersion Results 79
5.6 Statistical Analysis 82
5.7 Discussions and Conclusions 87

Chapter VI: Comparison of Seismic Surface Wave Dispersion Results Obtained from Conventional Versus Random Receiver Arrays **89**
Abstract 90
6.1 Introduction 91
6.2 Site Description-Geologic Setting 92
6.3 Data Acquisition and Analysis 93
6.4 Results 106
6.5 Statistical Analysis 111
6.6 Conclusions 112

Chapter VII: Forward Modeling Experiments for Dispersion ZCurve Resolution Pertaining to Random Array MASW **116**
Abstract 117
7.1 Introduction 118
7.2 Modeling Program Overview 120
7.3 Theory of Surface Wave Properties 121
7.4 Considerations for Numerical Simulations 122
7.5 Sensitivity of the Modeling Software 124
7.6 Analytical Considerations for Dispersion Curve Analysis 125
7.7 Modeling Results 128
7.7.1 Clustered Array Results 128
7.7.2 Skewness Effect 132
7.7.3 Total Number of Traces 134

7.8 Discussion 137
7.9 Conclusions 137

Chapter VIII: Adapting A Random-Array Acquisition Scheme For A Seismic Surface-Wave Study Of A Lunar Analog Site At Black Point Lava Flow, Arizona USA, As A Potential Rover-Friendly Methodology 138
Abstract 139
8.1 Introduction 140
8.2 Lunar Analog Sites for Seismic Studies 141
8.3 Geologic Setting-Black Point Lava Flow Site 143
8.4 Field Test Procedure 146
8.4.1 Data Acquisition 147
8.4.2 Data Analysis-Dispersion 149
8.4.3 Data Analysis-Inversion 150
8.4.4 Data Interpretation 154
8.5 Conclusions 156

Chapter IX: Summary, Conclusions and Future Work 159
9.1 Summary and Conclusions 160
9.1.1 Random Array Analysis 161
9.1.2 Comparison of Various Geophone Arrays 162
9.1.3 Forward Modeling Experiments 163
9.1.4 Application of Random Array MASW 163
9.2 Overall Conclusions and Implication of Research 164
9.3 Future Work 165

References 166

Appendix A

Appendix B

Appendix C

Vita

LIST OF FIGURES

Figure 1	Body waves ((a) and (b)) and surface waves ((c) and (d)) (modified from Bolt, 1993)	10
Figure 2	Cartesian coordinate system	11
Figure 3	Coordinate system in a homogeneous half-space	15
Figure 4	Ratio of VR to VS with Poisson's ratio. It compares the estimated values of VR to the values from the Rayleigh wave equation	19
Figure 5	Vertical and horizontal displacements of Rayleigh waves in homogeneous half-space media (after Richart et.al., 1970)	21
Figure 6	Vertical particle motions of two Rayleigh waves with different wavelengths (Rix, 2000)	24
Figure 7	Steady state methods from 1950's.	30
Figure 8	The Continuous Surface Wave method (Mathew et al., 1996)	30
Figure 9	Schematic representing overall SASW field procedure (Modified from Rix.et.,al 1991)	32
Figure 10	The apparent dispersion concept in SASW method (modified from O'Neill 2004)	32
Figure 11	A field record showing reflections signals hidden by strong surface waves in raw data are seen after filtering	34
Figure 12	Summary of work performed by Gabriels et.al., (1987) (modified from www.masw.com/History-MASW.html)	35
Figure 13	Schematic representation of the active MASW field survey (modified from Park, 2003)	38
Figure 14	Typical field layout for passive remote (left) and passive roadside (right) MASW surveys	47
Figure 15	Examples of 2-D receiver arrays for the passive remote MASW surveys	49
Figure 16	Typical multichannel seismic surface-wave experiment setup and MASW data processing procedure (modified from Park, 1999)	75
Figure 17	The shot point locations as deployed on the ground and the random	77

arrangement of geophones (small circles) inside a 10 m×10 m grid.
Figure 18 Selected data (shot gathers) acquired from a field test site in the University of Tennessee agricultural center, Knoxville, Tennessee, with 48-channel system and their corresponding dispersion images 80
Figure 19 (a) Selected data (shot gathers) acquired from the same field site as above using linear receiver array configuration in East-West direction. (b) Selected data (shot gathers) acquired from the same field site as above using linear receiver array configuration in North-South direction. 81
Figure 20 Comparison of dispersion relation from linear and random receiver array measurements. 82
Figure 21 (a) Figure showing the locations of receivers with x and y coordinates. (b) Surface plot generated from SAS program. (c) Semivariogram calculated using the velocity values as a geologic measurement obtained from various shot points. The statistical parameters like sill, range and nugget are also calculated. (d) Gaussian model is used to fit the variogram. (e) Final surface plot as obtained from the point kriging interpolation method. 85
Figure 22 2-D models obtained for each shot point location using the spatial data. The x-and y axis represents the E-W and N-S directions respectively. 86
Figure 23 Location of the University of Tennessee Agricultural Extension Center, Knoxville, TN 93
Figure 24 The shot point locations as deployed on the ground and the random arrangement of geophones (small circles) inside a 10 m×10 m grid 95
Figure 25 Shot gathers for various arrays. The x-axis represents offset (m) and trace numbers and y-axis represents time (ms). 97
Figure 26 (a) Schematic representation of various array designs as deployed in the field. The x-axis represents E-W and y-axis represents the N-S directions 98
(b) Schematic representation of four different random arrays 99

(different receiver spacing with different x and y coordinates) as deployed on the ground in a 10 by 10 m grid. The x-axis represents E-W and y-axis represents the N-S directions.

Figure 27 Schematic representation of steps involved in data processing and analysis 100

Figure 28 (a) Dispersion images for conventional Linear (EW and NS), Cross, and Circular receiver arrays. The x-axis represents Frequency (Hz) and Y-axis represents Phase Velocity (m/s). 102

(b) Dispersion images for four different random receiver arrays. The x-axis represents Frequency (Hz) and Y-axis represents Phase Velocity (m/s). 103

Figure 29 A graph representing dispersion curve comparison for four types of receiver arrays. 104

Figure 30 Comparison of dispersion curves for various random array distributions. 104

Figure 31 Schematic graphs representing dispersion picks split up into 10-20 Hz and 15-40 Hz to observe the differences within the dispersion picks for clarity. 105

Figure 32 (a) 1-D shear wave velocity profiles based on various conventional and random receiver arrays. 109

(b) 1-D shear wave velocity profiles for various random arrays obtained by inverting the phase velocity picks 109

Figure 33 1-D shear wave velocity profiles for conventional and random arrays calculated from the dispersion curve picks. 110

Figure 34 Graphical comparison of four different random array1-D Vs profiles 110

Figure 35 (a) Schematic stratigraphic column representing various soil layers with approximate depths (in meters) as obtained from the bedrock core-hole log data. Four basic Lithologic units have been identified from the multilevel piezometer that was installed in bedrock hole. 111

(b) All four 1-D Vs profiles shown together for close comparison. 111

Figure 36 Typical multichannel seismic surface-wave experiment setup 119
Figure 37 A layered earth model and corresponding parameters of compressional wave velocity (Vp), shear-wave velocity (Vs), and density. 124
Figure 38 Graph representing correlation between the field and modeled data. The x-axis represents shear-wave velocity (m/s) and y-axis represents depth (m). 125
Figure 39 Flow chart explaining step-by step process of modeling shot gathers 127
Figure 40 Four different cluster array geometries used in the modeling. The x-axis represents the E-W direction and y-axis represents the N-S direction 129
Figure 41 Shot gathers and corresponding dispersion images obtained for four different clustered arrays. The X-axis represents frequency range 1-100 Hz and Y-axis represents phase velocity range 10-3000 m/s 130
Figure 42 Graphical setup for the geophone coordinates as deployed around the grid for normal, left and right skewed data. The star represents the source location (at origin) in all three cases. 133
Figure 43 Shot gathers for Normal, Left and Right skewed models and their corresponding dispersion images. The X-axis on the dispersion image represents frequency (Hz) range 1-100 Hz and the Y-axis represents phase velocity (m/s) range 10-3000 m/s 135
Figure 44 Modeled shot gathers and corresponding dispersion images for different number of channels. The X-axis represents frequency range 1-100 Hz and Y-axis represents phase-velocity range 10-3000 m/s 136
Figure 45 (a) Sunset crater and the Black Point Lava Flow (BPLF), north of Flagstaff, AZ.
(b) Box marks the far-east side of the BPLF where seismic data was collected.
(c) A snapshot of the field site. 145
Figure 46
(a) The figure represents the shot point locations as deployed on the ground. There are a total of nine shot points for the 2-D arrays. The 146

	yellow markers represent the shot point locations. (b) Schematic representation of various receiver arrays as deployed in the field. X-axis represents E-W traverse and Y-axis represents N-S traverse (i) Linear EW (ii) Linear NS (iii) Cross (iv) Random	147
Figure 47	Typical shot gathers for various array types as acquired from the BPLF field site. Data was collected for 1000 ms but only the first 500 ms data is shown here as surface waves are more prominent here.	148
Figure 48	Dispersion images obtained from shot gathers for various receiver arrays in Figure 8.3. The x-axis represents the frequency (Hz) and y-axis represents the phase velocity (m/s). The white dots on the dispersion image represent the fundamental mode picks for various receiver arrays.	151
Figure 49	The 1-D shear wave velocity profiles obtained from the dispersion curves extracted from the dispersion images in Figure 48. The x-axis represents the shear wave velocity (m/s) and the y-axis represents the depth (m).	152
Figure 50	A graph comparing dispersion curves for various receiver arrays. The X-axis represents frequency (Hz) and Y-axis represents phase velocity (m/s).	153
Figure 51	Velocity (m/s) versus depth (m) comparison for various receiver arrays. The X-axis represents shear wave velocity (m/s) and Y-axis represents depth (m).	154
Figure 52	Graphical representation of Vs profiles for all receiver array types shown together in a single graph.	157
Figure 53	Interpreted soil profile as estimated for the conventional linear array and newly developed random array for up to 20 m depth.	158

LIST OF TABLES

Table 1	Relationships among elastic constants (modified from Achenbacj, 1973)	12
Table 2	Literature review on applications of MASW technique	36
Table 3	Data acquisition parameters for active survey (modified from www.masw.com)	40
Table 4	Summary of data acquisition parameters	78
Table 5	Statistical parameters used in Kriging method.	84
Table 6	Parameters as used in the field for different receiver arrays	96
Table 7	Statistical analysis performed on dispersion and inversion data using SAS and SPSS programming with dependent variables (a) frequency; (b) phase velocity (c) Vs. Pattern represents the geophone arrangement and data represents the 3 replicas obtained for each set of arrangement	114
Table 8	Statistical analysis performed on the three replicas of both (a) dispersion and (b) inversion data using SAS and SPSS programming.	114
Table 9	Statistical analysis performed on each array type using SAS and SPSS programming for (a) dispersion data with phase velocity as dependent variable; (b) inversion data with Vs velocity as dependent variable	115
Table 10	A layered earth model parameters	123
Table 11	Longest wavelength (λmax) and corresponding approximate depth of investigation (Zmax) calculated for each type of configuration	132
Table 12	Summary of data acquisition parameters	149
Table 13	Dynamic properties of soil layers with depth at BPLF site measured using MASW method	156

CHAPTER-1

Introduction

1.1 MOTIVATION

There are many unanswered questions related to the properties of the moon, its internal structure and makeup. Although scientists have previously studied various layers of the moon, and many velocity models exists explaining the velocity variations in the mantle and core (explained in section 3.1.2), none have reported in detail any study regarding the engineering properties of the shallow lunar subsurface (e.g., upper 30 m). Understanding the behavior of soils to various types of loading conditions is a primary goal in geotechnical engineering. Engineering properties, like the shear modulus and Poisson's ratio, are critical parameters with respect to most civil engineering works as they characterize the mechanical behavior of geotechnical materials under various types of loading. Therefore, the *in situ* estimation of shear wave velocity of soils is critically important in terms of determining the shear modulus of soil, regolith, and rock. This study will be used to detail one possible method to answer this question and help scientists and engineers better understand the shallow subsurface properties of the moon.

1.2 RESEARCH OBJECTIVES

The main focus of research in this study is to improve and increase the usage of MASW method in determining regolith and rock properties by introducing a new type of receiver arrangement to extend its usage on other planetary bodies like the Moon, Mars, or other solid bodies in the solar system. Both field tests and numerical simulations are used to examine this issue. The successful application of the results obtained from this study will help not only the geotechnical community but also other scientific communities by obtaining more reliable determination of regolith properties and readily-deployable data techniques.

The first objective of this research is to investigate a new method suitable and applicable on the Moon, and thus on any planetary surface to estimate geotechnical properties. Geotechnical or engineering properties are those properties that effect construction and engineering. Engineering properties--like shear strength, shear modulus and Poisson's ratio--are key parameters for civil engineering works, as they characterize the mechanical behavior of geotechnical materials under various types of loading. The multi-channel seismic method has previously been demonstrated to greatly increase our ability to map shear-wave velocities and subsurface variations in physical properties. However, considering the logistical constraints involved in deploying linear or circular array robotically or by astronaut, a random array will be better suited for lunar exploration. Therefore, the first hypothesis of this research is that a random-array seismometer deployment scheme can be used to obtain reliable and high resolution dispersion images.

The second objective of this research is to acquire MASW data for various conventional geophone arrays—such as the linear, cross, circular and triangular—as well as a random deployment for direct comparison. The main hypothesis is that conventional and newly developed arrays will yield similar results, as demonstrated by a correlation between the dispersion curves and the accuracy of the shear-wave velocity profiles. As a follow on component of this objective, computer simulations are conducted to study various effects such as increasing grid size, increasing numbers of receiver, etc. Simulation models are generated for various possibilities of rock/regolith property variations under certain parameters like varying velocities, frequencies, and depth to the subsurface.

The third objective is a field-based approach used to apply the results from objectives one & two by determining engineering properties for the upper 30 m of a lunar analog site. Analog sites are places or spaces on earth that approximate, in some respect, the geological,

environmental and putative biological conditions or settings on a particular planetary body, either at the present day or sometime in the past. A previously-determined terrestrial analog site that is suitable as a lunar analogs was selected, and near-surface seismic data has been acquired using random arrangement of geophones. The hypothesis of this objective is that the random-array MASW technique can yield acceptable results on a lunar analog.

1.3 DISSERTATION OUTLINE

Following this introduction in Chapter 1, Chapter 2 is used to describe the history of seismic waves with detailed description of Rayleigh waves, relevant equations, and behavior of Rayleigh waves in homogeneous and heterogeneous media. This will lay the fundamental groundwork for subsequent chapters.

Chapter 3 is dedicated solely describing the traditional surface wave techniques such as spectral analysis of surface waves (SASW) and MASW methods. A detailed procedure for MASW is covered in this chapter including its origin, importance, types of MASW methods, advantages and disadvantages of each type, data acquisition, data processing, and inversion. A subsection is used to describe various kinds of traditional receiver arrays as well as the importance of random arrays that is essential in subsequent chapters.

Chapter 4 is used to cover the geologic history of the Moon, the lunar landscape, the lunar regolith, importance of lunar regolith, and physical properties of the moon studied with reference to geotechnical properties to date. This background chapter is useful for the subsequent lunar analogue discussion in Chapter 8.

Chapter 5 presents the newly-developed random receiver array technique, including the data acquisition and processing scheme. Preliminary results obtained from this technique are also presented. These results are briefly compared with conventional linear geophone array in order to show the correlation between them and set the stage for the next chapter.

Chapter 6 presents a detailed comparison study between the traditional geophone arrays like the linear, cross, & circular with that of the newly developed random-geometry geophone array. This is mainly used to examine and identify the effectiveness/advantages from the use of random geophone array with respect to data acquisition, dispersion imaging, azimuthal variations etc.

Chapter 7 presents results of a suite of numerical simulations that are performed to study the effect of various parameters pertaining to random array geometry such as clustering effects, skewness effects, and total number of seismometers used within the random geophone array. Comparison of field and modeled data results are presented.

Chapter 8 covers the applicability of random array MASW method to delineate geotechnical properties of subsurface in a field-based case study. The results obtained from the Black Point Lava Flow (BPLF) site-a lunar analog are presented, including elucidation of the significance of the chosen site as compared to other prominent lunar analogs.

Finally, Chapter 9 provides the summary and conclusions of this research and recommendations for future work.

1.4 SIGNIFICANCE OF THE STUDY

There are many unanswered questions related to the properties of the moon, its internal structure, and makeup. Although scientists have previously studied various layers of the moon, and many velocity models exists explaining the velocity variations in the mantle and core (*see* Section 3.1.2), no refereed literature exists reporting in detail the engineering properties of the shallow lunar subsurface (e.g., upper 30 m), either directly or using any near-surface geophysical techniques. Engineering properties, such as shear modulus and Poisson's ratio, are critical parameters with respect to most civil engineering works as they characterize the mechanical behavior of geotechnical materials under various types of loading. Therefore, the *in situ* estimation of shear wave velocity of rock and regolith is critically important in terms of determining the shear modulus. The ultimate outcome of this research is the presentation of a exploration-friendly method to answer this question and help scientists & engineers to better understand the surface properties of the Moon.

CHAPTER 2

Rayleigh Waves in Vertically Heterogeneous Media

2.1 INTRODUCTION

Surface waves were first introduced by Lord Rayleigh as the solution of the equation of waves propagating along the free surface of an elastic half-space in 1885 (Rayleigh, 1885). In geotechnical engineering, surface waves have been used to determine the dynamic properties of near-surface soil, regolith, and bedrock non-invasively for the past 50 years (e.g., Jones, 1958; Richard et al., 1970; Nazarian, 1984; Stokoe et al., 1994; Tokimatsu, 1995; Rix et al., 2001b; Okada, 2003). Surface wave methods are based on measured vertical particle motions of Rayleigh waves at various locations on the ground surface. The measured motions depend on the properties of the medium, the frequency of the waves, and the distance from a source location to the ground-motion detectors (seismometers or *geophones*).

In this chapter, the theoretical study of Rayleigh wave propagation in homogeneous and layered media is addressed. A layered medium consisting of a stack of homogeneous, isotropic, and elastic layers overlying a homogeneous half-space represents an appropriate model for vertically heterogeneous soil/regolith/rock profiles. The layered model is often used in inversion procedures of surface wave methods due to computational efficiency.

2.2 CHARACTERISTICS OF BODY AND SURFACE WAVES

Seismic waves propagating in a medium bounded above by a free surface can be categorized into two types: body waves and surface waves. Body waves propagate through the interior of the medium and along the free surface and are of two types: *P*- and *S*-waves. *P*-waves propagate with a compressive disturbance while *S*-waves induce a shearing deformation. The particle motion associated with *P*-waves is parallel to the direction of propagation, while the particle motion associated with *S*-waves is perpendicular to the direction of wave propagation as shown in **Figure**

1 (a) and (b), respectively. According to the plane of particle motion, *S*-waves can be subdivided into two types: vertically polarized shear (SV) and horizontally polarized shear (SH) waves.

Surface waves are produced by the interaction between *P*- and *S*-waves at the free surface. They travel along the surface of a medium with amplitude that exponentially decreases with depth. They can be divided into two types: Love waves and Rayleigh waves. Love waves are generated only when energy is trapped in a soft surface layer over a stiffer half-space resulting in multiple reflections. Since Love waves result from the interaction of *P*- and *SH*-waves, the particle motion has a horizontal component, as shown in **Figure 1 (c).** Rayleigh waves, which are generated by the interaction of *P*- and *SV*-waves, have both vertical and horizontal particle motion as shown in **Figure 1 (d).**

Most surface wave methods used in geotechnical engineering are based on the velocity and attenuation of Rayleigh waves. In the research described herein, "surface waves" will be used to mean Rayleigh waves, unless otherwise stated.

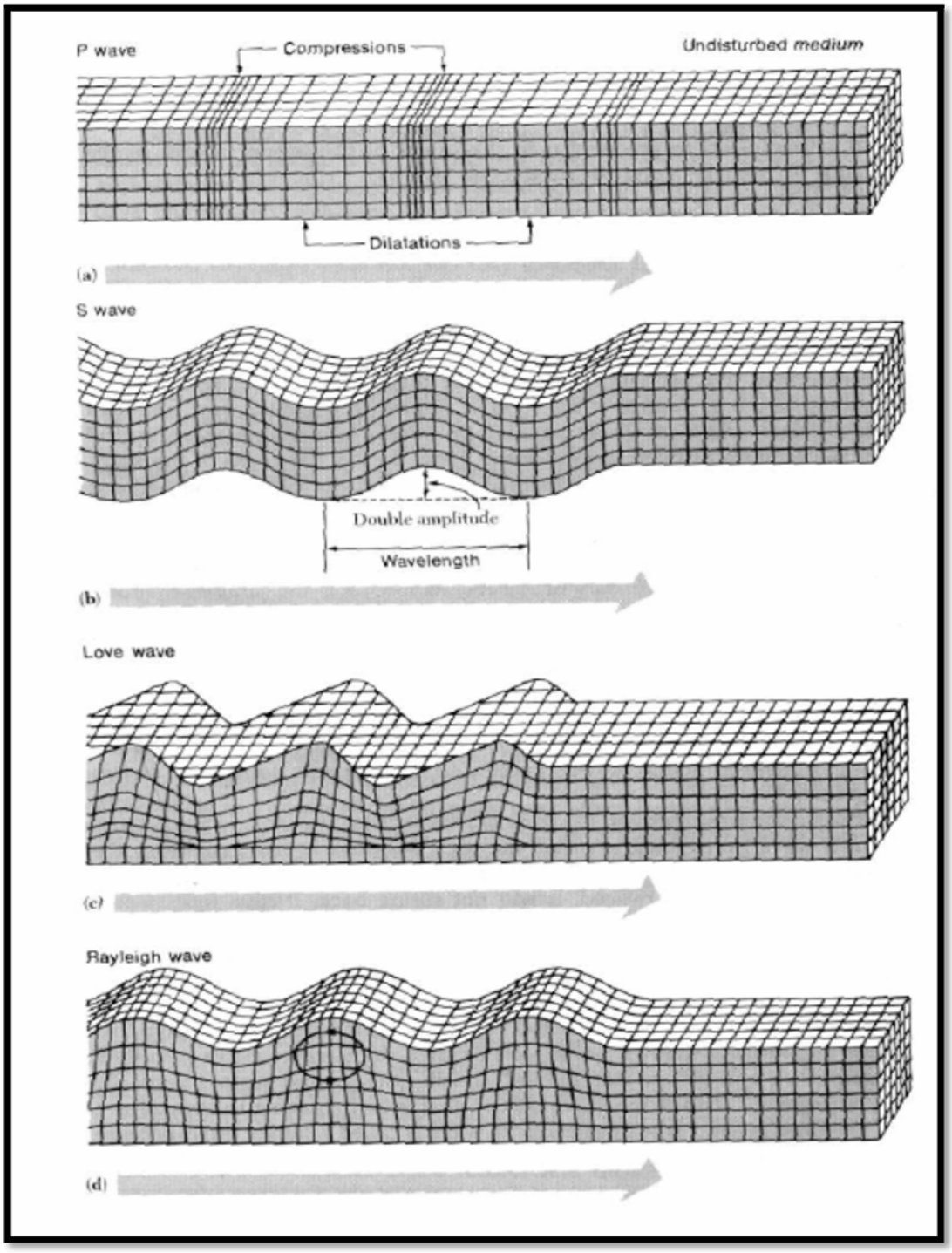


Figure 1. Body waves ((a) and (b)) and surface waves ((c) and (d)). The arrows indicate the direction of wave propagation. (Bolt, 1993)

2.3 RAYLEIGH WAVES IN A HOMOGENEOUS HALF-SPACE

2.3.1 Rayleigh wave equation

In 1885 Lord Rayleigh published a paper regarding waves propagating along the plane at the free-surface boundary above a homogeneous isotropic elastic half-space, and such waves are now called Rayleigh waves. Rayleigh waves propagating through a homogeneous half-space have been theoretically investigating by many researchers, for example, Rayleigh (1885), Viktorov (1967), Richart et al. (1970), Graff (1975), and Achenbach (1973). For the study of Rayleigh wave propagation in elastic media including a homogeneous half-space, a Cartesian coordinate system is defined as shown in **Figure 2**.

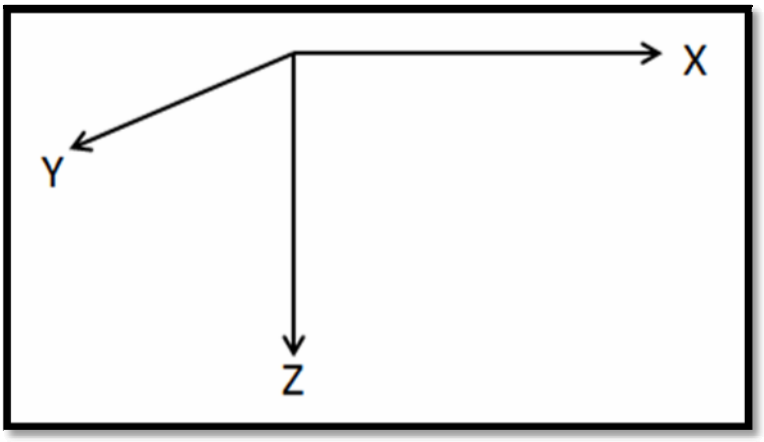


Figure 2. Cartesian coordinate system

A set of three basic equations for a homogeneous isotropic elastic medium is summarized using the Cartesian tensor notation as:

$$\sigma_{ij,j} + \rho b_i = \rho \ddot{u}_i \qquad \text{(Equations of Motion)} \tag{2.1}$$

$$\varepsilon_{ij} = \frac{1}{2} \cdot (u_{i,j} + u_{j,i}) \qquad \text{(Kinematical Equations)} \tag{2.2}$$

$$\sigma_{ij} = \lambda \varepsilon_{kk} \delta_{ij} + 2\mu \varepsilon_{ij} \qquad \text{(Constitutive Equations)} \tag{2.3}$$

where i,j = x,y,z directions, σ_{ij} is the stress tensor at a point, u_i is the displacement vector for the i direction ρ is the mass density, b_i is the body force per unit mass of material, and is a strain tensor. The terms μ and λ are the Lame parameters, which are elastic constants for the medium. Each constant can be expressed in terms of the other elastic constants such as Young's modulus (E), Poisson's ratio (v), and the bulk modulus (B) as summarized in **Table 1**.

Table 1. Relationships among elastic constants (modified from Achenbacj, 1973)

	$E,\ \nu$	$E,\ G$	$\lambda,\ G$
λ	$\frac{E\nu}{(1+\nu)(1-2\nu)}$	$\frac{\mu(E-2G)}{3G-E}$	λ
μ	$\frac{E}{2(1+\nu)}$	G	G
E	E	E	$\frac{G(3\lambda+2G)}{\lambda+G}$
B	$\frac{E}{3(1-2\nu)}$	$\frac{GE}{3(3G-E)}$	$\lambda+\frac{2}{3}G$
ν	ν	$\frac{E-2G}{2G}$	$\frac{\lambda}{2(\lambda+G)}$

Another expression of Equation 2.1 in terms of displacements is obtained by substituting Equations 2.2 into Equation 2.3 and then substituting the resulting equation into Equation 2.1, yieliding Navier's equation. In the absence of body waves, Navier's equation is given by:

$$\mu u_{i,jj} + (\lambda + \mu) u_{j,ji} = \rho \ddot{u}_i \quad \text{(2.4)}$$

In vector form, it can be expressed by:

$$\mu \nabla^2 \mathbf{u} + (\lambda + \mu) \nabla \nabla \cdot \mathbf{u} = \rho \ddot{\mathbf{u}} \quad \text{(2.5a)}$$

Where ∇ represents the gradient vector operator, which is expressed by:

$$\nabla = \frac{\partial}{\partial x} i_x + \frac{\partial}{\partial y} i_y + \frac{\partial}{\partial z} i_z \quad \text{(2.5b)}$$

and ∇^2 represents the Laplacian operator given by:

$$\nabla^2 = \frac{\partial^2}{\partial x^2} + \frac{\partial^2}{\partial y^2} + \frac{\partial^2}{\partial z^2} \quad \text{(2.5c)}$$

Solutions of Navier's equation can be obtained by a method known as Helmholtz's decomposition. It is assumed that the particle displacement vectors in the equation can be written by:

$$\mathbf{u} = \nabla \phi + \nabla \times \boldsymbol{\psi} \quad \text{(2.6)}$$

where Φ and Ψ are scalar and vector potentials, respectively.

By substituting Equation 2.6 into Navier's equation, we obtain:

$$\nabla^2\phi = \frac{1}{V_P{}^2}\frac{\partial^2\phi}{\partial t^2} \qquad (2.7)$$

$$\nabla^2\psi = \frac{1}{V_S{}^2}\frac{\partial^2\psi}{\partial t^2} \qquad (2.8)$$

Where,

$$V_S = \sqrt{\frac{\mu}{\rho}} = \sqrt{\frac{G}{\rho}},\ V_P = \sqrt{\frac{\lambda + 2\mu}{\rho}} = \sqrt{\frac{\lambda + 2G}{\rho}}$$

And Vp and Vs are *P*-wave and *S*-wave propagation velocities, respectively.

Considering waves propagating only in the x-z directions as shown in **Figure 3**, Equations 2.7 and 2.8 can be rewritten as:

$$\left(\frac{\partial^2\phi}{\partial x^2} + \frac{\partial^2\phi}{\partial z^2}\right) = \frac{1}{V_P{}^2}\frac{\partial^2\phi}{\partial t^2} \qquad (2.9)$$

$$\left(\frac{\partial^2\psi}{\partial x^2} + \frac{\partial^2\psi}{\partial z^2}\right) = \frac{1}{V_S{}^2}\frac{\partial^2\psi}{\partial t^2} \qquad (2.10)$$

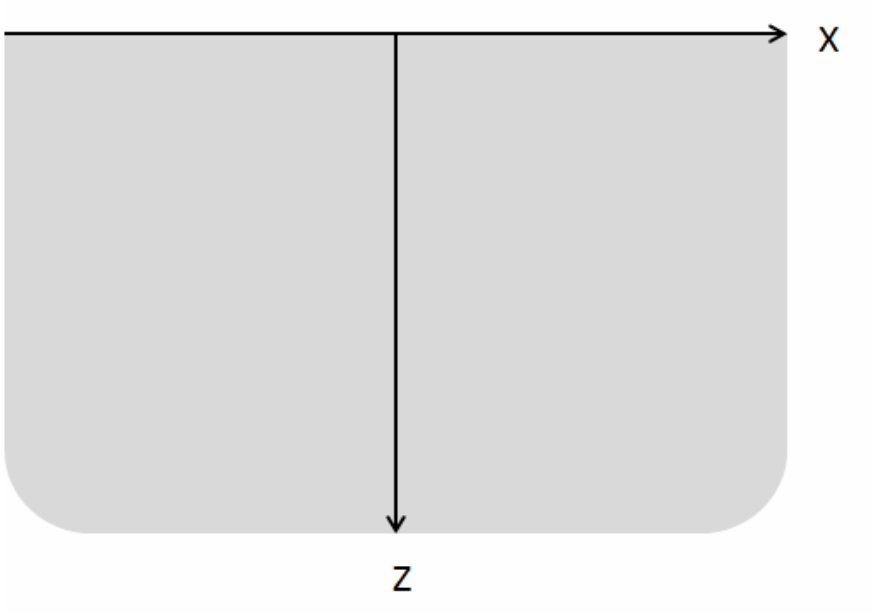


Figure 3. Coordinate system in a homogeneous half-space

Assuming time-harmonic, plane waves traveling along the x-direction, the displacement potentials are expressed by:

$$\phi(x,z) = F(z) \cdot e^{i(\omega t - kx)} \quad (2.11)$$

$$\psi(x,z) = G(z) \cdot e^{i(\omega t - kx)} \quad (2.12)$$

where F(z) and G(z) are amplitudes that are functions of depth, ω is the angular frequency, and k is the wavenumber. Substituting Φ (x,z) and Ψ (x,z) from Equations 2.11 and 2.12 into Equations 2.9 and 2.10, two ordinary differential equations are obtained:

$$\frac{d^2F(z)}{dz^2} + \left(\frac{\omega^2}{V_P^{\,2}} - k^2\right) \cdot F(z) = 0 \qquad (2.13)$$

$$\frac{d^2G(z)}{dz^2} + \left(\frac{\omega^2}{V_S^{\,2}} - k^2\right) \cdot G(z) = 0 \qquad (2.14)$$

Solving Equations 2.13 and 2.14 gives:

$$F(z) = A_1 \cdot e^{-pz} + A_2 \cdot e^{pz} \qquad (2.15)$$

$$G(z) = B_1 \cdot e^{-qz} + B_2 \cdot e^{qz} \qquad (2.16)$$

where

$$p = \sqrt{k^2 - \frac{\omega^2}{V_P^{\,2}}} \text{ and } q = \sqrt{k^2 - \frac{\omega^2}{V_S^{\,2}}}\,.$$

Equations 2.11 and 2.12 can be written as:

$$\phi(x,z) = \left(A_1 e^{-pz} + A_2 e^{pz}\right) \cdot e^{i(\omega t - kx)} \qquad (2.17)$$

$$\psi(x,z) = \left(B_1 e^{-qz} + B_2 e^{qz}\right) \cdot e^{i(\omega t - kx)} \qquad (2.18)$$

The constants A1, A2, B1, and B2 are real-valued constants that are determined from the boundary condition for Rayleigh waves, which are zero stresses at free surface and no displacement at infinite depth:

$$\tau_{zx}(x,0) = \tau_{zz}(x,0) = 0 \qquad (2.19)$$

$$\mathbf{u}(x,z) = 0 \quad \text{as} \quad z \to \infty \qquad (2.20)$$

The constants A2 and B2 are, therefore, equal to zero from Equation 2.20. Substituting Equations 2.17 and 2.18 into Equation 2.6, the displacement field u(x,z) can be obtained. Using the computed displacements and equations 2.2 and 2.3, the stress field can also be computed. Applying all the boundary conditions, the final result can be obtained in matrix form.

$$\begin{bmatrix} 2p & \frac{k^2}{q}\cdot\left(2-\frac{V_R^{\,2}}{V_S^{\,2}}\right) \\ \left(2-\frac{V_R^{\,2}}{V_S^{\,2}}\right) & 2 \end{bmatrix} \cdot \begin{bmatrix} A_1 \\ B_1 \end{bmatrix} = \begin{bmatrix} 0 \\ 0 \end{bmatrix} \qquad (2.21)$$

where V_R is the Rayleigh wave phase velocity.

A non-trivial solution of Equation 2.21 can be computed by:

$$\det\begin{bmatrix} 2p & \frac{k^2}{q}\cdot\left(2-\frac{V_R^{\,2}}{V_S^{\,2}}\right) \\ \left(2-\frac{V_R^{\,2}}{V_S^{\,2}}\right) & 2 \end{bmatrix} = 0 \qquad (2.22)$$

from which final equation can be derived as follows:

$$\left(2-\frac{V_R^{\,2}}{V_S^{\,2}}\right)^2-4\left(1-\frac{V_R^{\,2}}{V_P^{\,2}}\right)^{0.5}\cdot\left(1-\frac{V_R^{\,2}}{V_S^{\,2}}\right)^{0.5}=0 \qquad (2.23)$$

Equation 2.23 is called the *characteristic equation of Rayleigh waves* or just *Rayleigh wave equation*. It is important to note from this equation that the Rayleigh wave velocity (V_R) is a function of both *P*-wave and *S*-wave velocities and is independent of frequency, which means that Rayleigh waves are non-dispersive in homogeneous half-space.

The value for V_R can also be estimated as a function of the shear-wave velocity (V_S) and Poisson's ratio (*see* Stokoe and Santamarina, 2000; modified by Achenbach, 1973):

$$V_R=\frac{0.874+1.117\nu}{1+\nu}V_S \qquad (2.24)$$

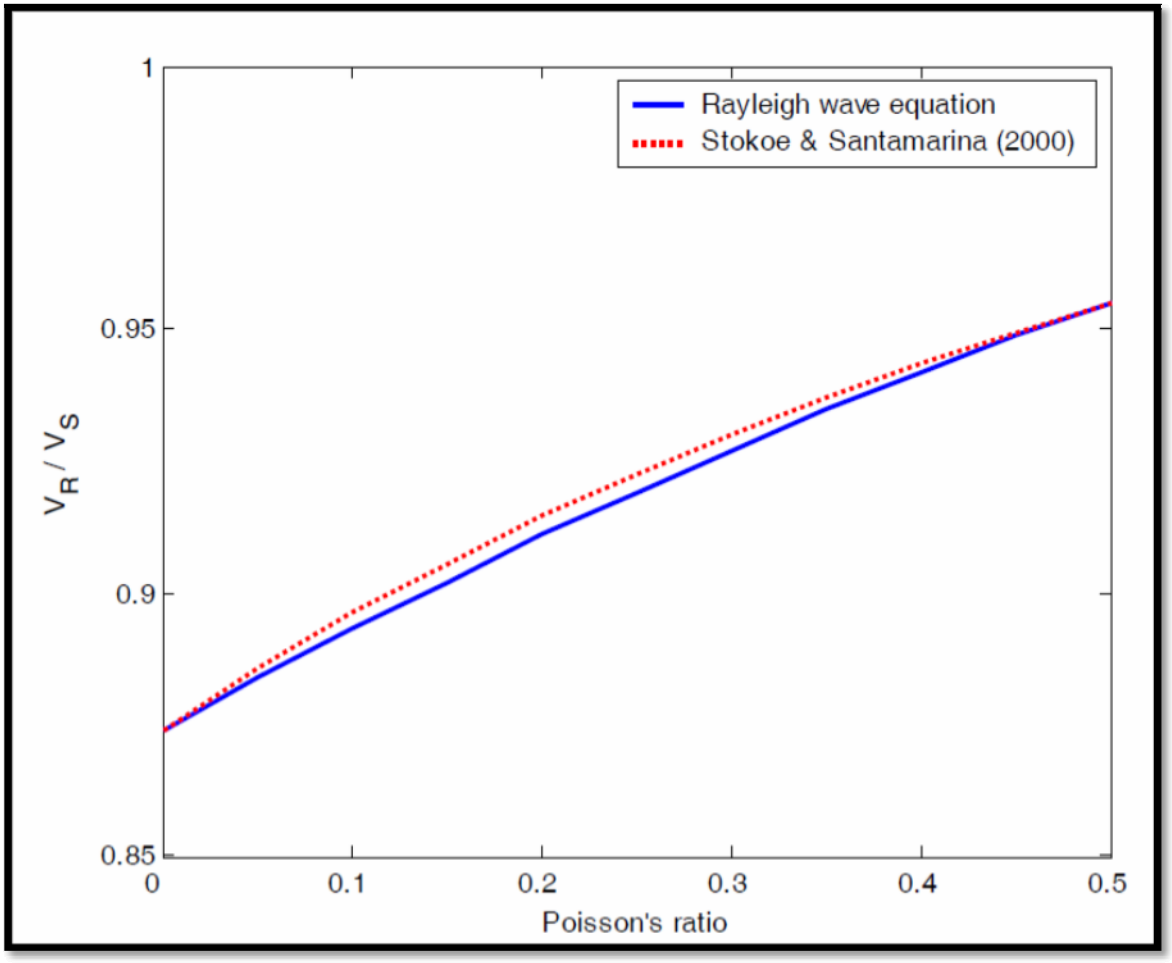


Figure 4. Ratio of V_R to V_S with Poisson's ratio. It compares the estimated values of V_R to the values from the Rayleigh wave equation. (Modified from Sungsoon, 2005)

2.3.2 Displacements due to Rayleigh waves

Along with the Rayleigh wave velocities it is also of importance to understand the displacement of Rayleigh waves in a homogenous half space. As the equation is derived from the Helmholtz's decomposition, Rayleigh waves are composed of the superposition of longitudinal and transverse components. Therefore it is possible to derive the vertical and horizontal

components of displacements associated with Rayleigh waves that are propagating through a homogenous half-space medium. Equation 2.6 can therefore be written as:

$$u_x = \frac{\partial \phi}{\partial x} + \frac{\partial \psi}{\partial z} \quad \text{(2.25)}$$

$$u_z = \frac{\partial \phi}{\partial z} - \frac{\partial \psi}{\partial x} \quad \text{(2.26)}$$

The horizontal and vertical displacements of Rayleigh waves in a homogenous medium can be obtained from the above equations by substituting the solutions for the two potential functions, Φ and Ψ.

$$u_x(x,z) = ikA_1\left(-e^{-pz} + \frac{2pq}{q^2+k^2}e^{-qz}\right)e^{i(\omega t - kx)} \quad \text{(2.27)}$$

$$u_z(x,z) = kA_1\left(-\frac{p}{k}e^{-pz} + \frac{2pk}{q^2+k^2}e^{-qz}\right)e^{i(\omega t - kx)} \quad \text{(2.28)}$$

At t=0 and x=0, the vertical and horizontal displacements can be plotted as a function of depth as shown in **Figure 5**.

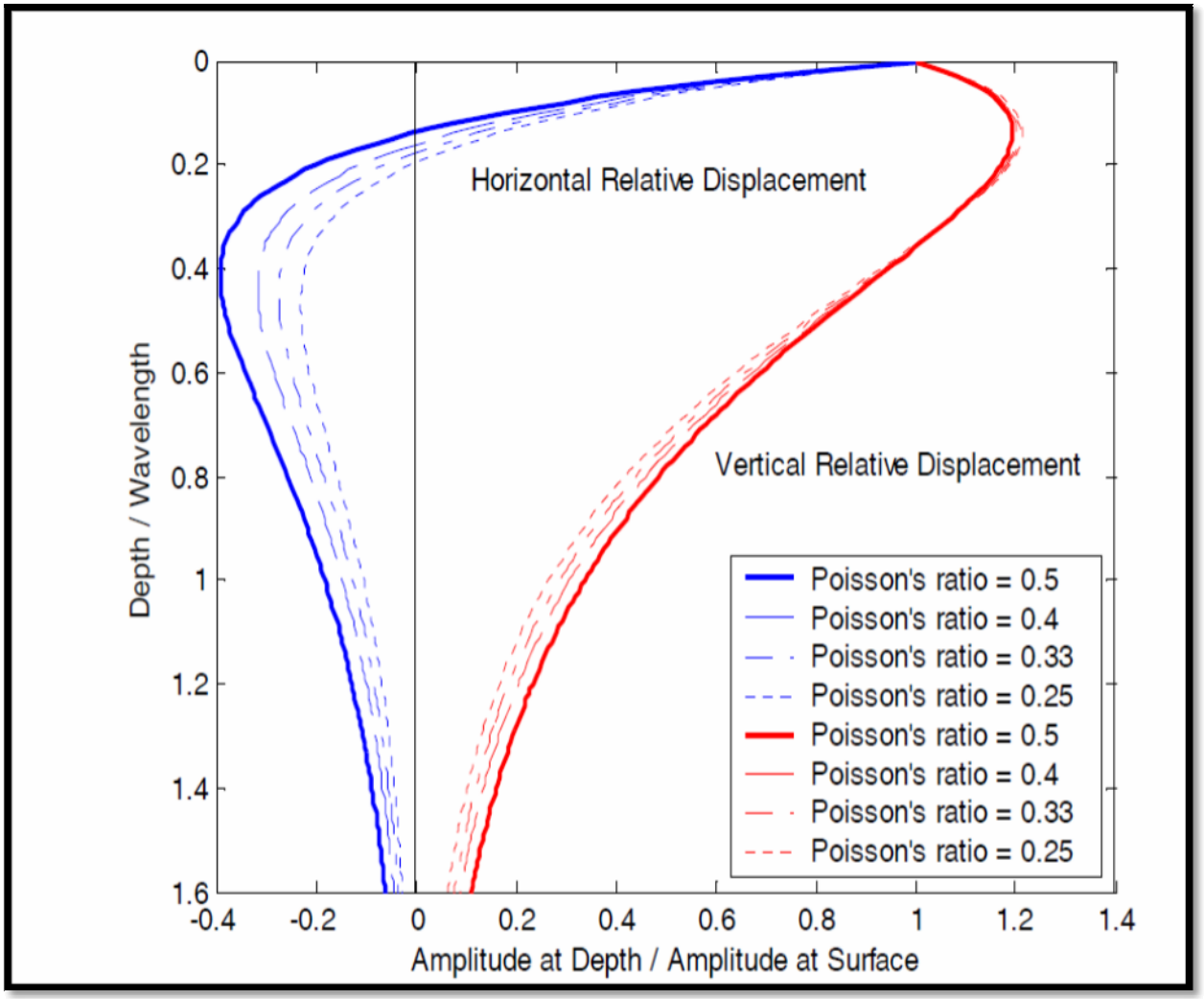


Figure 5. Vertical and horizontal displacements of Rayleigh waves in homogeneous half-space media (after Richart et al., 1970)

2.4 RAYLEIGH WAVES IN LAYERED MEDIA

2.4.1 Dispersion equation

In the real world, assuming a homogenous half space for modeling subsurface properties is a bit too simple and unrealistic. Instead, subsurface properties that vary with depth may be idealized using a simplified layered model as shown in **Figure 6**. This simplification consists of N number of homogenous, isotropic, elastic layers characterized with properties like shear wave

velocity (Vs), density (ρ), Poisson's ratio (Φ) and thickness (h)**.** These types of layered media are modeled frequently in most geotechnical cases due to computational efficiency, and yield robust approximations.

The boundary conditions that are applied for a homogenous half space are (i) no stress at the surface and (ii) zero amplitude at infinite depth. These conditions are also typically valid for the layered media with extra boundary conditions applied to the continuity in stress and displacements at the interface between each layer, and these additional boundary conditions are expressed as:

$$\tau_{zx}(x, z_n) = \tau_{zx}(x, z_{n+1}) \quad (2.29)$$

$$\tau_{zz}(x, z_n) = \tau_{zx}(x, z_{n+1}) \quad (2.30)$$

$$\mathbf{u}(x, z_n) = \mathbf{u}(x, z_{n+1}) \quad (2.31)$$

where n=1,……,N

Displacements $u_n(x, z)$ in each layer are obtained by:

$$\mathbf{u}_n(x, z) = \nabla\phi_n + \nabla \times \psi_n \quad (2.32)$$

Application of the boundary conditions in equations 2.31 and 2.32 will yield a homogeneous system of 4N-2 linear equations, denoted by *S*. Non-trivial solutions can be obtained by setting det[S]=0, and this leads to the final product that is called the *Rayleigh dispersion equation* for a

layered half-space. The equation provides an implicit relationship between the phase velocity of Rayleigh waves, frequency, and the properties of the layers, and can be written (Lai, 1998):

$$f_R(V_{S,n}, \nu_n, \rho_n, h_n, k_j, \omega) = 0 \quad \text{(2.33)}$$

It is evident from equation 2.33 that the phase velocity of Rayleigh waves in a vertically heterogeneous medium is dependent on frequency. This phenomenon is known as geometric dispersion, since it is related to the geometrical variations of properties with depth. **Figure 6** illustrates how geometric dispersion is caused, where a Rayleigh wave with shorter wavelength is confined within only the upper layer, while a longer wavelength Rayleigh wave has particle motion in all three layers. Therefore, it is the key element in surface wave methods that Rayleigh waves with different wavelengths (frequencies) sample different parts of layered medium (*see* Stokoe et al., 1994) allowing them to be used to determine variations in material properties with depth. However, for a given frequency, there exist multiple solutions for the Rayleigh dispersion equation. This means that for a given frequency, multiple modes for a given frequency traveling at different phase velocities exist. The concept of multiple modes can be explained physically by the constructive interference occurring among waves undergoing multiple reflections at the layer interfaces (*see* Lai, 1998).

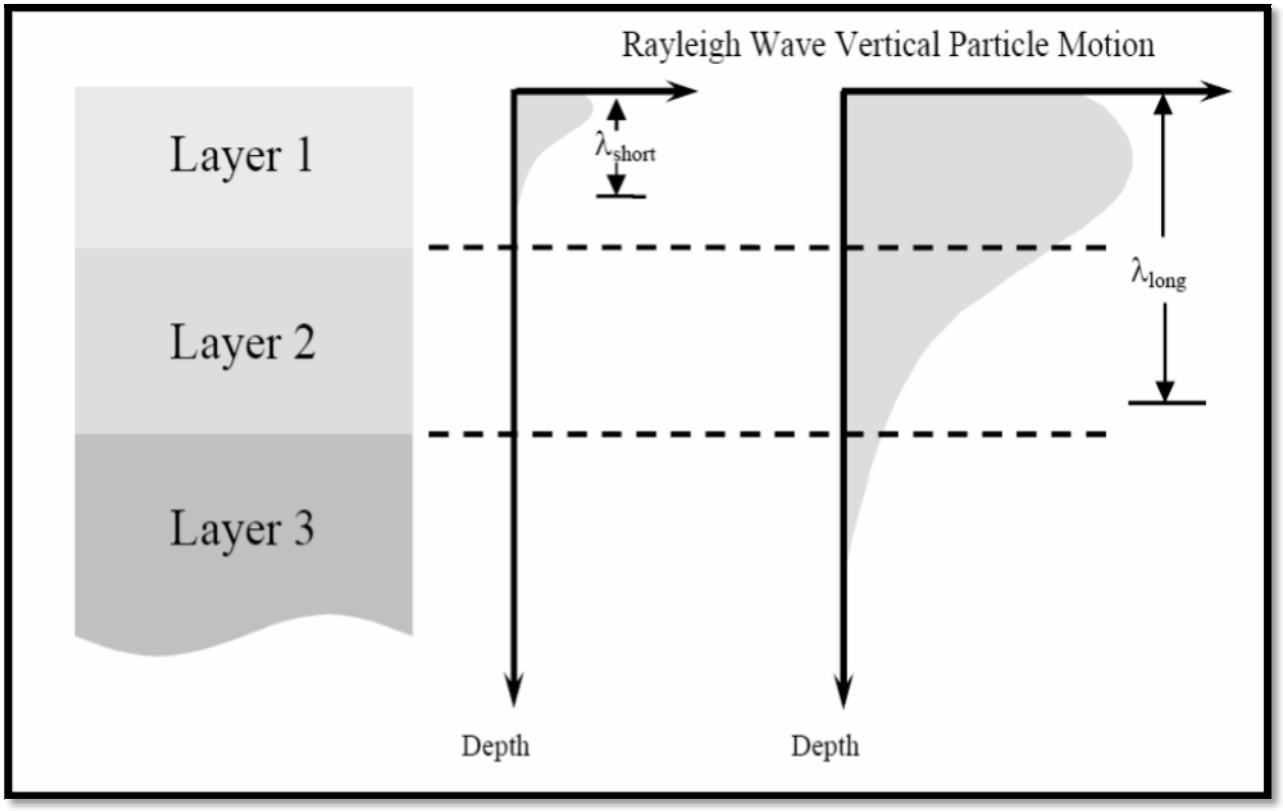


Figure 6. Vertical particle motions of two Rayleigh waves with different wavelengths (modified from Rix, 2000)

2.4.2 Phase velocities of Rayleigh waves

In most cases, differential eigenvalue problem (e.g., Aki and Richards, 1980) is used as an alternative formulation of the Rayleigh wave dispersion equation. A linear differential eigenvalue problem with displacement eigenfunctions $r_1(z,k,\omega)$ and $r_2(z,k,\omega)$ and stress eigenfunctions $r_3(z,k,\omega)$ and $r_4(z,k,\omega)$ in a layered medium is defined by:

$$\frac{df(z)}{dz} = A(z) \cdot f(z) \qquad (2.34)$$

Where $f(z) = [r_1\ r_2\ r_3\ r_4]^T$ and a 4-by-4 matrix A(z) are composed of elements which are functions of λ(z), G(z), ρ(z), k, and ω. The eigenfunctions r_1 and r_4 are defined by:

$$u_x = r_1(z,k,\omega)\cdot e^{i(\omega t - kx)} \qquad (2.35a)$$

$$u_z = i\cdot r_2(z,k,\omega)\cdot e^{i(\omega t - kx)} \qquad (2.35b)$$

$$\tau_{zx} = \mu\left(\frac{dr_1}{dz} - kr_2\right)\cdot e^{i(\omega t - kx)} = r_3(z,k,\omega)\cdot e^{i(\omega t - kx)} \qquad (2.36a)$$

$$\tau_{zz} = i\left[(\lambda + 2\mu)\frac{dr_2}{dz} + k\lambda r_1\right]\cdot e^{i(\omega t - kx)} = ir_4(z,k,\omega)\cdot e^{i(\omega t - kx)} \qquad (2.36b)$$

The boundary conditions described in Equations 2.19 and 2.20 can be written in terms of the displacement and stress eigenfunctions:

$$r_3(z,k,\omega) = r_4(z,k,\omega) = 0 \qquad \text{at} \qquad z = 0 \qquad (2.37)$$

$$r_1(z,k,\omega) = r_2(z,k,\omega) = 0 \qquad \text{as} \qquad z \to \infty \qquad (2.38)$$

Non-trivial solutions of Equation 2.34 for a given frequency exist only for special values of the wavenumber $k_j(\omega)$, (j=1,…..,M) where M is the total number of modes at a certain frequency ω by applying boundary conditions in Equations 2.37 and 2.38 (Lai, 1998). The values of k_j and the corresponding solutions $r_i(z,k_j,\omega)$, (i=1,….,4) are the eigenvalues and the eigenfunctions of the eigenvalue problem described in Equation 2.34, respectively (Lai, 1998).

The values of k_j for Rayleigh waves in the layered medium can be obtained by solving the Rayleigh dispersion equation in Equation 2.33 using solution techniques like transfer matrix method (Thomson 1950; Haskell 1953; Schwab and Knopoff, 1970; Abo-Zena, 1979), stiffness matrix method (Kausel and Roesset, 1981), and reflection and transmission coefficients method (Kennett, 1974; Kennett and Kerry, 1979; Luco and Aspel, 1983; Hisada, 1994; Hisada, 1995). Once the roots of the Rayleigh dispersion equation, i.e., the values of k_j, are obtained using one of the above solution methods, the eigenfunctions $r_i(z,k_j,\omega)$ satisfying Equation 2.34 can be easily calculated. Each pair of $r_i(z,k_j,\omega)$ and k_j defines a specific mode of Rayleigh wave propagation. On the other hand, in a medium consisting of a finite number of homogeneous layers overlying a homogeneous half-space, the total number of modes of Rayleigh wave propagation is always finite (Ewing et al., 1957).

CHAPTER-3

Multi-Channel Analysis of Surface Waves (MASW)

3.1 INTRODUCTION

As described in Chapter 2, there are two types of surface waves: Rayleigh and Love waves (Dobrin and Savit, 1988). Both represent the plane-wave solutions to the coupled elastic wave equation (*see* Haskell, 1953):

$$\partial^2\phi/\partial t^2 = V_p^2\,\nabla^2\phi \quad \text{and} \quad \partial^2\Psi/\partial t^2 = V_s^2\,\nabla^2\Psi \ldots\ldots (3.1)$$

In most of near-surface active-source seismic surveys when a compressional source is used, more than two-thirds of total seismic energy generated is imparted into Rayleigh waves (Richart et al., 1970), which is the principal component of surface waves generated most effectively in all kinds of surface seismic surveys. As previously described, surface waves obey the property of dispersion i.e. for a vertical velocity variation, each frequency component of a surface wave has a different propagation velocity (also called *phase velocity*), that in turn results in a different wavelength for each frequency of the propagated wave. Therefore, due to its dispersive property, ground roll can be utilized to infer near-surface elastic properties (Nazarian et al., 1983; Stokoe et al., 1994; Park et al., 1998a).

Constructing shear-wave velocity profiles through the analysis of plane-wave fundamental mode Rayeligh waves is one of the most common ways to use the dispersive properties of surface waves (Bullen, 1963). The phase velocities for different wavelengths can be found from the solutions to the wave equation (as described in Chapter 2) by treating the near surface materials as layered earth medium (Haskell, 1953). Therefore, by analyzing the dispersion feature of ground roll represented in recorded seismic data, the near-surface *S*-wave velocity (Vs) profiles can be constructed and the corresponding shear moduli (μ) are calculated from the relation between the two parameters.

$$V_s = (\mu/\rho)^{1/2} \ldots\ldots (3.2)$$

where ρ represents the density of material (assumed as constant since it varies little with depth (as compared to the scale of variations in bulk and shear modulus).

3.2 HISTORICAL CONTEXT OF THE SURFACE-WAVE METHOD

Early pioneering work in surface waves goes back to 1950s when the steady state method was first used by Van der Pol (1951) and Jones (1955) **(Figure 7)**. Most commonly known as the Continuous Surface Wave method (Mathew et al., 1996**; Figure 8)**, it is based on the fundamental-mode (M0) only, and at the time other Rayleigh wave assumptions and all other types of waves-higher modes, body waves, etc. were all ignored. While this method was gaining popularity amongst the geotechnical community, Tokimatsu et al. (Year) redefined the soil site inversion theory. Since the very early stage of the surface wave application, pavement was found to be more complex than soil (Sezawa, 1938; Press and Dobrin, 1956), with a special type of guided wave called the "leaky wave" that required a complex-domain approach in solving wave equations (Jones, 1962; Vidale, 1964). Martincek (1994) introduced a modern computer approach, but it still produced limited results.

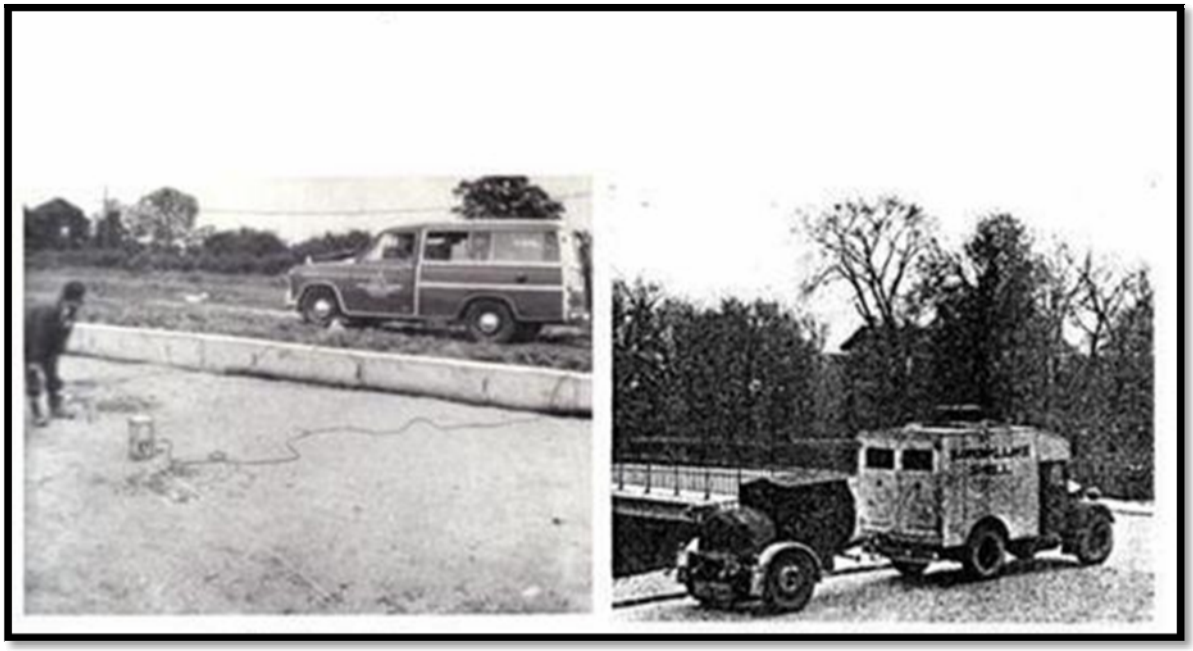


Figure 7. Steady state methods from 1950's. UK 1950s (left) and Van der Pool (1951) (right)

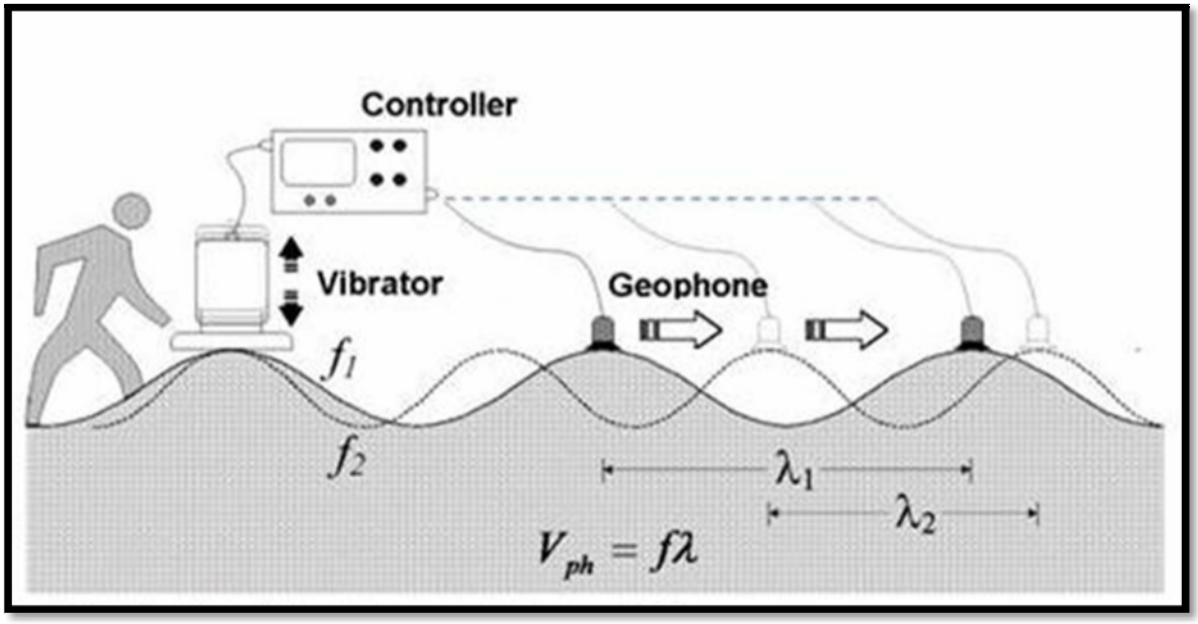


Figure 8. The Continuous Surface Wave method (from Mathew et.al., 1996)

3.2.1 Two-Receiver Approach (The SASW Method)

The Spectral Analysis of Surface Waves (SASW) method (Heisey et al., 1982) was introduced by scientists at University of Texas-Austin in the early 1980's. This method is based on the Fast Fourier Transform (FFT) analysis of phase spectra of surface waves generated by using an impulsive source like the sledge hammer (**Figure 9**). It was then that this method became widely used among geotechnical engineers and researchers. During the initial stage, again only the fundamental-mode (M0) Rayleigh wave assumption was used, but simultaneous multi-frequency generation from the impact seismic source and then by FFT during the subsequent data processing stage greatly improved overall efficiency of the method in comparison to conventional methods such as the continuous surface wave (CSW) method. Significant research on this method has since been conducted at UT-Austin (Nazarian et al., 1983; Rix et al., 1991; Al-Hunaidi, 1992; Gucunski and Woods, 1992; Aouad, 1993; Stokoe et al., 1994; Fonquinos, 1995; Ganji et al., 1998). More detailed information on this method and more detailed and complete list of publications on SASW up to early 1990's can be found in "Annotated bibliography on SASW" by Hiltunen and Gucunski (1994).

During the early stage of use, the SASW method was focused only on ways to enhance accuracy of the fundamental-mode (M0) Rayleigh-wave dispersion curve through field procedure and data processing efforts. But soon it was recognized that there might be a possibility of the curve "being more than M0" and therefore the concept of Higher Modes (HM's) were introduced in the studies (Roesset et al., 1990; Rix et al., 1991; Tokimatsu et al., 1992; Stokoe et al., 1994). It was then that the concept of "apparent (or effective)" dispersion curve (Gucunski amd Woods, 1992; Williams and Gucunski; 1995) was introduced that accounts for other multiple-mode possibilities (**Figure 10**). The following three main points categorizes

the difficulties with the SASW method and which led to the concept of multi-channel analysis of surface wave (MASW) method:

i. Higher modes (HM's) inclusion was underestimated
ii. Inclusion of other types of waves (body, reflected and scattered surface waves, etc.) was also underestimated or not considered at all (Sheu et al., 1988; Hiltunen and Woods, 1990; Foti, 2000).
iii. Data processing, for example, phase unwrapping (Al-Hunaidi, 1992) during the phase-spectrum analysis to construct a dispersion curve was also not accounted for.

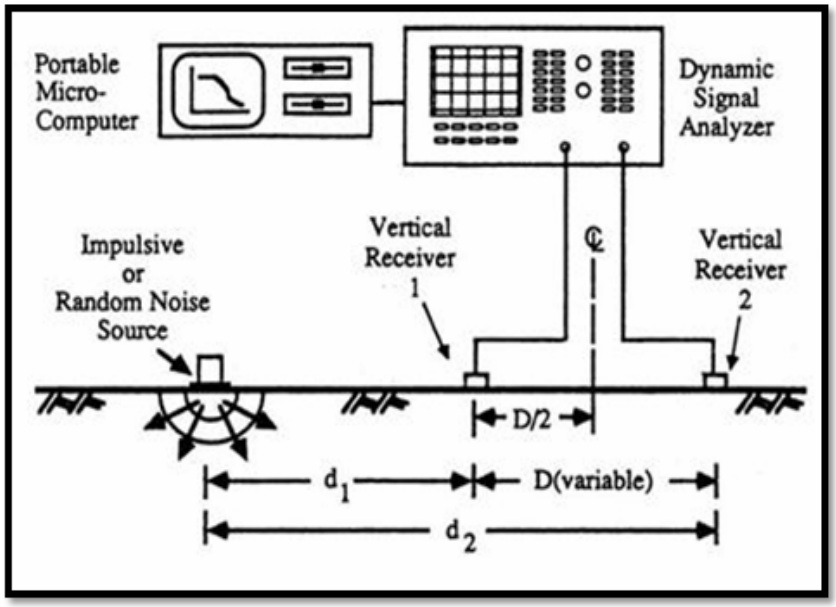


Figure 9. Schematic representing overall SASW field procedure (modified from Rix et.al., 1991)

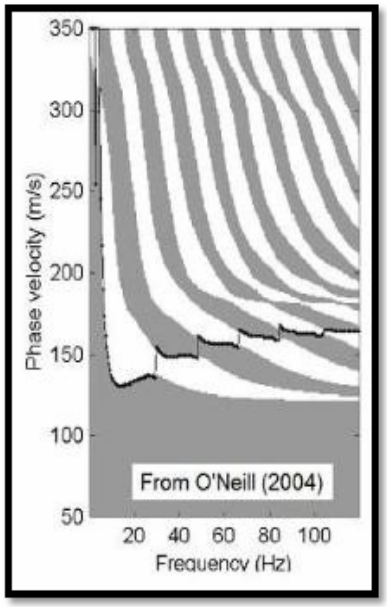


Figure 10. The apparent dispersion concept in SASW method (modified from O'Neill 2004)

3.2.2 The Multi-channel Approach (MASW)

The multi-channel analysis of surface waves method (MASW), first introduced into geotechnical and geophysical community in early 2000s (Park et al., 1999), is a seismic method which generates a shear wave velocity profile (i.e., Vs versus depth) by analyzing Rayleigh-type surface waves on a multi-channel (multiple geophones) record. The project actually started in mid-90s at the Kansas Geological Survey (KGS) by geophysicists who had been utilizing seismic reflection method to image earth's interior for depths up to several kilometers. At that time, surface waves were considered as a significant source of noise that were to be attenuated (**Figure 11**). But later this surface wave method, also called as the high-resolution reflection method, was used to image very shallow depths of engineering interest (e.g., 100 m or less; Baker, 1999). Keeping in mind the drawbacks in the SASW method, which clearly reached its limitation to handle complexities, the MASW method was mainly utilized for the purpose of geotechnical engineering projects. It is a seismic exploration method evaluating ground stiffness in 1-D, 2-D and 3-D formats for various types of geotechnical engineering projects. Since first introduction in the late 1990's, MASW has been utilized by numerous practitioners and researched by many investigators worldwide. Based on the theory that the number of geophones used can directly impact the resolving power of the method, researchers utilized diverse techniques already available after a long history of seismic data analysis (Telford et al., 1976; Robinson and Treitel, 1980; Yilmaz, 1987), and also developed new strategies in field and data processing to detail surface wave propagation properties and characterized key issues to bring out a routinely-useable seismic method.

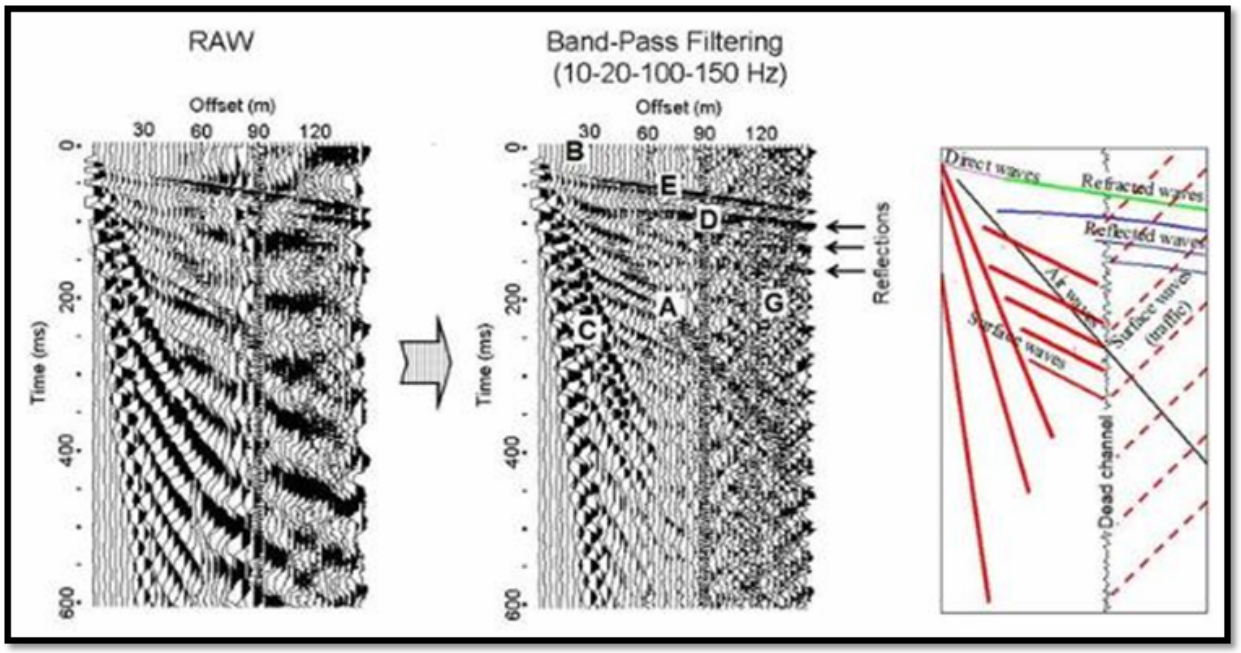


Figure 11. A field record showing reflections signals hidden by strong surface waves in raw data are seen after filtering (modified from www.masw.com/History-MASW.html).

Investigators in Netherlands first documented the MASW method in early 80s. They used a 24-channel acquisition system to deduce shear-wave velocity structure of tidal flats by analyzing recorded surface waves (Gabriels et al., 1987) (**Figure 12**). Later, Park and others (1999) used uncorrelated Vibroseis data to study the effectiveness of the multichannel approach, and detailed advantages with multichannel acquisition and processing concepts that suit geotechnical engineering applications. A table describing a few of many applications of the MASW technique is shown in **Table 2**.

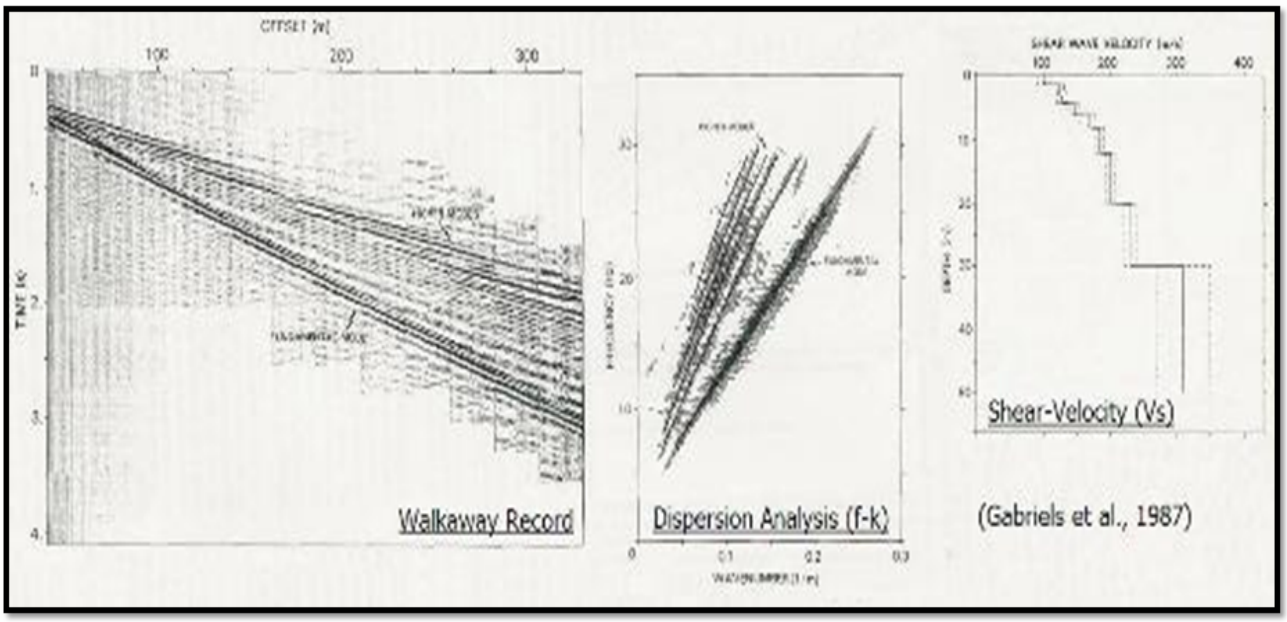


Figure 12. Summary of work performed by Gabriels et al., (1987) (modified from www.masw.com/History-MASW.html)

3.3 ADVANTAGES OF MASW

Directly measuring shear-wave velocities from a shear-wave survey is difficult in terms of maintaining favorable signal-to-noise ratio (S/N) during both data acquisition and data processing. But MASW method provides fairly favorable and competent results: the data acquisition is more tolerant in terms of selecting the parameters than any other near-surface seismic methods and also provides high S/N due to the fact that seismic surface waves are the strongest seismic waves generated that can travel longer distance than body waves without suffering from significant noise contamination. Because of high S/N, the MASW method yields reliable pattern recognition on a seismic record. i.e. it can be used to extract signal in midst of noise of many natural or cultural activities and also to other types of inherent seismic waves generated simultaneously.

Table 2. Literature review on applications of MASW technique

Author	Year	Title
Park, C.B., and Miller R.D	2004	MASW to map shear-wave velocity of soil
Penumadu,D., and Park C.B	2005	MASW method for geotechnical site characterization
Park, C.B., and Miller, R.D	2003	MASW for shear wave velocity evaluation of soil before and after deep dynamic compaction operations
Miller, R.D., Xia, J., Park, C.B., and Ivanov,J	1999	Multichannel analysis of surface waves to map bedrock
Xia,J., Miller, R.D., Park, C.B., and Hunter,J	1998	Comparison of shear wave velocities from MASW technique and borehole measurements in unconsolidated sediments of the Fraser River Delta
Ivanov,J., C.B. Park, R.D.Miller, and Xia, J	2000	Mapping Poisson's ratio of unconsolidated materials from a joint analysis of surface-wave and refraction events
Miller, R.D., Xia, J., Park, C.B., and Ivanov,J	2000	Shear wave velocity field from surface waves to detect anomalies in the subsurface
Xia,J., Miller, R.D., Park, C.B., and Hunter,J and Harris, J.B	2000	Comparing shear-wave velocity profiles from MASW with borehole measurements in unconsolidated sediments, Fraser river delta, B.C Canada
Xia,J., R.D Miller, C.B Park	2000	Advantages of calculating shear-wave velocity from surface waves with higher modes
Xia,J., R.D Miller, C.B Park, and Ivanov,J	2000	Construction of 2-D vertical shear-wave velocity field by MASW technique
Miller, R.D., Xia, J., Park, C.B., and Ivanov,J	1999	Multichannel analysis of surface waves to map bedrock
Xia,J., Miller,R.D, Park, C.B, Hunter, J.A, and Harris,J.B	1999	Evaluation of the MASW technique in unconsolidated sediments

3.4 OVERALL MASW PROCEDURE

The MASW method utilizes multi-channel recording and processing concepts widely used in near-surface seismology as well as in reflection surveying for oil exploration. The fundamental mode the Rayleigh is without a doubt one of the most troublesome types of source-generated noise on reflection surveys. Rayleigh-wave energy is defined as signal in MASW analysis, and needs to be enhanced during both data acquisition and processing steps. In all kinds of surface seismic surveys using vertical sources, ground roll takes more than two thirds of total generated seismic energy and usually appears with the most prominence on the Multi-channel records. Therefore, generation of ground roll is easiest among all other types of seismic waves. The field setup is shown schematically in **Figure 13**. The method first requires measurement of

seismic surface waves generated from various types of seismic sources—such as sledge hammer—and the propagation velocities of those surface waves is analyzed, and finally the shear-wave velocity (Vs) variations below the surveyed area that is most responsible for the analyzed propagation velocity pattern of surface waves is calculated.

The most common procedure that is followed for typical MASW surveys include three major steps:

1. Data acquisition: acquiring multichannel field records
2. Dispersion analysis: extracting dispersion curves
3. Inversion: Inverting to yield shear-wave velocity variation with depth

Subsequently, a 2-D cross-sectional Vs map may be constructed through an appropriate interpolation scheme by placing each 1-D Vs profile at surface location corresponding to the middle of the receiver line. Detailed step by step procedure for each of the step is explained below and the optimum field parameters are also tabulated.

3.4.1 Field procedure: Data acquisition

This subsection is used to describe the entire field procedure for MASW data acquisition. Among the active and passive MASW, the active method is the most common type for acquiring 2-D Vs profiles. The maximum depth of investigation (Z_{max}) that can be achieved from the survey is usually 10-30 m range and varies with the type of source used. Some of the parameters related to data acquisition procedure are described below. **Table 3** describes the optimum field parameters for a typical data acquisition procedure, keeping in mind the fact that these can be

changed or updated by investigators and practitioners depending upon the requirements and in-field conditions.

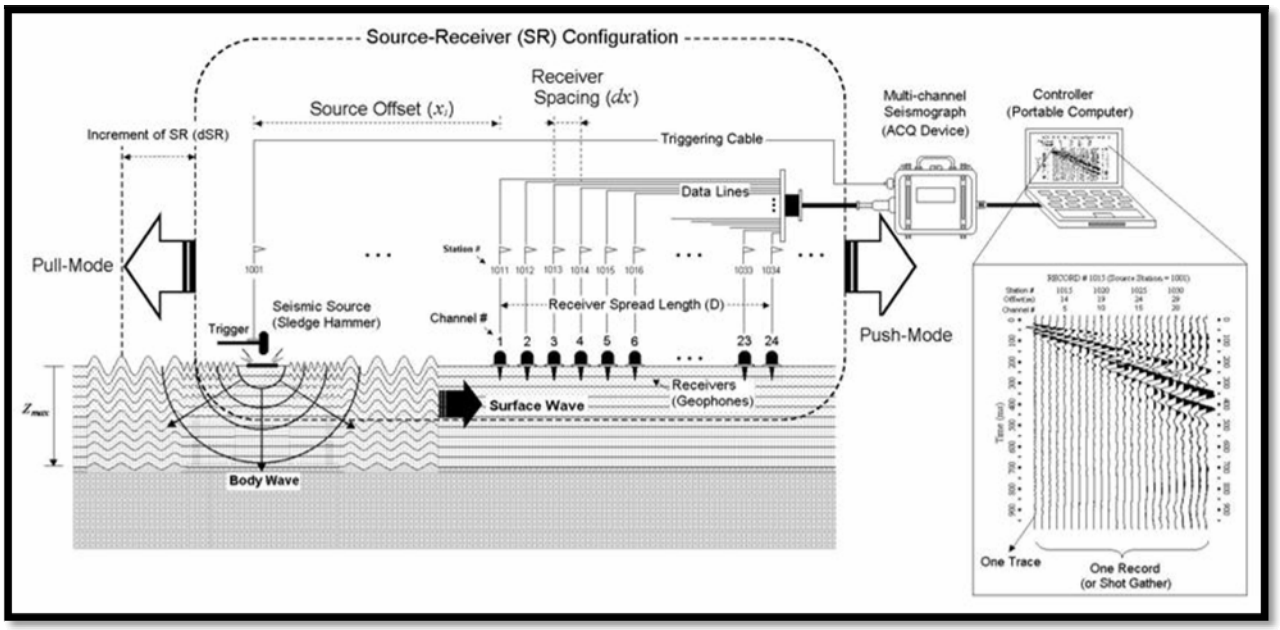


Figure 13. Schematic representation of the active MASW field survey (modified from Park, 2003)

Source

Maximum investigation depth (Z_{max}) is determined by the longest wavelength (L_{max}) of the surface waves used for the analysis as $Z_{max}=0.5L_{max}$. Also, L_{max} is governed by the energy and area of impact of the seismic source, which may be controlled type (like the sledge hammer in case of an active survey) or passive (via a car moving or other kinds of cultural noise). According to the above relation, the longer L_{max}, (deeper the Zm_{ax}) can be achieved with a greater impact power. Some of the commonly used sources include a heavy sledge hammer (10-20 lb), weight-drop etc. Using an impact plate (also called base plate) will help the source impact point intrude less into soil. The table below explains different optimum sources for different investigation depth. For unusually shallow investigation, a relatively light source has to be used

so that the dominant frequency can be shifted towards higher frequencies. Ambient noise can be significantly reduced through multiple impacts and vertical stacking of these impacts therefore is always recommended, especially if the survey takes place in an urban area.

Seismometers (geophones)

Typically, vertical (instead of horizontal) low-frequency geophones (e.g., 4.5 Hz) are recommended. Although spike coupled geophones always give the highest sensitivity, the coupling provided by a land streamer can be equally efficient and is a significant convenience in field operation. The high end of geophone frequency is not critical as in a typicaly reflection survey where any minor drop in sensitivity may become important (see Baker et al., 2003). For instance, recording and analysis of surface waves up to 450 Hz have been reported by using 4.5-Hz geophones (Miller et al., 2000) and frequencies up to 1 kHz have been detected from a hammer blow on an active glacier (Baker et al., 2001).

Field Geometry

Length of the receiver spread (D) should be directly related to the longest wavelength (L_{max}) that can be analyzed, which in turn determines the maximum depth of investigation (Z_{max}). Therefore, D usually has to be equal to or greater than Z_{max}.

$$D= m\ Z_{max}\ (1<m<3) \qquad (3.3)$$

On the other hand, receiver spacing (*dx*) is related to the shortest wavelength (L_{min}) and therefore determines the shallowest resolvable depth of investigation (Z_{min}).

$$Z_{min} = k\ dx\ (0.3 < k < 1.0)\ldots..(3.4)$$

The source offset distance (*x1*) is also a major governing factor to predict the degree of contamination by the near-field effects that indicate a confluence of all adverse influences on data acquisition, mainly because of the source being too close to the geophones resulting in "clipping" of the digital record. Although its optimum value is still under debate, a value of 20% of D is suggested as a minimum and 100% as a maximum. A larger value of *x1* and D will increase the risk of higher-mode domination and reduce S/N for the fundamental mode. Occationally while performing an active linear survey where the total profile length is significantly longer than the available geophone spread, sometimes a roll-along spread is used. In that case, the interval (*dSRC*) of source-receivers configuration move between 1*dx*-12*dx* is recommended for 24-channel acquisition. This particular variable is also directly related to the horizontal resolution. Obviously, as the number of available channels increases, the ability to acquire data along a profile without a roll-along spread is increased.

Table 3. Data acquisition parameters for active survey. Recommended values in ( )

Depth (Zmax) (ft)	Source (S) (lb)	Receiver (R) (Hz)	Receiver Spread (RS) (ft)				SR Move (dx)			Recording				
			Length (D)	Source offset (X1)	Receiver spacing (dx)		Lateral Resolution			dt (ms)	T (sec)	Vertical Stack		
					24-ch	48-ch	High	Medium	Low			C	N	VN
=50	=1 **(1)**	45-100 **(40)**	5-15 **(10)**	1-15 **(2)**	0.2-0.6 **(0.3)**	0.1-0.3 **(0.2)**	1-2 **(1)**	2-4 **(2)**	4-12 **(4)**	0.5-1.0 **(0.5)**	0.5-1.0 **(0.5)**	1-3 **(3)**	3-5 **(5)**	5-10 **(10)**
5-15	1-5 **(5)**	45-40 **(10)**	5-45 **(30)**	1-9 **(5)**	0.2-2.0 **(1.0)**	0.1-1.0 **(0.5)**	1-2 **(1)**	2-4 **(2)**	4-12 **(4)**	0.5-1.0 **(0.5)**	0.5-1.0 **(0.5)**	1-3 **(3)**	3-5 **(5)**	5-10 **(10)**
15-30	5-10 **(10)**	=10 **(4.5)**	15-90 **(50)**	3-18 **(10)**	0.5-4.0 **(2.0)**	0.2-2.0 **(1.0)**	1-2 **(1)**	2-4 **(2)**	4-12 **(4)**	0.5-1.0 **(0.5)**	0.5-1.0 **(1)**	1-3 **(3)**	3-5 **(5)**	5-10 **(10)**
30-60	>10 **(20)**	=10 **(4.5)**	30-180 **(120)**	6-36 **(30)**	1.0-8.0 **(4.0)**	0.5-4.0 **(2.0)**	1-2 **(1)**	2-4 **(2)**	4-12 **(4)**	0.5-1.0 **(0.5)**	1.0-2.0 **(1)**	1-3 **(3)**	3-5 **(5)**	5-10 **(10)**
60-100	>10 **(20)**	=4.5 **(4.5)**	60-300 **(200)**	12-60 **(40)**	2-12 **(8)**	1-6 **(4)**	1-2 **(1)**	2-4 **(2)**	4-12 **(4)**	0.5-1.0 **(0.5)**	1.0-2.0 **(1)**	1-3 **(3)**	3-5 **(5)**	5-10 **(10)**
100-150	>10 (20) **(passive)**	=4.5 **(4.5)**	100-450 **(300)**	20-90 **(60)**	4-18 **(12)**	2-9 **(6)**	1-2 **(1)**	2-4 **(2)**	4-12 **(4)**	0.5-1.0 **(0.5)**	1.0-3.0 **(1)**	1-3 **(3)**	3-5 **(5)**	5-10 **(10)**
>150	>10 (20) **(passive)**	=4.5 **(4.5)**	>150 **(450)**	>30 **(100)**	>6.0 **(20)**	>3.0 **(10)**	1-2 **(1)**	2-4 **(2)**	4-12 **(4)**	0.5-1.0 **(0.5)**	>1.0 **(2.0)**	1-3 **(3)**	3-5 **(5)**	5-10 **(10)**

*** **SR Move** represents distance in receiver spacing (**dx**) that the source (**S**) and Receiver (**R**) setup moves after acquiring data at one location; **dt** represents sampling interval in milliseconds (ms); **T** represents total recording time in seconds (sec); **Vertical stack** is the number of stacking data in seismograph's memory before being saved under different conditions of calm (**C**), noisy (**N**), and very noisy (**VN**) environment, respectively. These parameters given here are just a list of optimum parameters and are by no means definitive or required. There is a tolerance level of +/- 20% to most of these recommended values.

A one-millisecond of sampling interval (dt=1 ms) is most commonly used with a 1-sec total recording time (T=1 sec). A smaller *dt* is recommended if any body-wave processing is planned as by product and a longer T is recommended in case of extremely low velocities or if a longer receiver spread (D) is used. An excessively longer T, when used, may increase the chance of recording ambient noise. Generally, shorter dx and longer D combination is recommended. When more channels are used the Signal-to-noise ratio (S/N) will be increased during data analysis because of the redundancy as well as the possibility of increasing resolution at shallow depths. Also the effect of increasing D will be an increased *Zmax*.

3.4.2 Field procedure: Data Analysis

The first step in data analysis involves extracting dispersion curves from the data that are in turn used in the subsequent step of data inversion, whereby a proper layer (shear-wave velocity-Vs) model is determined such that the theoretical dispersion curves match the measured ones as close as possible. Usually, the fundamental mode (M0) curve is used. However, recent studies (Xia et.al., 2000a) suggest that higher-modes can also be utilized to get shear-wave velocity information.

Concept of Dispersion

In the early stage of surface wave method using monotonic vibrator exciting at a single frequency (f) at a time, the distance (Lf) between two consecutive amplitude maxima was measured by scanning the ground surface with a single sensor and an oscilloscope. Then, corresponding phase velocity (Cf) was calculated as Cf=Lf*f. This measurement was then repeated for different frequencies to construct a dispersion curve with the assumption that the fundamental mode (M0) of the surface wave dominate in the field. In early 1900's this method was used efficiently by the spectral analysis of surface waves (SASW) method. Instead of trying to measure the distance of Lf, the method is used to measure the phase difference (dp) for a frequency (f) between the two receivers a known distance apart from the relationship: Cf=2*pi*f/dp. This process is repeated for different frequencies to construct a dispersion curve. The possibility of multi-modal influence during the inversion process is accounted for with the concept of apparent dispersion curve.

While using a multi-channel approach, however, the user does not calculate individual phase velocities first, but instead construct an image space whereby dispersion trends are

identified from the pattern of energy accumulation (higher amplitude peaks) in this the frequency-wavenumber domain. Then, necessary dispersion curves are extracted by following the image trends based on the amplitude anomalies. During this imaging process, a multichannel record in time-space domain is transformed into either frequency-wave number or frequency-phase velocity domain. In order to acquire this, the phase-shift method is generally used instead of any other traditional method like pi-omega or the f-k method because it achieves higher resolution than the other methods (from www.masw.com).

The Dispersion imaging scheme

The standard data processing scheme is as follows: A multi channel field record (a) is first decomposed via Fast Fourier Transformation (FFT) into individual frequency components, and then amplitude normalization is applied to the each component (b). Then, for a given testing phase velocity in a certain range, necessary amount of phase shifts are calculated to compensate for the time delay corresponding to a specific offset, applied to individual component, and all of them are summed together to make a summed energy of (c). This in turn is repeated for different frequency components. When all the energy is summed in frequency-phase velocity space, it will show a pattern of energy accumulation that represents the dispersion curve as shown in (d). In case of multi-modal dispersion, that behavior of energy will appear as multiple energy accumulations for a given frequency as shown in (e).

3.4.3 Field Procedure: Data Inversion

Inversion in general

Inversion or inversion modelling, in general, attempts to seek the cause to a result when the result is known. On the other hand, predicting the result from the given cause is referred to as

forward modeling. An inversion is known to be unique if there is only one solution to the problem, and non-unique if multiple solutions exist. It is also called "linear" if the cause-related relationship is linear as a small change in input yields also a small change in result, whereas "non-unique" if a small change can give rise to a big change in result.

Typical MASW method inversion

The goal of a field survey and data processing in MASW is to establish the fundamental mode (M0) dispersion curve as accurately as possible. Theoretical M0 curves are then calculated for different earth models by using a proper forward modeling scheme (e.g., Schwab and Knopoff, 1972) to be compared against the measured curve. The process of inversion is based on the assumption that the measured dispersion curve represents the M0 curve only, not influenced by any other modes of surface waves. The most important issue with the inversion process is to determine the best-fit earth model among many different models as efficiently as possible. One way to check for the closeness between the measured and theoretical curves is the root-mean square (RMS) error factor. Several other types of inversion are described below.

Multi-modal Inversion

The multi-modal inversion technique utilizes both the fundamental and higher-mode curves for the inversion. This is done in order to increase the accuracy (resolution) of the final 1-D Vs profile by narrowing the range of solutions with 1-D Vs profiles otherwise equally well suited if only the M0 curve is used (Reference?). This method can also be used to alleviate the inherent problem with the inversion method of non-uniqueness in general.

Dispersion Image Inversion

The method of inversion includes the use of dispersion image data (also called phase-velocity spectra) instead of dispersion curves, and does not involve the extraction of modal curves at all (Ryden and Park, 2006; Forbriger, 2003a;2003b). This approach eliminates such drawbacks with the modal-curve based inversion such as mode-misidentification and mode-mix problems (misidentifying higher mode curve as a M0 curve) if data acquisition and subsequent processing are not properly performed. Dispersion curves when misidentified may lead to erroneous Vs profile because of the lack of compatibility in the inversion process trying to match measured and theoretical curves.

Raw Data Inversion

As the name suggests, this type of inversion utilizes the raw multichannel record instead of the one processed for dispersion imaging (Forbriger, 2003b). In the process, the scheme attempts to compare whole seismic waveforms observed at different distances from the source with synthetic waveforms generated from a forward modeling scheme. This type of approach may be advantageous over others for the fact that it is not biased by any other kind of data processing such as dispersion imaging or curve extraction. At the same time, however, it has to take into account the attenuation and interference issues, as well as layer parameters, since all of these can contribute to the shaping of a seismic waveform.

2-D Vs Inversion

This approach uses the final output of 2-D Vs profile from current typical inversion approach as input to the second phase of the inversion based on a different forward modeling scheme than previously used. The main objective of this method is to consider the smearing

effect caused by the lateral variations during dispersion analysis as much as possible by adopting another scheme accounting for the local variation of Vs. For this purpose, the Vs structure is provided by the previous output of the 2-D Vs profile as an initial starting model to account for the local variations observed within an individual field record to update a certain part of the 2D Vs model. This initial starting model most likely corresponds to the surface location of the receiver spread used during data acquisition. Iterations can be performed for a better result. The main drawback for this method, however, is that it is very computationally intensive.

3.5 TYPES OF MASW METHODS

Depending upon the source used to generate surface waves there are two basic types of MASW technique: active, where an impact source such as a sledge hammer or a weight drop is used, and passive method, wherein surface waves are generated by passively recording evergy from cultural and natural noise such as traffic and tidal motion.

The active (or active-source) survey method is the conventional mode of survey for collecting MASW. However, there are two sub categories in the passive method, both of which utilizes surface waves generated passively from ambient cultural noise such as traffic, thunder etc., and are sometimes used in MASW. The passive-remote method (Park et al., 2004; 2005) employs a 2-D receiver array such as a cross or circular layout to record passive surface waves. On the other hand, the passive-roadside MASW method (Park and Miller, 2006) adopts the conventional linear receiver array and tries mainly to utilize those surface waves generated from local traffic. For the passive-roadside method, the array is typically deployed along a sidewalk or on the shoulder of a road ,and the survey can continue in a roll-along mode for the purpose of 2-D Vs profiling.

3.5.1 Why do we need passive method?

Although one can achieve reliable Vs estimations with the active-source MASW method, the depth of investigations is typically only down to a few tens of meters (for example, 30 m). While this kind of depth is often sufficient for engineering investigations, there are other instances where the investigation depth is insufficient due to either unusual elastic properties of the near-surface materials or an usually deep investigation depth sought. Some of the commonly used active source like a sledge hammer or heavier source like the weight drop can overcome the limitation; however, the depth range gained may often be trivial as the power delivered by most of the active sources is not sufficient to achieve a distinguished gain in investigation depth (it is a strongly nonlinear relationship between depth and power). Even if such a source is invented, it would likely be uneconomical and impractical.

On the other hand, the surface waves generated from natural or cultural noise are usually of higher-energy and lower-frequency, with wavelengths ranging from a few kilometers (natural sources such as wave surf) to a few tens (or hundreds) of meters (cultural sources like traffic) (e.g., Okada, 2003), providing a wide range of penetration depths and therefore proving to be more advantageous than the active methods (Park and Miller, 2006). In addition, as the necessity of performing MASW surveys in urban areas grows, utilizing those pre-existing surface waves generated by local traffic is found to be a perfect choice recently (Asten, 1978; Louie, 2001; Okada, 2003; Suzuki and Hayashi, 2003; Yoon and Rix, 2004; Park et al., 2004).

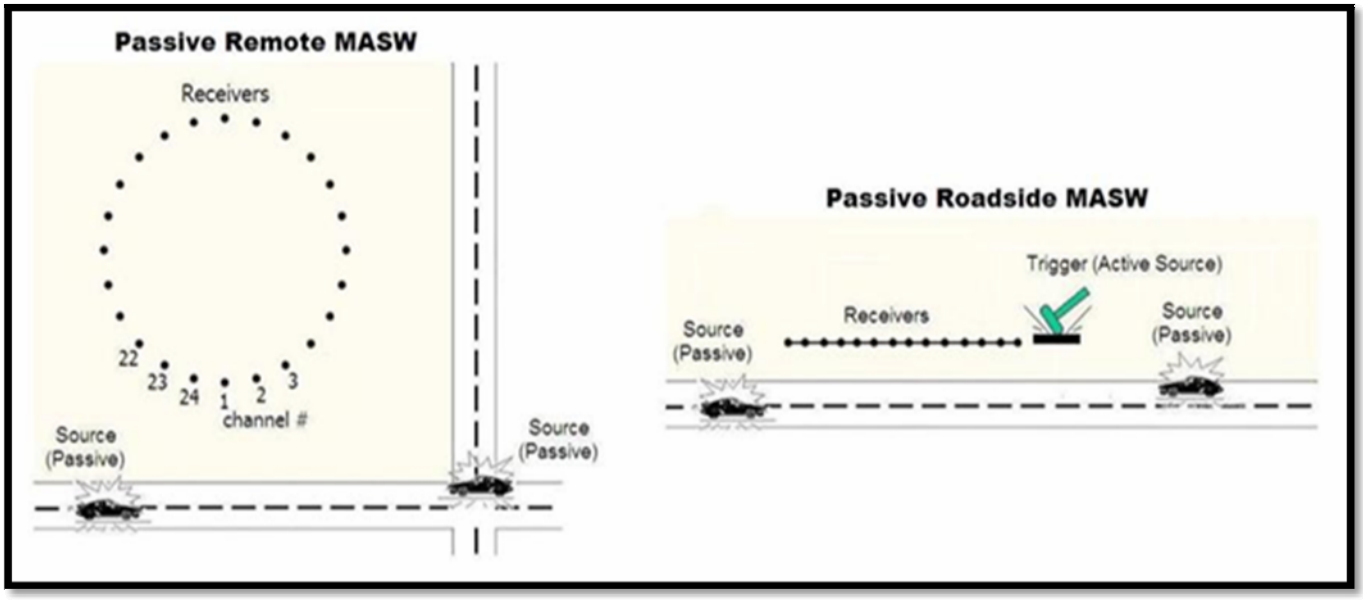


Figure 14. Typical field layout for passive remote (left) and passive roadside (right) MASW surveys

3.5.2 Types of passive MASW methods

As previously mentioned, the passive MASW methods are divided into two subtypes depending on the field logistics and the type of shear-wave velocity (Vs) profiles (1-D or 2-D) generated: passive remote (Park et al., 2004) and passive road side (Park and Miller, 2008) surveys. Examples of field layouts for both passive remote and passive roadside surveys are shown in **Figure 14**.

Passive remote survey

The former method utilizes a two-dimensional (2-D) receiver array such as circular, cross or any other symmetrical shape to record passive surface waves. Although this method involves laborious field operation and needs more space for deploying the array, results in most accurate 1-D shear-wave velocity profiles (Vs) (Park et al., 2005). For this type of survey any kind of symmetrical shape like circle, cross, square, triangular or random etc. is used. This study is

mainly focused on a study comparing some of the 2-D arrays with that of a random array in terms of its effect on dispersion analysis and shear-wave velocity extraction. Some of the commonly used 2-D arrays are shown pictorially in **Figure 15**.

Passive roadside survey

As mentioned above, this type of MASW method utilizes conventional linear receiver array and uses local traffic as noise. This method overcomes limitation with the remote in terms of area of survey and data acquisition procedures, but one has to sacrifice the accuracy of the Vs evaluation (usually <10%). Because the receivers can be laid linearly and traffic noise can be used as a source, this set up can be set along a sidewalk, median or on the shoulder of a road and just as in the active linear array, a roll-along mode can be used for the purpose of 2-D Vs profiling (from www.masw.com) . Also, while performing this survey, an active impact can be applied at one end of the array to trigger a long recording. Therefore, from a passive road side array a combined analysis of surface waves for Vs evaluation can be achieved for both shallow and deep information simultaneously.

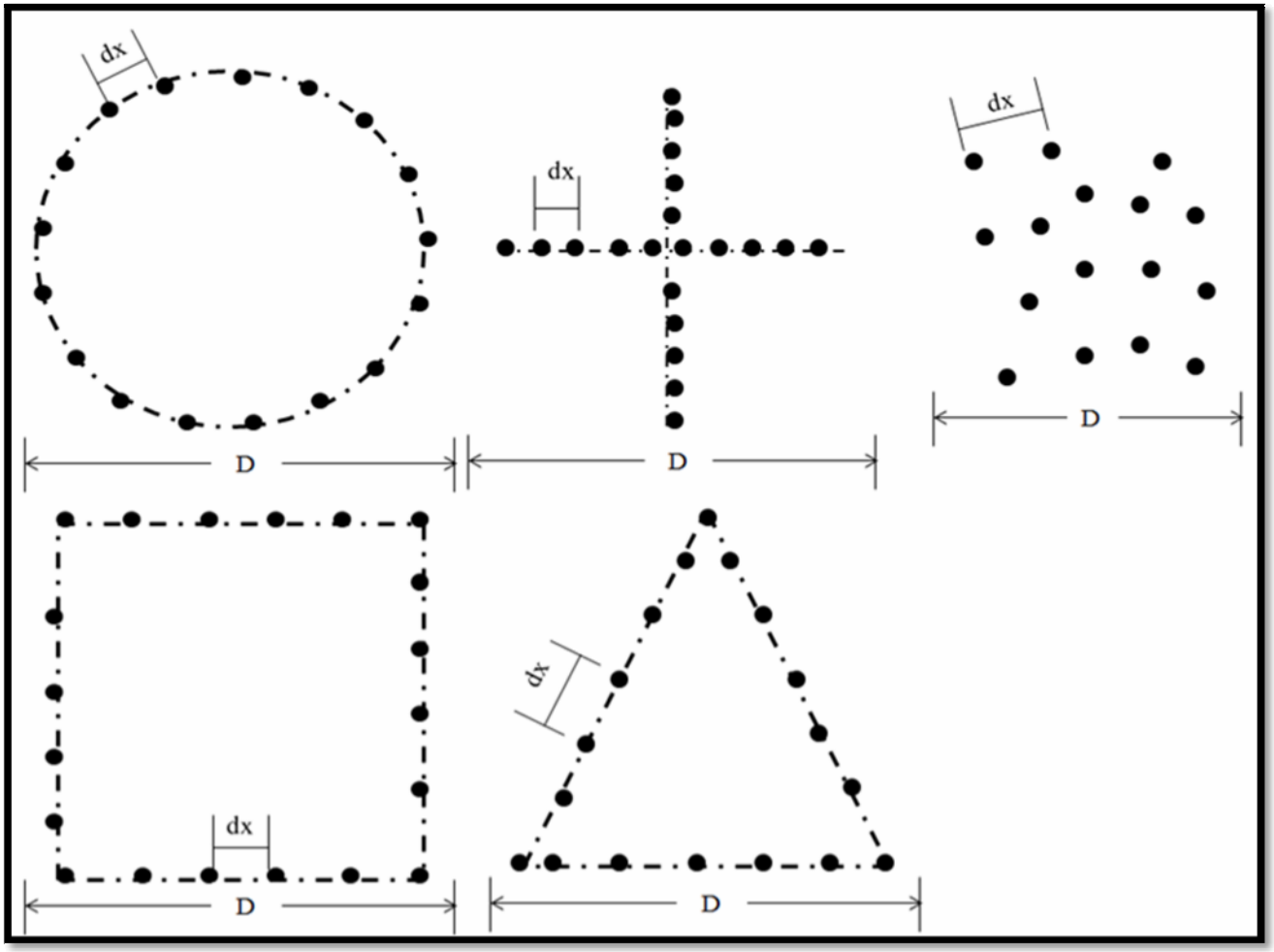


Figure 15. Examples of 2-D receiver arrays for the passive remote MASW surveys

Combined active and passive survey

In some cases it is often necessary and useful to combine dispersion images from both active and passive data: (1) to enlarge the analyzable frequency range of dispersion. (2) to better identify the modal identity of dispersion trends (active methods results in high frequency range and passive results in the low frequency range). Although some studies (e.g., Aki, 1965) suggest that the M0 obtained from passive survey are predominantly Rayleigh waves, recent studies (Park et al., 2005; 2006) reveal that there is also a strong possibility of higher modes domination.

Therefore it is suggested (Park et al., 2005) that a combined analysis would be more reliable for modal identification.

3.6 SUMMARY

The multi-channel analysis of surface waves (MASW) method is a relatively recently developed seismic method dealing with relatively lower frequencies and shallow investigation depth ranges than any other many other conventional seismic methods. The data acquisition and processing scheme results (Vs information) have proven to be highly reliable in geotechnical field, even under the presence of higher modes of surface waves and also under various types of cultural noise. The data processing steps are all automated which makes this method extremely easy and fast to implement and also very cost-effective. Due to these advantages, this method has gained significant importance in geotechnical engineering and also in other engineering communities.

CHAPTER-4

Physical Properties of the Moon

4.1 INTRODUCTON

The Moon is Earth's natural satellite and also the fifth largest satellite in the Solar system. It is the only celestial body on which humans have landed. The Moon preserves a unique history of the planetary information and early development, and also serves as a target that has recorded the space environment and cosmic radiation for billions of years (the Lunar Source book). During the last 20 years, the Moon has become an objective for long-term human exploration beyond Earth. Therefore, it has become important to understand the Moon's characteristics, especially its potential usefulness and resources that are critical for planning the human future in space.

The geology of the moon, also known as "selenology," is quite different from that of Earth. It has been identified that the moon currently has no atmosphere, does not possess any plate tectonics, has lower gravity, and cooled more rapidly than Earth due to its smaller size (*Vaniman et al., 1991*). According to the NASA Apollo scientists and geologists, impact cratering and volcanism—or a combination of the two processes—are the main reason for the complex geomorphology of the lunar surface (*Horz et al., 1991*). The geology of the moon has been studied based on many earth based telescopic observations, orbiting spacecraft readings, lunar samples and some geophysical data.

4.2 GEOLOGIC HISTORY OF THE MOON

The geologic history of the Moon has been defined in six major epochs, called the lunar geologic timescale (Wikipedia). Formed around 4.5 billion years ago (based on current hypotheses, Kleine et.al., 2005), the Moon was initially in molten state and was orbiting much closer to the Earth. Due to the tidal forces of Earth's gravity, the molten body deformed into an

ellipsoid, with the major axis pointing towards Earth. The first important event in the geologic evolution of the moon was the crystallization of the near global magma ocean. The first minerals to form in this ocean were the iron and magnesium silicate olivine and pyroxenes. Lunar samples that were brought back from Apollo missions (11, 12, 14, 15, 16, and 17) indicate that most of the lunar impact basins were formed within a very short period of time between about 4 and 3.85 Ga ago. Impacts by meteorites and comets are the only abrupt geologic force acting on the moon today and generate the majority of the regolith.

4.3 LUNAR LANDSCAPE

Impact craters, their ejecta, volcanoes, hills, lava flows and depression filled with magma characterize most of the lunar landscape.

4.3.1 The Highlands

The most distinctive aspect of the moon is the contrast between its light and dark zones. Lighter surfaces, rich in plagioclase minerals, are called the highlands while the dark surfaces, rich in iron minerals, are called maria. The highlands are anorthositic in composition, whereas the maria are basaltic (Vaniman et al., 1991). The highlands are older than the visible maria, and hence are more heavily cratered.

4.3.2 The Maria

The maria is believed to represent the large flow of basaltic lava that corresponds to low-albedo surfaces covering nearly a third of the near side. These are products of volcanic processes on the Moon. The maria ages from 1 Ga to 4.2 Ga, as indicated by radiometric dating and crater counting techniques (Neukum et.al., 1975). The youngest lavas erupted within Oceanus

Procellarum, whereas some of the oldest appear to be located on the farside. The maria are younger than the highlands given their lower density of impact craters.

Although the cause is still under debate, the maria basalts are predominantly located on the near-side hemisphere of the moon. Based on data obtained from the Lunar Prospector mission, it appears that a large proportion of the Moon's inventory of heat producing elements is located within the regions of Oceanus Procellarum and the Imbrium basin, a unique geochemical province now referred to as the Procellarum KREEP TerrainTaylor J.G., and others 1980). A special group of lunar basalts is the KREEP basalts, which are abnormally rich in potassium (K), rare earth elements (REE) and phosphorus (P).

According to terrestrial classification schemes, all mare basalts are classified as thoeleiitic, but additional sub classifications have been invented to further subdivide them into three series based on their element chemistry: high-Ti basalts, low-Ti basalts and very low-Ti basalts. The global remote sensing data acquired from the Clementine mission showed that there is a continuum of Titanium concentrations betweens these end members, and that the high-titanium concentrations are the least abundant (Taylor J.G., 1980)). Titanium dioxide abundances can reach up to 15 wt% for mare basalts, whereas most terrestrial basalts have abundances much less than 4 wt%. A major difference between terrestrial and lunar basalts is the near-total absence of water in any form in the lunar basalts. Lunar basalts do not contain hydrogen-bearing minerals like the amphiboles and phyllosilicates that are common in terrestrial basalts.

4.3.3 Impact craters

Being one of the most notable geologic processes on the Moon, impact craters are formed when a solid body, such as an asteroid or comet, collides with the surface at a high velocity (e.g., Gehrels, 1979; Shoemaker, 1983). Although the concept was quite speculative, Eugene Shoemaker conducted detailed studies of a number of craters and recognized that they are formed mainly due to impacts, shock metamorphism, being one of the main reason associated with impact events. The kinetic energy of the impact creates a compression shock wave that radiates away from the point of entry followed by rarefaction wave (e.g., Maxwell, 1977; Orphal, 1977; Croft, 1980)Reference!), which is responsible for propelling most of the ejecta out of the crater. In the final stages, there is a hydrodynamic rebound of the floor that can create a central peak.

These craters occur in all kinds of shapes and sizes ranging from tiny pits to immense diameter (Pike 1977). The South Pole-Aitken Basin is one of the largest known impact crater with diameter of nearly 2500 km and a depth of 13 km. It is also observed that the largest impact basins were formed during the early periods, as these were successively overlaid by smaller craters. Well-defined features, including a sharp-edged rim, distinguish the most recent impacts. Smaller craters tend to form a bowl shape, while larger impacts can have a central peak with flat floors. Larger craters also generally display slumping features along the inner walls that can form terraces and ledges. The largest type of impact basins, the multiring basins, can even have secondary concentric rings of raised material (Horz et.al., 1991)!). The largest impacts produced melt sheets of molten rock that covered portions of the surface that may be as thick as a kilometer. Examples of such impact melt can be seen in the northeastern part of the Mare Orientale impact basin.

4.4 THE LUNAR REGOLTIH

Regolith is a terrestrial geology term also used for the Moon. It is defined as a surface layer of fragmental and unconsolidated rock material, whether residual or transported and of highly varied character, that nearly everywhere forms the surface of the land and overlies or covers bedrock (Bates and Jackson, 1980). It has been observed from various missions to the Moon that the entire lunar surface consists of a regolith layer that completely covers the underlying bedrock, except perhaps on some very steep-sided crater walls and lava channels, where there may be exposed bedrock.

The regolith on the Moon results from uniquely different processes when compared to the processes on the Earth. On Earth, the regolith generally is produced by processes that are uniquely terrestrial—the presence of oxygen, the influences of wind and water, and the activities of life. On the airless, lifeless Moon, the lunar regolith results from the continuous impact of large and small meteoroids and the steady bombardment of the lunar surface by charged atomic particles from the sun and the stars (Mckay et.al., 1991).

Continuous meteoroid bombardment physically breaks up nearly all bedrock exposed on the Moon. As the impacts continue, the original bedrock is covered by a fragmental layer of broken, melted, and otherwise altered debris from innumerable superimposed craters. This layer is the lunar regolith.

Lunar soils are also sometimes referred to as lunar regolith and they consists of particles <1cm in size although larger cobbles and boulders, some as much as several meters across, are commonly found at the surface (Mckay et.al., 1991). Impact cratering produces much of the

pulverized material which melts and gets welded together to produce breccias and impact melt rocks that make up a significant portion of the regolith and add to its complexity.

The regolith thickness is believed to not exceed 10 to 20 m, since about 4 b.y. ago the impact flux on the lunar surface has been relatively low, and a regolith only a few meters thick is adequate to shield the underlying bedrock almost indefinitely. Astronauts have drilled to a depth of approximately 3 m in the regolith at some Apollo sites), and estimates based on grain-size distributions suggest that the maximum thickness of the regolith may not exceed 20 m, at least in these locations (McKay et al., 1974). Current consensus is that the regolith is generally about 4-5 m thick in the mare areas but may average about 10-15 m in older highland regions. Below this layer lies what is commonly known as megaregolith, a complex zone consisting of large-scale ejecta and impact-fractured, brecciated bedrock (Peeples et al., 1978; Langevin, 1982). It should be noted, however, that there is no large-scale survey of thickness in existence.

As the formation and evolution of the lunar regolith is a complex process, its nature and history is determined mainly by two random mechanisms. 1) destructive: the excavation of existing regolith by impact craters; and 2) constructive: the addition of layers of new material that are excavated from either near or distant impact craters. Also, the solar and cosmic radiations form layers on top of the regolith. During this process, the dust particles form microcraters, and solar-wind atomic particles are trapped in the outer layers of regolith grains, while high-energy particles produce distinctive nuclear reactions to depths of several meters (Mckay et al., 1991)!).

4.4.1 Importance of the lunar regolith

The lunar regolith is the actual boundary layer between the solid Moon and the matter and energy that fill the solar system. The regolith is the source of virtually all our information about the Moon. Both physical and chemical properties that are known about the Moon to date have been measured from samples, both rocks and soils, collected from the regolith. All the experiments conducted by astronauts on the Moon or remotely monitored from the Earth are done on or in the regolith layer. For example, the heat flow measurements and the seismic data acquired were all acquired on the regolith.

Because of its ubiquity, it can be inferred that the regolith is and will be the raw material used for lunar base construction, mining, road building, and resource extraction when permanent lunar bases are established in the near future (e.g., Taylor, 1997). The lunar regolith information has been mainly obtained from samples returned from both manned and unmanned missions to the Moon. Many physical and mechanical properties were directly measured during experiments on the Moon itself. For instance, the penetration depth of the lunar module provided an estimate of regolith compressibility. Such geotechnical properties are extremely important for any type of engineering ventures and are discussed later in the chapter. However, the majority of the information is at a point only, and any degree of lateral heterogeneity is essentially unknown.

4.4.2 Physical properties of the lunar regolith

This section will outline the physical properties of the lunar surface, determined at depths varying from few micrometers to a few tens of meters. The measured or inferred properties include geotechnical properties (needed to evaluate engineering problems), electrical and electromagnetic properties, and the reflection and emission of radiation. Most part of these data

have been derived from The Lunar Source book, Chapter-7 on the Lunar regolith written by Mckay and others (1991) and reference there in.

The lunar regolith mainly consists of five basic particle types: crystalline rock fragments, mineral fragments, breccias, agglutinates, and glasses. Considering the facts that the moon contains fewer number of minerals when compared to the Earth, and also the fact that the continuous meteoroid impact has converted the lunar surface materials into well-graded silty sand that has reached steady-state in thickness, particle size distribution, and other properties at most locations on the moon. In that regard, the lunar regolith is distinctly different from typical terrestrial materials. The absence of lunar atmosphere as well as the lack of water and organic material in the regolith constrain the physical properties of the lunar surface material to relatively narrow, well-defined range. The primary factors that affect the physical properties are bulk density, relative density, and temperature. These properties have been measured in situ by robots and astronauts, in the laboratory from the returned samples, and also from remote sensing data (Carrier et al., 1991)!).

With the studies done so far, the ranges in magnitude of geotechnical properties of lunar materials are less than those that occur in most surficial materials on the Earth. This is because of the fact that there are no weathering agents on the Moon (e.g., running water, wind, or glaciations). As previously mentioned, the principle process by which lunar soil is formed is meteoroid impacts that produce a heterogeneous and well-graded (poorly-sorted) soil. Water, clay minerals or organic materials do not affect the soils on the moon. In fact, the number of detected minerals in lunar soils is much less than that on the Earth (Papike et al., 1982)!). Most of the soil particles are made up of fragments of rocks, minerals, and glass stuck together with glass (agglutinates).

As a result of fairly negligible amount of variation in the soil particles, the geotechnical variations in the lunar soils have been previously determined to vary only in a narrow range, and the most significant variable is the relative density that is effected by particle size distribution, bulk density, specific gravity, and porosity. These properties, however, have an influence on important Earth-centric physical properties such as shear strength, permeability, bearing capacity, slope stability, and trafficability. Parameters like bearing capacity, slope stability, and trafficability determine the practical consequences of the geotechnical index and engineering properties of the lunar regolith. And the variations in these parameters mainly depend on the soil density and the shear strength measurements. These characteristics will be discussed below in detail.

Particle size distribution

Particle size distribution on the Moon is an important parameter that controls to various degrees the strength and compressibility of material, as well as its optical, thermal and seismic properties (Carrier, 1973). Sieving methods are generally used to determine the particle size distribution of an unconsolidated material for particle sizes > 10 μm. And for those < 10 μm, scanning electron microscope (SEM) image analysis or Coulter-counter methods are usually applied (Butler and King, 1974; Mckay et al., 1974; Heiken, 1975). The particle size distribution is presented either graphically as histograms or may be characterized by some standard statistical parameters such as mean particle size, median particle size, sorting, skewness, and kurtosis (Folk, 1968; Koch and Link, 1970). The majority of lunar soil samples fall in a fairly narrow range of particle-size distributions (Carrier, 1973). The median particle size is 40 to 130 μm with a mean of 70 μm. Around 10 to 20% of the soil is finer than 20 μm, and a thin layer of dust

adheres electrostatically to everything that comes in contact with the soil: spacesuits, tools, equipment, and lenses (e.g., Carrier, 1973).

Particle shape

The shapes of individual lunar soil particles are extremely anisotropic and range from spherical to extremely angular (Mahmood et al., 1974a!). The particles in general are elongated and therefore they tend to pack together with a preferred orientation of the long axes. This orientation—which was found in lunar core samples—was found to be dependent on the mode of deposition (Mahmood et al., 1974a). Because of this preferred particle orientation the physical properties of the lunar soil in situ are expected to be anisotropic. Also, many particles are not compacted due to their irregular and reentrant surfaces. These particle irregularities have a significant impact on the compressibility and shear strength of the soil. Thus, it can be inferred from the above studies that particle shape has a great significant influence on bulk physical properties and thus Vs.

Specific gravity

The specific gravity of the lunar regolith has been measured for Apollo 11, 12, 14, 15, and 17 soils. Techniques used for measuring include nitrogen pycnometry, helium pycnometry, water pycnometry, air pycnometry, and suspension in a density gradient. Average specific gravity of a given lunar soil is related to the relative proportions of different particle types; i.e., basalts (>3.32), breccias (2.9 to 3.1), and agglutinates & glasses (1.0 to >3.32). The suggested value for general scientific and engineering analyses of lunar soils is 3.1 units (generally range between 2.3 to > 3.2).

Bulk density, relative density and porosity

The in-situ bulk density is a fundamental property that influences bearing capacity, slope stability, seismic velocity, thermal conductivity, electric resistivity, and the depth of penetration of ionizing radiation. Remote sensing studies of the lunar surface suggested a bulk density value ranging from 0.3-0.4 g/cc (Jaffe, 1964 & 1965) (Halajian, 1964) whereas that measured in returned core samples from various studies (Scott et al., 1971; Houston and Mitchell, 1971; Carrier et al., 1971 and 1972a; Vinogradov, 1971) range from 0.75 to 2.29 g/cc. In situ robotic measurement values ranged from 0.8 to 1.7 g/cc (Christensen et al., 1967; Cherkasov et al., 1968 etc.)!) . Representative values range from 1.45 to 1.79 g/cc, depending on depth, for intercrater areas. At present the average bulk density of the top 15 cm of lunar soil is 1.5 g/cc and top 60 cm is 1.66 g/cc These results were based on the penetrometer measurements made by Lunakhod 1 and on the Apollo 14, 15, and 16 missions (Mitchell et al., 1974)

While bulk density of a given soil can vary over a wide range—depending on how the particles are assembled—for a granular soil, such as lunar soil, it is common to express the degree of particle packing by means of the relative density, D_R, defined as

$$D_R = (e_{max} - e)/(e_{max}-e_{min}) \times 100\%.....(4.1) – \text{(Lambe and Whitman, 1969)}$$

where e is the void ratio of the soil sample or deposit as it presently exists (corresponding to the porosity, n, or bulk density, ρ); e_{max} and the e_{min} correspond to the maximum (n_{max}) and minimum (n_{min}) porosity. As an alternative formulation, the relative density can also be expressed as 4.2 and 4.3 because of the relationships among void ratio, porosity, and bulk density:

$$D_r = ((1-n_{min}) / (1-n)) \text{ x } ((n_{max}-n) / (n_{max}-n_{min})) \text{ X } 100\%.....(4.2)$$

Or

$$D_r = ((\rho_{max}) / (\rho)) \times ((\rho - \rho_{min}) / (\rho_{max} - \rho_{min})) \times 100\% .....(4.3)$$

The relative density values are qualitatively described as follows:

Relative density %	Description
0-15	Very loose
15-35	Loose
35-65	Medium
65-85	Dense
85-100	Very dense

Physical properties such as thermal conductivity, seismic velocity, shear strength, compressibility, and dielectric permittivity are all dependent on the in situ relative density as well as the absolute bulk density. The in-situ relative density of lunar soil has been found to be about 65% (medium to dense) in the top 15 cm, increasing to more than 90% (very dense) below a depth of 30 cm (Carrier et al., 1991)!). These values are much higher than the 65-75% limit obtained in soils at terrestrial construction sites. This implies that lunar soils were not emplaced by some type of sifting mechanism, but were instead extensively shaken and densified, likely as a consequence of the aforementioned repeated impact events.

Porosity (n) of lunar soils is measured in situ by combining the best estimates of bulk density and specific gravity.

$$n= 1-\rho/G\rho_w = 1-\rho/(3.1)\ (1) =1-\rho/3.1 .....(4.4)$$

The average porosity in the top 30 cm are often measured to be ~50%. These measurement values combines the inter-, intra- and subgranular porosity. The intragranular porosity is the space between particles, intergranular porosity is the space created by reentrant surfaces on exterior of particles, and subgranular porosity is the voids enclosed within the interior of the particles.

Engineering properties

Compressibility describes the volume change, or densification, that occurs when a confining stress is applied to a material. On the Moon this has been measured with 1-D odometers on the Apollo 12 and Luna 16 and 20 missions (Leonovich et al., 1974 a, 1975)!). The compressibility is usually measured by a factor called the compression index, C_c, that is defined as the decrease in void ratio occuring when the stress is increased by an order of magnitude;

$$C_C = - \Delta e / \Delta \log \sigma_v \ldots..(4.5)$$

where, Δe=change in void ratio and $\Delta \log \sigma_v$ =change in logarithim of applied vertical stress.

Carrier and others (1972b, 1973c) measured the compression index from Apollo 12 and Luna 16 and 20 missions and found that C_C varied from 0.01 to 0.11, depending on the initial density and the applied stress. The representative parameters are;

- 0.3 C_C for loose soil

- 0.05 C_C for dense soil

- 0.003 C_r (recompression index)

- 0.45 coefficient of lateral stress (K_0) for normally consolidated soil

- 0.7 K_0 for recompacted soil

Shear strength is typically calculated from Mohr-Coulomb equation.

$$T= c + \sigma \tan\varphi \ldots..(4.6)$$

where T is the shear strength (kPa), c is cohesion (kPa), σ is the normal stress (kPa), and φ is the friction angle (degrees). Shear strength, therefore, consists of two components: a cohesive component that is independent of the applied stress, and a frictional component that is directly proportional to the normal stress. Shear strength is a critical parameter because it governs other important engineering properties such as bearing capacity, slope stability and trafficability. The cohesion ranges from 0.52-1.6 kPa for a depth of 0-60 cm and the friction angle ranges from 42-49 for the same depth variations. Cohesion increases sharply with depth, increasing by factors of 5 to 7 within ~1/2 meter of surface (after Mitchell et al., 1972d, 1974)!).

For the present, these suggested shear strength parameters may be sufficiently accurate for the design of lunar structures and construction activities. But at later stages in the human development of the moon, heavy structures or deep excavations will likely to be constructed. At that point a more detailed understanding of the shear strength under high stress conditions is key.

Regolith seismic properties

The *P*-wave velocities measured in the regolith are very low and uniform ranging from 92 to 114 m/sec (likely due to brecciation and high porosity) with an average of 105 m/s (Watkins and Kovach, 1973). The seismic Q factor of lunar regolith is ~200 at velocity of 105 m/s, which is only slightly higher than that found on soils of Earth (Baker et al., 2002).

Permeability and Diffusivity

The coefficients of permeability and diffusivity are used to evaluate the movement of a fluid through a porous solid medium. Although no direct values have been measured for lunar soils, approximate values are presented here.

The coefficient of permeability defines the quantity of flow of a fluid through a porous medium in response to a pressure gradient. In hydrology studies, the steady state flow of an incompressible, nonreactive liquid is given by Darcy's law;

$$Q = K (\rho g_m / \mu) i A$$

where Q=flow rate (m3/s); K= absolute permeability (m2); ρ=density of the liquid (kg/m3); g_m= acceleration due to lunar gravity (m/s2); μ= viscosity of liquid (N-s/m2); i=hydraulic gradient (m/m); and A= cross-sectional area normal to the flow (m2). The size and shape of pore spaces and independent of the properties of the liquid control the coefficient of permeability for a given arrangement of particles. Based on a test firing of the Surveyor 5 vernier engine on the lunar surface, the permeability of the soil to a depth of about 25 cm was calculated to be 1-7×10 m2 (Choate et al., 1968) that is considered to be consistent with the fine-grained nature of soil.

The diffusivity coefficient defines the molecular flow of gas through a porous medium in response to a concentration gradient and depends on the gas composition, the pressure and the temperature, and the particle size and shape of the soil. Martin et al., (1973) measured the diffusivity of noble gases-He, Ar, and Kr to be 7.7, 2.3, and 1.8 cm^2/s respectively, on lunar regolith samples.

Bearing capacity, slope stability and trafficability

The next few paragraphs relate to the important practical consequences of the geotechnical index and engineering properties of the lunar regolith. Bearing capacity is the parameter that describes the ability of a soil to support an applied load, such as a vehicle, a structure or even an astronaut. Two types of bearing capacity exist. Ultimate bearing capacity defines the maximum possible load that can be applied without causing gross failure, such as overturning of a structure. The soil density, its shear strength, and the size of the footing therefore control ultimate bearing capacity. If density and shear strength can be measured in situ, then the ultimate bearing capacity vs. footing width can be calculated. Allowable bearing capacity, on the other hand, defines a lesser load that can be applied without exceeding a given amount of settlement. This factor is controlled by the compressibility of the soil and the acceptable amount of settlement for a given structure.

Slope stability is based on the ability of a structure (or a slope) to remain in place without a support. There are many methods developed over years to evaluate the stability of soil slope (cf. Taylor, 1937, 1948; Bishop, 1955; Lambe and Whitman, 1969). It is much simpler to evaluate the slope stability on the Moon due to the absence of water. The factor of safety, F.S., against slope failure in case of Moon can be calculated by using the following equation;

$$F.S. = N\frac{\rho g_m h}{c} \qquad \text{……..(4.7)}$$

where ρ=density of soil; c=cohesion of soil; gm=acceleration of gravity on the moon; h=height of slope; and N=stability number, which is a function of friction angle, Φ, of the soil and the slope angle, β.

Two different kinds of slope stability need to be calculated. The first kind includes constructed slopes like an excavation, a compacted embankment, or a dumped pile. The safe depth in an intercrater area may be calculated by combining values for the in-situ density with the in-situ shear strength (Carrier et a., 1991)). The other slope type are the natural slopes; however, very little is known about the stability of natural lunar slopes. Initially, when there was no lunar landing, scientists thought that the hills and mountains were stronger than the mare basins as the hills had slopes and the maria were relatively flat. Cone penetrometer tests obtained during some lunar missions (Leonovich et al., 1974a, 1975!) indicate that the soil on the slopes is actually somewhat weaker than the soil in the flatter intercrater areas (~ 70 cm).

While the reasons for slope failures on Earth are mostly due to ground water table fluctuations, erosion from running water, and occasionally by tectonic activity, on the Moon the triggering mechanism is presumed to be the seismic vibrations produced by meteoroid impacts. While Houston et al. (1973) suggested that meteoroid impacts are an insignificant factor for slope degradation except on very steep slopes, Carrier et al. (1973) suggested that outgassing during the shearing of lunar soil could produce a fluidized flow condition, thereby resulting in large run-out distances for the transported material.

Trafficability is the capacity of a soil to support a vehicle and to provide sufficient traction for movement. Initially and before the first lunar landing, it was believed that trafficability on the lunar surface would be poor and that the movement of vehicles would be very difficult. As we know today, however, any vehicle with round wheels will perform satisfactorily on the lunar surface. The primary limitations on the trafficability of the lunar soil are speed and slope climbing. The speed of the Lunar Reconnaissance Vehicle was constrained by the irregularity of the cratered surface, coupled with the low lunar gravity, and can be

increased only by modifying its dynamic response and/or by constructing permanent roads. The lunar vehicle energy is influenced by three components: soil compaction, roughness, and elevation changes. These all parameters can be estimated from empirical equations developed by Bekker (1969)

$$R_c = \left(\frac{bk}{n+1}\right) z^{n+1} \quad \ldots\ldots(4.8)$$

where R_c = Soil Compaction Resistance Per Wheel (N); b= wheel width of ground contact (cm); $k=k_c/b+k_\Phi$ =soil consistency $[N/(cm)^{n+2}]$; k_c=cohesive modulus of soil deformation $[N/(cm)^{n+1}]$; k_Φ=frictional modulus of soil deformation $[N/(cm)^{n+2}]$; z=wheel sinkage (cm).

Although some of these parameters can be estimated, there are some isolated areas of soft soil on the lunar surface that could immobilize a vehicle. Therefore future lunar surface vehicle design and operation will need to take into account such soil areas and other impediments. More flexible vehicles may be needed for adverse conditions, something like a four-wheel-drive vehicle that are used on Earth and can be equally applicable to the Moon.

4.5 SUMMARY

In summary, therefore, the following are either known from in-situ measurements, determined back on Earth with lunar specimens, or estimated from anecdotal evidence:

Compared to terrestrial soils, lunar soils

- Lack organic matter and clays
- Contain abundant glass
- Have much higher relative densities

Lunar soils

- Accumulate at a rate of 1.5 mm/million years
- Dominated by <1 mm particles
- Mean particle sizes of 40 to 130 μm
- Average particle size of ~ 65 to 70 μm
- Representative specific gravity of 3.1
- Bulk density that ranges from 1.45 to 1.79 g/cc, depending on depth
- Relative density is greater than 65% and quickly exceeds 90% within ~1/2 m of surface
- Porosity ranges from ~44 to ~54%, decreasing with depth
- Cohesion of soils in intercrater areas is greater than that on interior crater walls but less than that on crater rims

CHAPTER-5

Exploring Multi-Channel Analysis of Seismic Surface Waves with Random Receiver Arrays for Potential Lunar Exploration

Note: This Chapter is written specifically to be submitted directly as a manuscript. Therefore, there is some repeated material and overlap with previous and subsequent chapters.

Yeluru, P.M., Baker, G.S., Park, C., and Perfect, E.A., in prep.

ABSTRACT

Understanding the physical and engineering properties within the upper 30 meters of the lunar subsurface will be critical as lunar exploration advances and deployment of large structures, landing of large spacecraft, and excavating for mining or human habitation on the moon becomes necessary. Advances in multi-channel seismic acquisition, either active or passive, in acquiring reliable 1-D or 2-D shear wave velocity profiles have greatly improved our ability to determine the engineering properties (e.g., Poisson's ratio) of Earth's shallow subsurface, especially when using the seismic multi-channel analysis of surface waves (MASW) technique. A new scheme of using randomly distributed geophones that would be deployed from a mortar-type device, instead of a conventional linear array, is necessary for lunar exploration because of the substantial logistical challenges associated with arranging an accurate linear or circular array robotically. Results indicate that robust dispersion curves and thus subsurface models of engineering properties can be obtained using random array geometry. Based on the extreme logistics imposed by lunar exploration and the anticipated engineering needs of lunar exploration, information obtained on the Moon (e.g., V_{30}) using this technique should prove to be a critical component of data acquisition. This study focuses on testing the effectiveness of a random receiver array judged by the accuracy of the dispersion curve processed from the random-array data. For the purpose of comparison, the effectiveness of the dispersion curves obtained from the newly developed method will be compared with the conventional linear array data that was collected at the same site.

5.1 INTRODUCTION

The geology of Earth's Moon has been studied via Earth-based telescopic observations (e.g., Kuiper, 1960), orbiting-spacecraft readings (Apollo, Luna missions), Lunar samples (also returned from Apollo and Luna missions), and geophysical data (e.g., Khan et al., 2000; Khan et al., 2007). The physical properties of Lunar soils and rocks have been determined *in situ* by robots and astronauts at depths varying from a few micrometers to a few tens of meters of the subsurface, in the laboratory on returned samples, from remote sensing, and from Lunar orbit (Carrier et al., 1991; Mitchell et al., 1973; 1974). Geotechnical properties (the properties of a planetary surface needed to evaluate the engineering problems) of the interior as well as the mechanical properties of soil and rock, and the electric/electromagnetic properties are critical in understanding the complexities of the lunar surface. Seismic signals were incorporated into many of the experiments performed by astronauts during the Apollo missions with the objective to map the deep Lunar interior (Nakamura et al., 1973). However, using seismic signals to determine the engineering properties (e.g., Poisson's ratio) of the shallowest layers (upper 30 m) of the Lunar subsurface has not been attempted in any lunar mission. The shear wave velocities of near surface materials (such as soils) are of fundamental interest on Earth in many environmental and engineering studies and in construction safety (e.g., Park et al., 1999). For example, the average shear-wave velocity of the upper 30 m of the subsurface (V_{30}) plays a key role in soil classification and is one of the critical parameters in the construction industry and earthquake safety (Xia et al., 2007). The V_{30} parameter is also a critical parameter in slope-stability analysis. Understanding the physical properties within the upper 30 m of the Lunar subsurface is important as lunar exploration advances. The physical properties will be critical when building large structures, landing large crafts, mining for resources, and tunneling for human habitation. A

prior knowledge of the load-bearing capacities and structural integrity of the surface layers will become important for future lunar exploration.

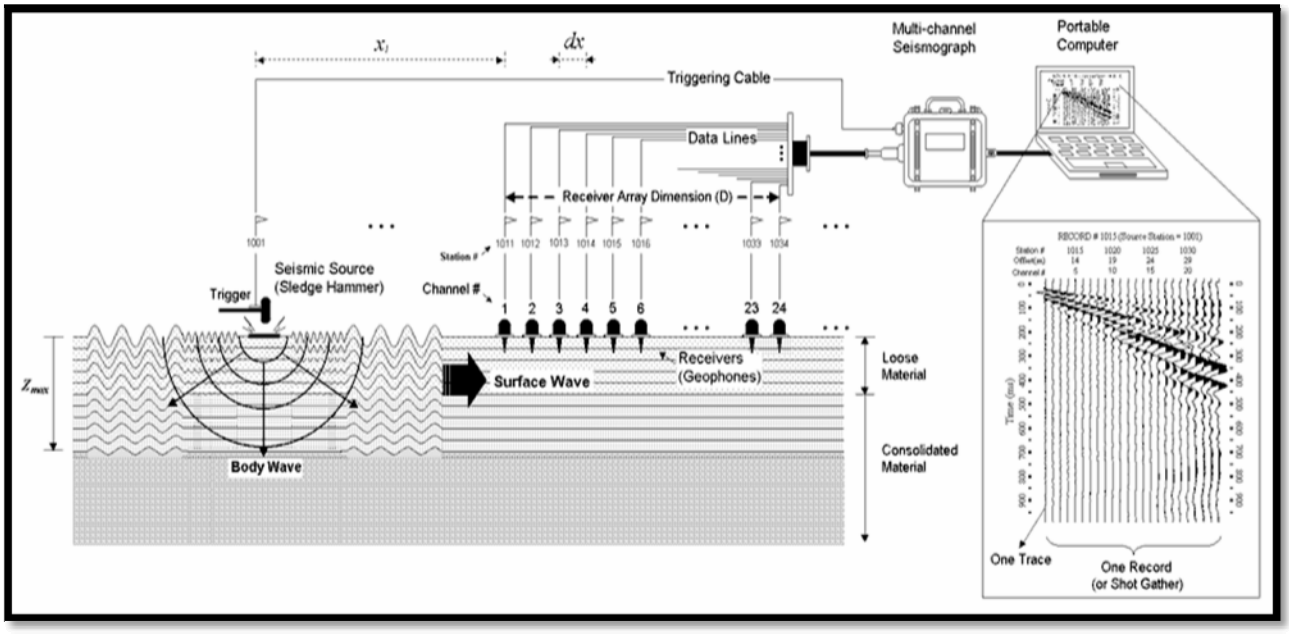
The multi-channel analysis of surface waves (MASW) seismic method (Park et al., 1999) utilizes a multi-channel seismic recording system to estimate near-surface S-wave velocity from dispersion property of high-frequency (>2 Hz) Rayleigh waves (**Figure 1 a**). The method has been steadily gaining popularity and attention from the near-surface geophysical and engineering communities, and has been successfully applied to various near-surface problems, such as mapping bedrock (Miller et al*.,* 1999), studying pavement structures (e.g., Ryden et al*.,* 2006) and liquefaction studies (e.g., Nazarian et al*.,* 1983). The MASW uses a multi-channel array, which makes it possible to distinguish the fundamental-mode from higher modes and body waves. Depending on the source used to generate surface waves, there are two types of MASW surveys: the active method that utilizes a controlled impact source like a sledge hammer, and the passive method that utilizes ambient noise such as vehicle traffic or tidal motion. The active method is considered to be the conventional mode of survey, collecting data in a roll-along mode using an active seismic source and a linear receiver array. The passive remote method utilizes ambient cultural noise such as traffic, thunder, tidal motion, etc., and employs a 2-D surface receiver array such as a cross, circular, or random array to record passive surface waves.

A new scheme of using randomly distributed geophones that would be deployed from a mortar-type device instead of a conventional linear array is necessary for lunar exploration because of the substantial logistical challenges associated with arranging an accurate linear or circular array robotically. For example, rovers that are used to move around on lunar surfaces cannot easily move in a linear fashion or in a symmetrical circular motion to arrange the geophones due to constraints imposed by surface clutter such as rocks and boulders. Therefore it

is difficult to arrange the geophones in an organized manner on a lunar surface. The principle objective of this study is to assess our ability to obtain accurate dispersion properties that can help determine engineering properties for the upper 30 m of the subsurface by using the 1-D shear wave profiles obtained using random array of geophone placement.

5.2 OVERVIEW OF MASW METHOD

In order to acquire typical MASW data, multiple receivers (usually 24 or more) are deployed with even spacing along a linear array with all the receivers connected to a single recording device (seismograph) (**Figure 16**). Each channel is dedicated to recording vibrations from one receiver. Each multi channel record, also known as a shot gather, consists of multiple number of time series (called traces) from all the receivers in an ordered manner. The recorded shot gather can have various patterns depending on the type of receiver array used. A typical shot gather for a linear array is shown in **Figure 16(a).**



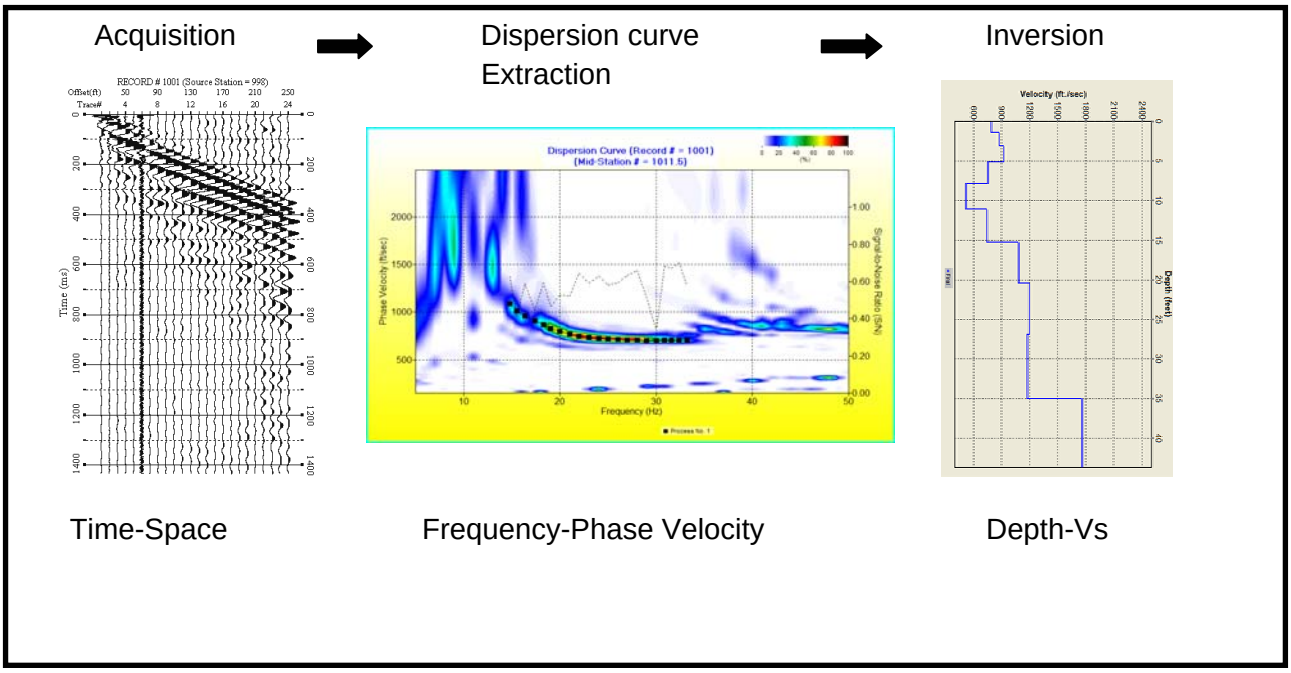


Figure 16. **(a)** Typical multichannel seismic surface-wave experiment setup and (b) MASW data processing procedure (modified from Park et al., 1999)

The data processing usually consists of three steps (**Figure 16 b**): the first step involves converting the acquired SEG-2 format data into KGS format, and then sorting data by applying field geometry based on source and geophone locations. The second step is dispersion analysis which involves extracting dispersion curves (one for each record). One of the unique features of surface waves is that they are dispersive, that is, the phase velocity of surface waves in a vertically heterogeneous medium is dependent on frequency. This property of surface waves is known as dispersion. This is the key element in surface waves allowing them to be used to determine the variation of material properties with depth.

Generating a good dispersion curve is a critical step, since the final result of a MASW survey (either a 1-D shear wave velocity profile or a 2-D shear wave velocity map) depends on the frequency- phase velocity relationship analyzed in this step. This process is achieved by first converting the data from the time-space domain to frequency-phase velocity domain by using a

suitable mathematical transformation process like the pi-omega transform (McMechan and Yedlin, 1981) or the phase-shift method (Park et al., 1998). This type of 2-D (i.e., time and space) transformation generates image of dispersion patterns in both fundamental and higher modes through successive energy accumulations, instead of calculating individual phase velocities one by one. Among multiple modes of dispersion possibly recorded, we are particularly interested in the fundamental mode dispersion curve, the one that is at the lowest velocity range. The last step of the MASW data processing involves inverting the surface wave dispersion data in order to obtain a 1-D seismic shear wave velocity profile. The inversion process involves back-calculating shear wave velocity variation with depth that yields the best fit between theoretical and measured dispersion curves (e.g., Xia et al., 2003).

5.3 MASW DATA COLLECTED FOR RANDOM RECEIVER ARRAYS

Multichannel seismic data were acquired on the University of Tennessee agricultural field test site in eastern Tennessee USA using two 24-channel Geometrics Geode seismographs with 40 Hz vertical geophones. The seismic source was the Thunderbolt™ impact source, which produces results similar to a sledge hammer. The receivers were spread randomly within a 10 m × 10 m grid and data were acquired at 13 shot points around the grid (**Figure 17**). Using a random number generator, forty eight X-Y coordinate pairs (between zero and ten) were generated for the random array. Corresponding X and Y coordinates were then mapped on the ground (inside the 10 m × 10 m grid) using a tape measure. A time sampling interval of 0.5 ms and a total recording time of 1000 ms were used during data acquisition. No acquisition frequency filter was applied during the recording. To increase signal-to-noise ratio, data from three impacts at the same impact station were vertically stacked.

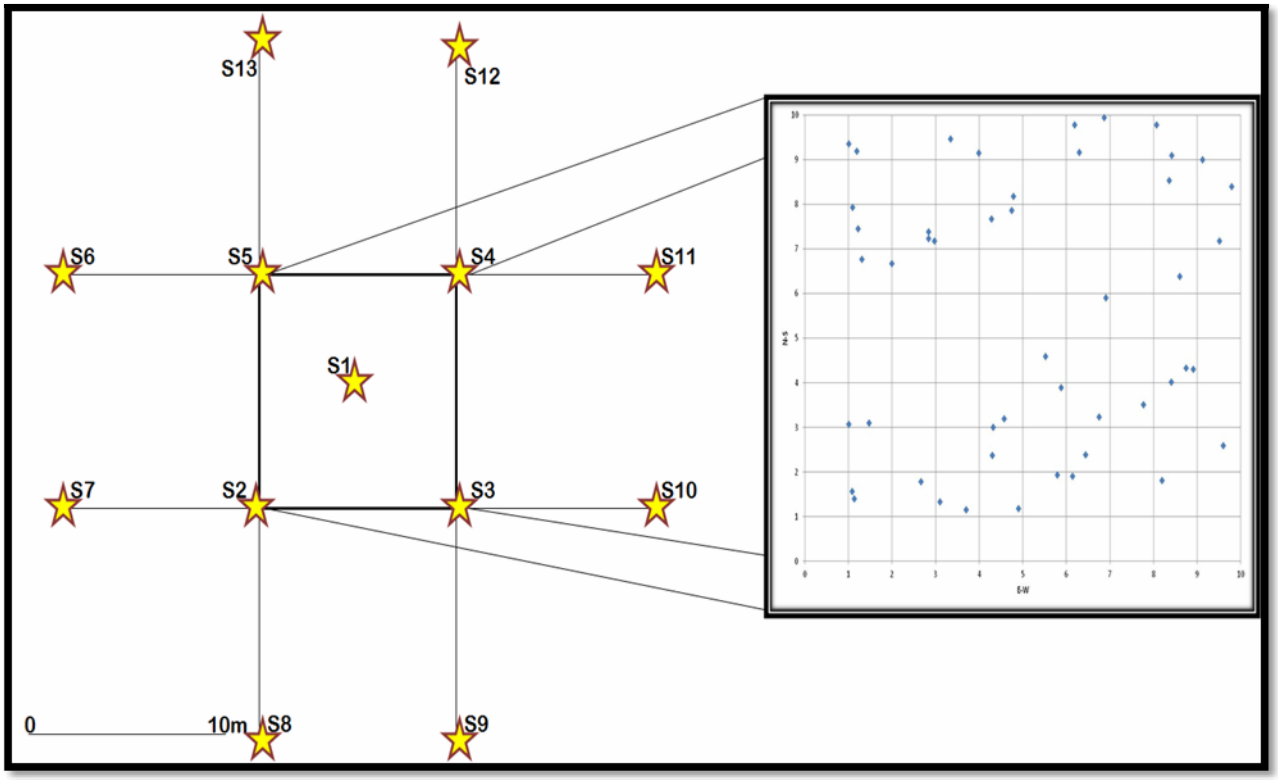


Figure 17. The figure on the left represents the shot point locations as deployed on the ground. There are total 13 shot points (shown as s1, s2, etc.) from which data was collected. The distance between each shot point location is 10 m. The figure on the right represents the random arrangement of geophones (small circles) inside a 10 m×10 m grid

The acquired data (**Figure 18**) were processed using SURFSEIS software (developed by the Kansas Geologic Survey). The various fundamental mode frequencies measured during this experiment range from 10-50 Hz; the phase velocities range from 100-2000 m/sec. The data acquisition parameters used for the two arrays are tabulated in **Table 4**.

Table 4: Summary of data acquisition parameters

Survey Type	Random	Linear
File name	"Random_MASW .dat"	Linear_MASW.dat
Survey purpose	1-D Vs profiling	1-D Vs profiling
Data format	SEG-2	SEG-2
Acquisition	48-channel	48-channel
Seismic Source	10 lb Sledge hammer	10 lb Sledge hammer
Receivers	40 Hz	40 Hz
Receiver Array	Random	Linear
Array Dimension	100 m (Square)	24 m
Receiver Spacing	Random	0.5 m
Source Offset	10 m around the grid	5 m along the line
Sampling Interval	0.5 ms	0.5 ms
Recording Time	1000 ms	1000 ms
Record numbers	1000-1012	1017-1024 (N-S) 1025-1032 (E-W)

5.4 MASW DATA ACQUIRED FROM LINEAR RECEIVER ARRAYS

The acquisition of the "active" Rayleigh wave (surface wave) data was relatively straightforward. Essentially, forty eight low-frequency (40 Hz) vertical geophones were placed at 0.5 m spacing along a 24 m spread. Seismic energy was generated at an offset (distance to nearest geophone) of 5 m using a 10 lb sledge hammer and a metal impact plate. The generated Rayleigh wave data was recorded at eight shot point locations along the line. At each "station" location, Rayleigh wave data was generated and recorded. We collected linear data in both East-West and North-South directions for accuracy.

The acquired Rayleigh wave data were processed using SURFSEIS (**Figure 19**). Each set of Rayleigh wave data (48 channel data set for each impact station location) was transformed from the time domain into the frequency domain using Fast Fourier Transform (FFT) techniques. These data sets were used to generate site-specific dispersion curve for each station location.

5.5 COMPARISON OF THE DISPERSION RESULTS

The comparison of dispersion curves from linear and random measurements are shown in **Figure 20**. The two methods show a fair extent of agreement in the frequency and phase velocity ranges up to (approximately) 50 Hz and 950 m/s, respectively. The agreement appears to be best relatively at frequencies of 25-50 Hz, and at frequencies between 13-25 Hz random-array curve deviates due to over-estimated phase velocities, which is a typical phenomenon caused by dominating energy from higher modes (Park et al., 1999). This comparison indicates a strong potential that reliable dispersion curves can be obtained using random geophone arrays.

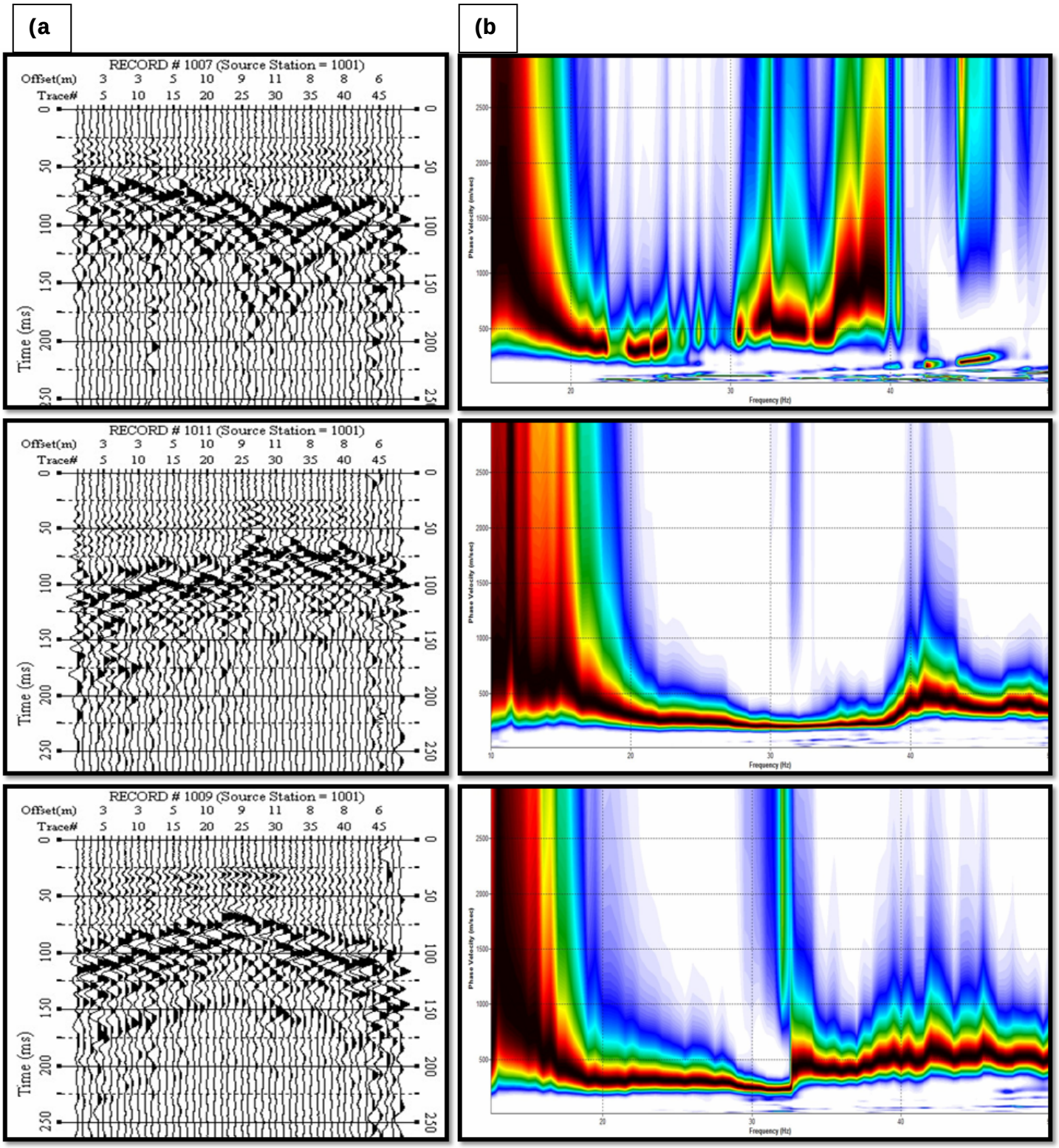


Figure 18**.** (a) Selected data (shot gathers) acquired from a field test site in the University of Tennessee agricultural center, Knoxville, Tennessee, with 48-channel system and (b) their corresponding dispersion images.

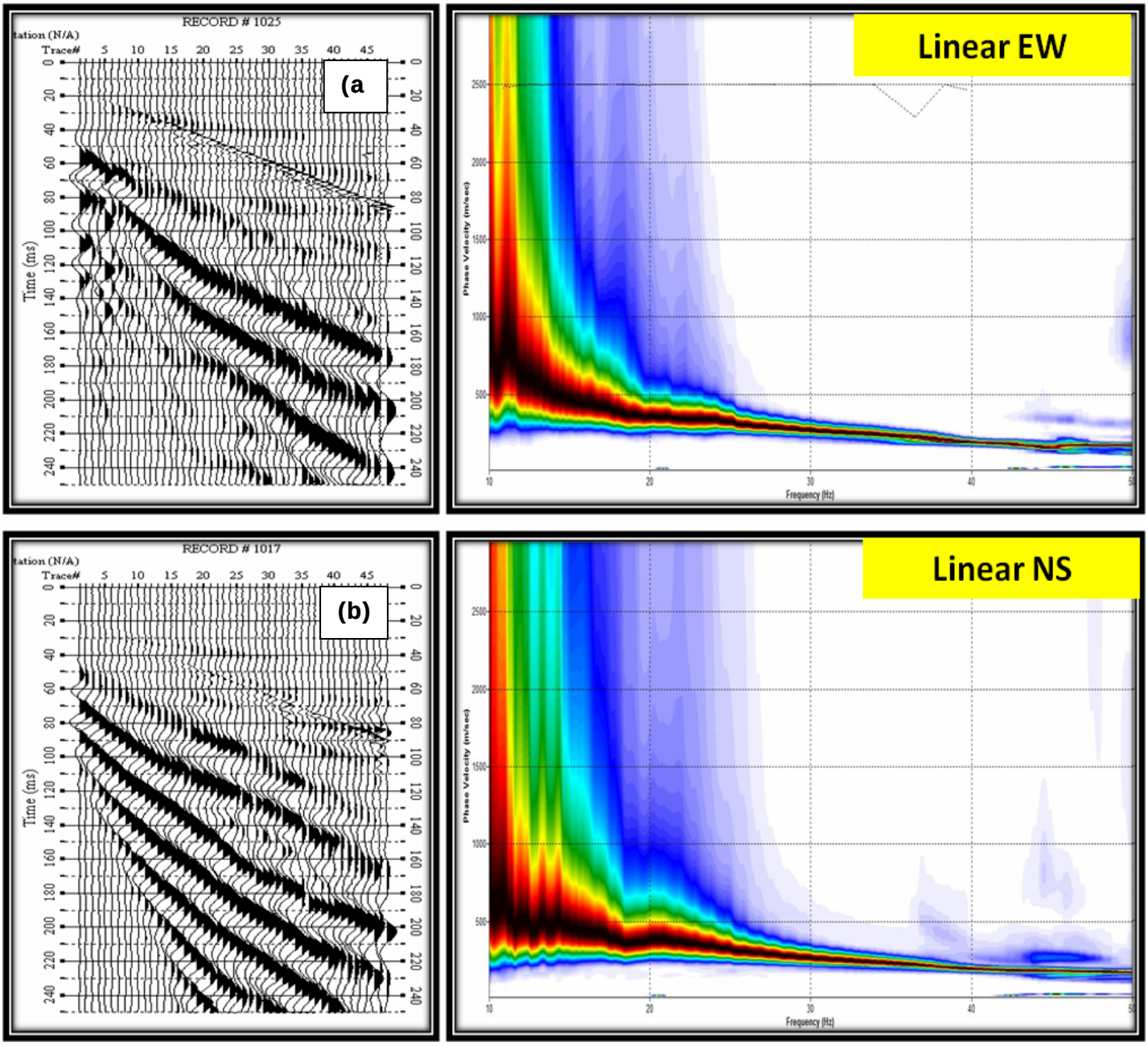


Figure 19**.** (a) Selected data (shot gathers) acquired from the same field site as above using linear receiver array configuration in East-West direction. The initial data was collected for 1000 ms but only the first 250 ms exhibits dominant surface waves. (b) Selected data (shot gathers) acquired from the same field site as above using linear receiver array configuration in North-South direction. The initial data was collected for 1000 ms but only the first 250 ms exhibits dominant surface waves.

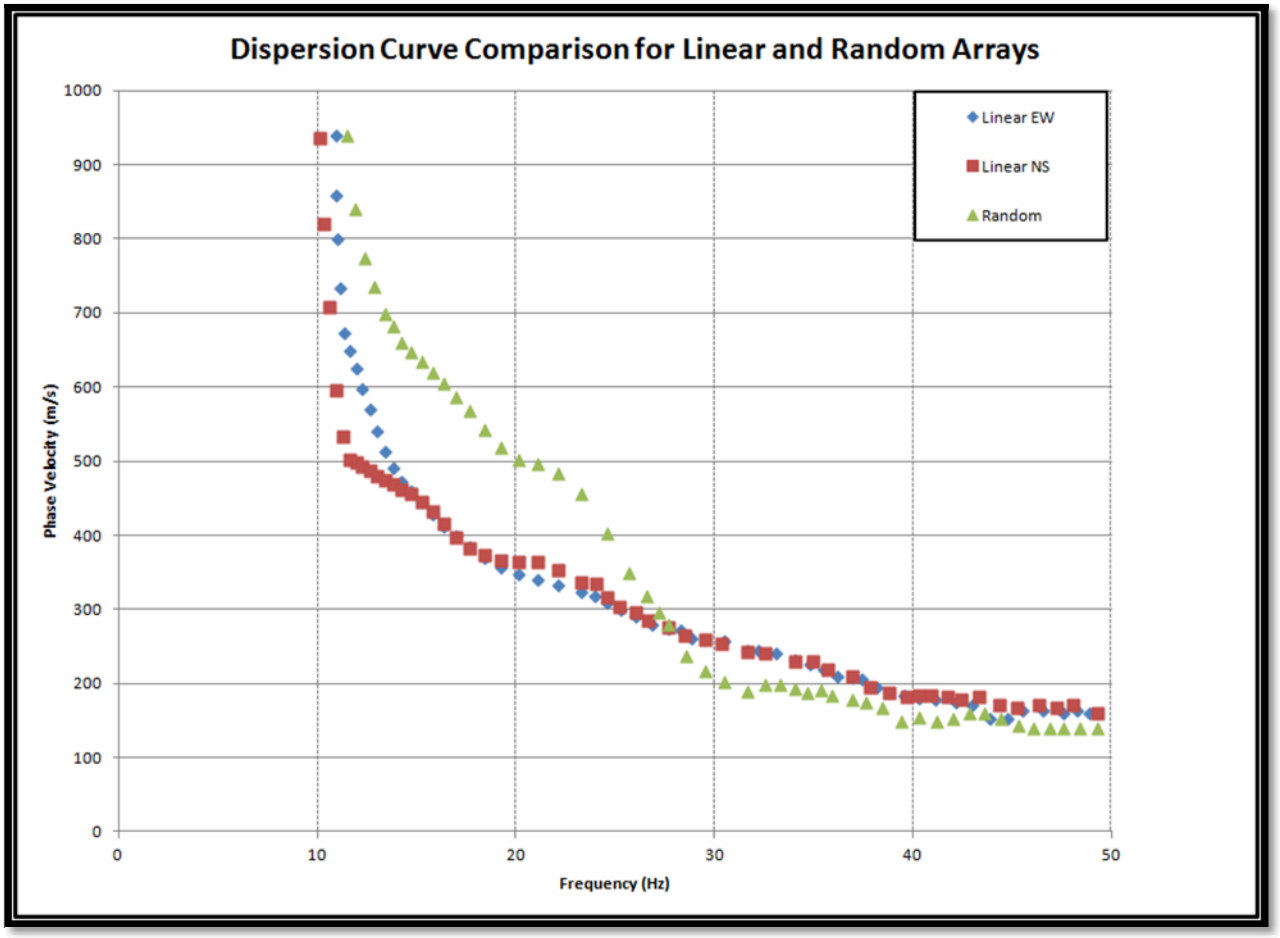


Figure 20. Comparison of dispersion relation from linear and random receiver array measurements. The x-axis represents the frequency (Hz) ranging from 0-50 Hz and the y-axis represents the phase velocity (m/s) ranging from 0-1000 m/s.

5.6 STATISTICAL ANALYSIS

Geostatistical tools were used to further analyze the random data obtained from various shot point locations. The main objective was to obtain 2D/3D models of subsurface features using the spatial analysis technique. In statistics, spatial analysis includes any of the formal techniques which studies entities using their topological, geometric or geographic properties. In this technique three (or four) variables are analyzed together, two (or three) of which are spatial coordinates: grid references or latitude/longitude, with or without altitude or depth. The other variable is a geological measurement of interest, and is regarded as varying continuously over

the area. The data may be imagined as points in three dimensions, and analysis often has the objective of constructing a smooth surface to describe spatial variation (Cadigan, 1962). The usual requirement in analyses of spatial data is to use values of a measured variable, which is symbolized by z, taken from discrete sample locations called control points, to produce a model or estimate of the values of the variable over the whole area. We may investigate statistical trends in the data by trend surface analysis or may merely estimate grid values.

The 1-D shear wave profiles resulted from dispersion images and the interpolated average shear wave velocities were used as geologic measurement of interest along with the x and y coordinates for each shot point location with respect to each geophone. All the parameters were exported to SAS software (code attached in Appendix A) to obtain variograms for various shot points and then used the statistical values (sill, range and nugget) from variograms to model the 2-D/3-D subsurface using point kriging method. The Gaussian model was used to fit the variogram which in general is a stochastic process whose realizations consist of random values associated with every point in a range of times (or of space) such that each such random variable has a normal distribution. Some of the results pertaining to shot point 4 are shown in **Figure 21** as an example. Also the various statistical parameters that are used for interpolation are shown in **Table 5**.

Table 5: Statistical parameters used in the Kriging interpolation

Shot point	Nugget		Sill (C0)		Range (a0)		adjusted R^2
	estimate	std. error	estimate	std.error	estimate	std.error	
1	229.7	60.9	1065.7	83.8	5.2	0.6	0.98
2	8.1	2.2	99.5	75.9	14.2	7.1	0.98
3	98.6	21.7	810	37	5.6	0.4	0.98
4	1.4	0.6	9.3	1.1	5.7	1	0.97
5	39.4	16.3	113.1	25.5	5.8	2	0.89
6	183.3	174.7	3387.9	422.6	7	1.1	0.97
7	1.4	0.6	9.3	1.1	5.7	1	0.98
8	9.8	3.5	105	13.3	7.3	1	0.99
9	88.5	32.8	822.7	111.9	7.5	1.2	0.99
10	10.8	4.1	58.3	6.8	5.6	1	0.97
11	10.8	4.1	58.3	6.8	5.6	1	0.97
12	2575	774.3	25042	3429.6	7.6	1.1	0.99
13	5827	1720	46774.2	25582.6	10.1	4.2	0.97

The process was followed to obtain variograms for all 13 shot points. Kriging interpolation method is used to generate 2-D models for each shot point. Kriging is a Geostatistical gridding method that produces visually appealing maps from irregularly spaced data. The variogram models are used as input to custom-fit to a data set using Kriging interpolation technique. There are various types of Kriging like Point Kriging, Block Kriging, and universal Kriging depending upon the stochastic properties of the random field. For this study we used the point Kriging type also known as the simple Kriging where it assumes the expectation of the random field to be known, and relies on a covariance function. That is, it estimates the value of a point from a set of nearby sample values using Kriging interpolation. The resulting 2-D models for a few selected shot points are shown in **Figure 22**. It can be observed that there is a significant amount of

spatial variations within the shot points which can be observed from the magnitude of contours with velocity range of 340-450 m/s. These changes in the data could be due to any azimuthal variations or due to any acquisition/processing artifacts. It can also be observed from statistical results that in each shot point model the velocities are higher at the lower left hand corner of the surface grid and lower as we go towards the upper right hand corner.

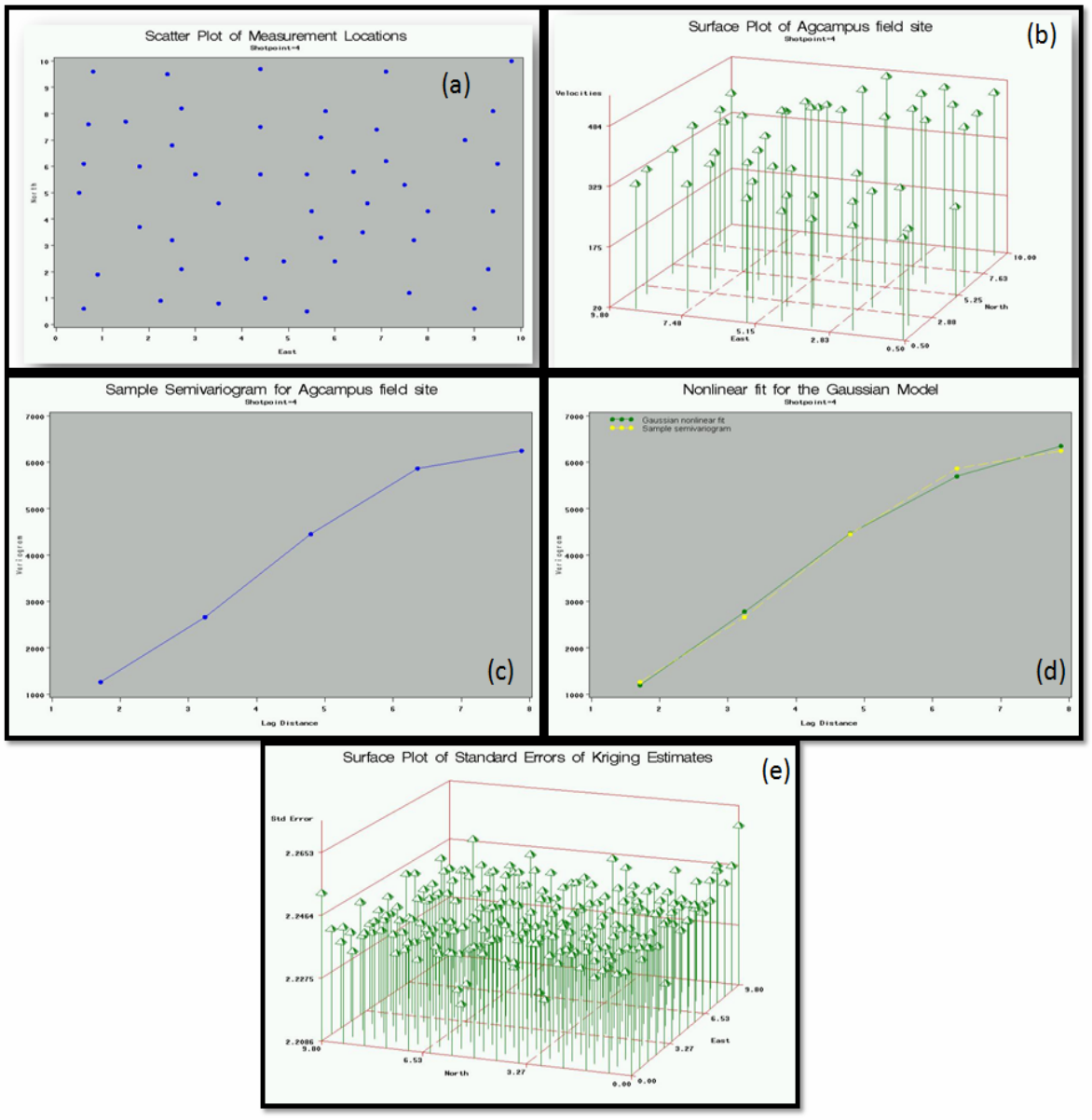


Figure 21. (a) Figure showing the locations of receivers with x and y coordinates. (b) Surface plot generated from SAS program. (c) Semivariogram calculated using the velocity values as a

geologic measurement obtained from various shot points. The statistical parameters like sill, range and nugget are also calculated. (d) Gaussian model is used to fit the variogram. (e) Final surface plot as obtained from the point Kriging interpolation method.

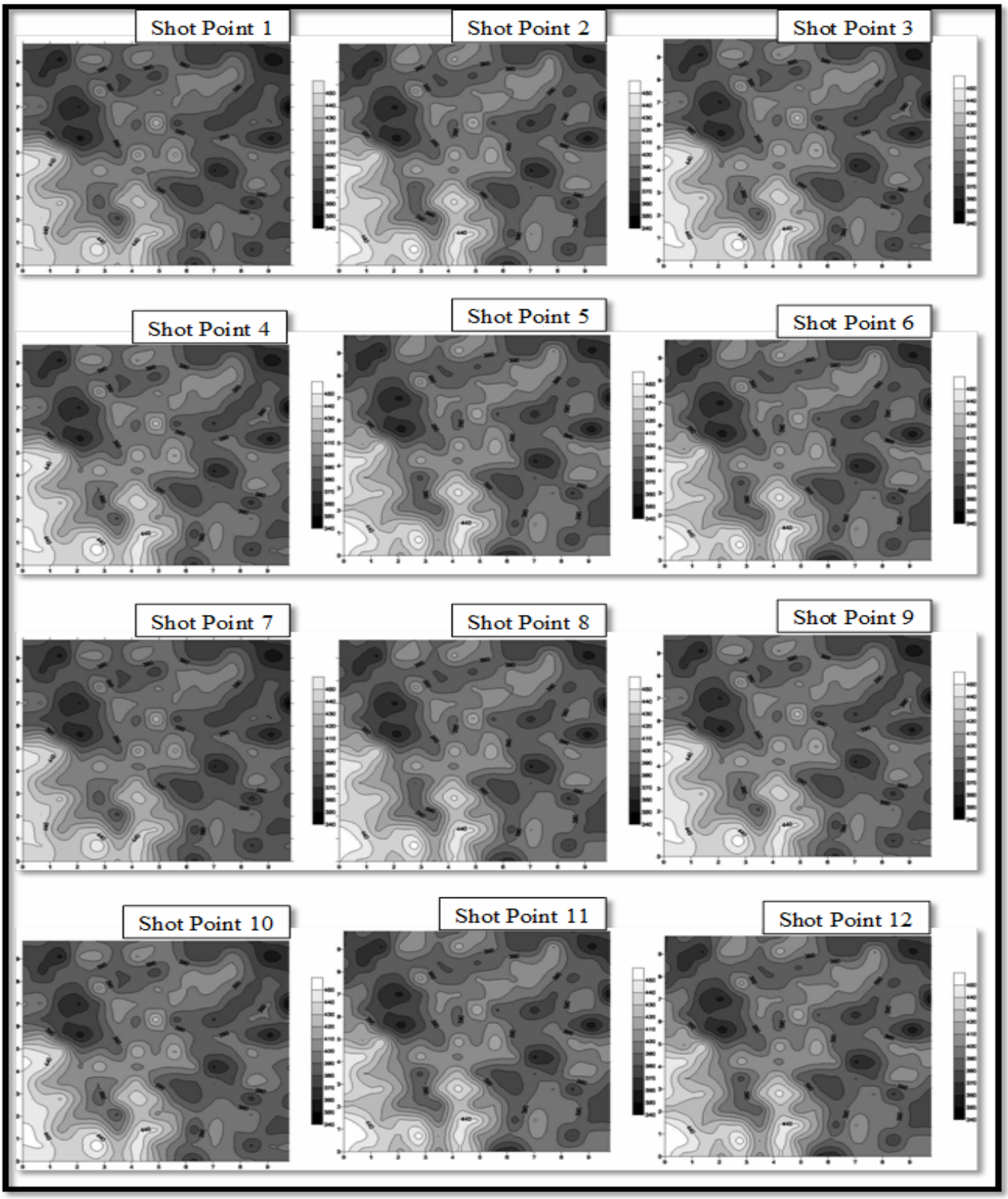


Figure 22. 2-D models obtained for each shot point location using the spatial data. The x-and y axis represents the E-W and N-S directions respectively.

5.7 DISCUSSIONS AND CONCLUSIONS

This study has introduced a new configuration of randomly-distributed receivers for estimating the S-wave velocity profile of subsurface soils. Our results thus far indicate that the random array MASW data can be used to generate reasonable dispersion curves and thus, the 1-D shear wave profiles. The dispersion results indicate that the random array data correlates fairly well with that of the conventional linear-array data. Some variations pertaining to the dispersion data could be due to azimuthal variations in the subsurface materials that may have resulted in slightly different dispersion characteristics including different amount of higher modes energy. Also the variability in the range of velocity values within the grid could be due to various reasons. There are various factors discussed in the literature that could affect the velocity values from the *in situ* measurements. Out of all, Lithology is probably the most obvious factor affecting velocity (Sheriff and Geldart, 1983). The most impressive aspect from this data is the ranges of values. Usually, higher velocity values for sedimentary rocks indicate carbonates and low velocity values indicate sands or shale whereas intermediate values indicate both. Velocity measurements are sometimes used to discriminate between sandstones and shales in area of clastic deposition. It can be inferred from the regression analysis and other statistical results that the variations in the velocity values could be due to variation in lithology (which can be the case as predicted from previous studies), and in particular due to presence of various sand and silt layers in the survey area. This assumption strongly agrees with the geology of the area too. It has also been observed from previous studies (Hilterman, 1990) that variation within the shale or sand properties like grain size and cementation can also affect the velocity values. Also, the Poisson's ratio (one of the most important seismic property of soils) decreases with increase in velocity for both sands and shales, clean sands with appreciably low Poisson value than shales.

Density, porosity and depth of burial are some of the other factors which could affect *in situ* velocity values of the subsurface (Watkins et.al., 1972).

In addition, different effects of computational artifacts from each type of array may also have contributed to the variation to a certain degree. Another possibility for the difference in the dispersion curves might be the dimensions of the receiver array, the linear array being 24 m long and random array being only 10 by 10 m, as we know from the theory that for wavelengths of surface waves longer than the array dimensions becomes less accurate in dispersion analysis. Study pertaining to further compare this newly developed technique with other conventional receiver arrays like circular and cross will be performed in near future by using both field and synthetic experiments. The data thus collected will also be compared with the borehole data for ground truth. Such comparison will be useful to further study about the computational artifacts and then ultimately about the effectiveness of the random array over the conventional arrays.

CHAPTER-6

Comparison of Seismic Surface Wave Dispersion Results Obtained from Conventional versus Random Receiver Arrays

Note: This Chapter is written specifically to be submitted directly as a manuscript. Therefore, there is some repeated material and overlap with previous and subsequent chapters.

Yeluru, P.M., Baker, G.S., and Park, C., in prep.

ABSTRACT

Understanding the physical and engineering properties (e.g., Poisson's ratio) within the upper 30 m of the lunar subsurface is critical for lunar exploration and deployment of large structures, particularly as landing of large spacecraft and mining on the surface becomes possible. Advances in both active and passive multi-channel seismic acquisition have greatly improved one's ability to determine engineering properties of the shallow subsurface, especially when using the multi-channel analysis of surface waves (MASW) technique. Using randomly distributed geophones (likely deployed from a mortar-type device) instead of a conventional linear array is necessary for lunar exploration due to the logistical constraints in arranging a linear or circular array robotically. Results indicate that robust dispersion curves (and thus subsurface models of engineering properties) are obtained from the random array geometries. The goal of this study is to compare this newly developed technique with that of the conventional methods in order to evaluate for its accuracy. Multi-channel data is acquired using conventional arrays (e.g., linear, circular and cross-arrays) at the same location where random data was collected. The dispersion datasets, obtained using various conventional arrays, were consistent with data sets of the newly developed array. All array methods are closely evaluated for the frequency, phase velocity, and, shear wave velocity ranges; they all correlate well with one another. Random geometry is also evaluated for potential improvements in the resolution of the dispersion image and as a more accurate method for assessing azimuthal variations in the subsurface geology.

6.1 INTRODUCTION

Geophysical technique of MASW is increasingly being applied to geotechnical engineering for the measurements of dynamic properties like Poisson's ratio distribution (Ivanov et al., 2000a), seismic characterization of pavements (Park et.al., 2001a; Ryden et al., 2001), and site characterizing studies (Penumadu et.al., 2005). This technique is particularly used in geotechnical engineering for the measurements of shear wave velocity, identification of material properties, their boundaries and special variations of ground etc. Being a non-invasive and less time consuming, the MASW method (Park et.al., 1999; Xia et.al., 1999) is used to evaluate material layer thickness, their shear wave velocity (1D and 2D), Poisson's ratio and density. The Multi-channel Analysis of Surface wave method (Park et.al., 1999) uses a multi-channel array, which makes it possible to distinguish the fundamental-mode from higher modes and body waves. Depending on the source used to generate surface waves, there are two types of MASW surveys: active method that utilizes a proper impact source like a sledge hammer and passive method, on the other hand, utilizes ambient noise such as traffic or tidal motion. The active method is considered to be the conventional mode of survey, collecting data in a roll-along mode using an active seismic source and a linear receiver array. The passive remote method utilizes ambient cultural noise such as traffic, thunder, tidal motion etc. and employs a two-dimensional receiver array such as a cross, circular, random etc. to record passive surface waves. Initial studies indicate that robust dispersion curves (and thus subsurface models of engineering properties) are obtained from the random array geometries (Yeluru et al 2008). Using randomly distributed geophones (likely deployed from a mortar-type device) instead of a conventional linear array is necessary for lunar exploration due to the logistical constraints in arranging a linear or circular array robotically. It has been observed from preliminary experiments that

reliable dispersion images, and 1-D shear wave velocity profiles, can be obtained by using random geophone arrangement.

However, a detailed study comparing each different type of array and its effect on dispersion analysis has not been reported yet. Therefore, this study is particularly focused on comparing different types of conventional arrays with the random array in order to evaluate for its accuracy.

6.2 SITE DESCRIPTION-GEOLOGIC SETTING

The field Hydrology Teaching and Research Site is located at the University of Tennessee (UT) Plant Science Farm, alongside Highway approximately 2 miles south of the UT campus (**Figure 23**). It is located between the highway and the Tennessee River. Soil conditions across the site vary from residual soils developed directly on sedimentary bedrock near the highway, to loamy soils developed on a series of alluvial terraces at different elevations above the river. Both visual and particle size analyses of sediment sampled from two borings support this fining up progression. Analysis of material from existing core samples from wells drilled at this location further confirms this progression. The bedrock is very fine-grained Ordovician calcareous Ottossee Shale, underlying the sediment at the site and is composed of claystone, shale and sandstone depositional sequences with some limestone interbeds. The upper portion of the bedrock contains numerous weathered and stained fractures and can also be used as a low yield aquifer. Also the underlying irregular and heterogeneous bedrock surface was reworked under high energy conditions as coarse sands and gravel were laid down. The contact between the Ottosee Shale and the alluvium was found to be weathered bedrock beneath unconsolidated

coarse gravel and sand material. Clays from the hydrogeology teaching and research site sampled from core samples were calcareous with weathered shale fragments. The variable types of clay can be attributed to the folded and interbedded shale, sandstone, and limestone bedrock underlying the field site (Benfield et al., 2003).

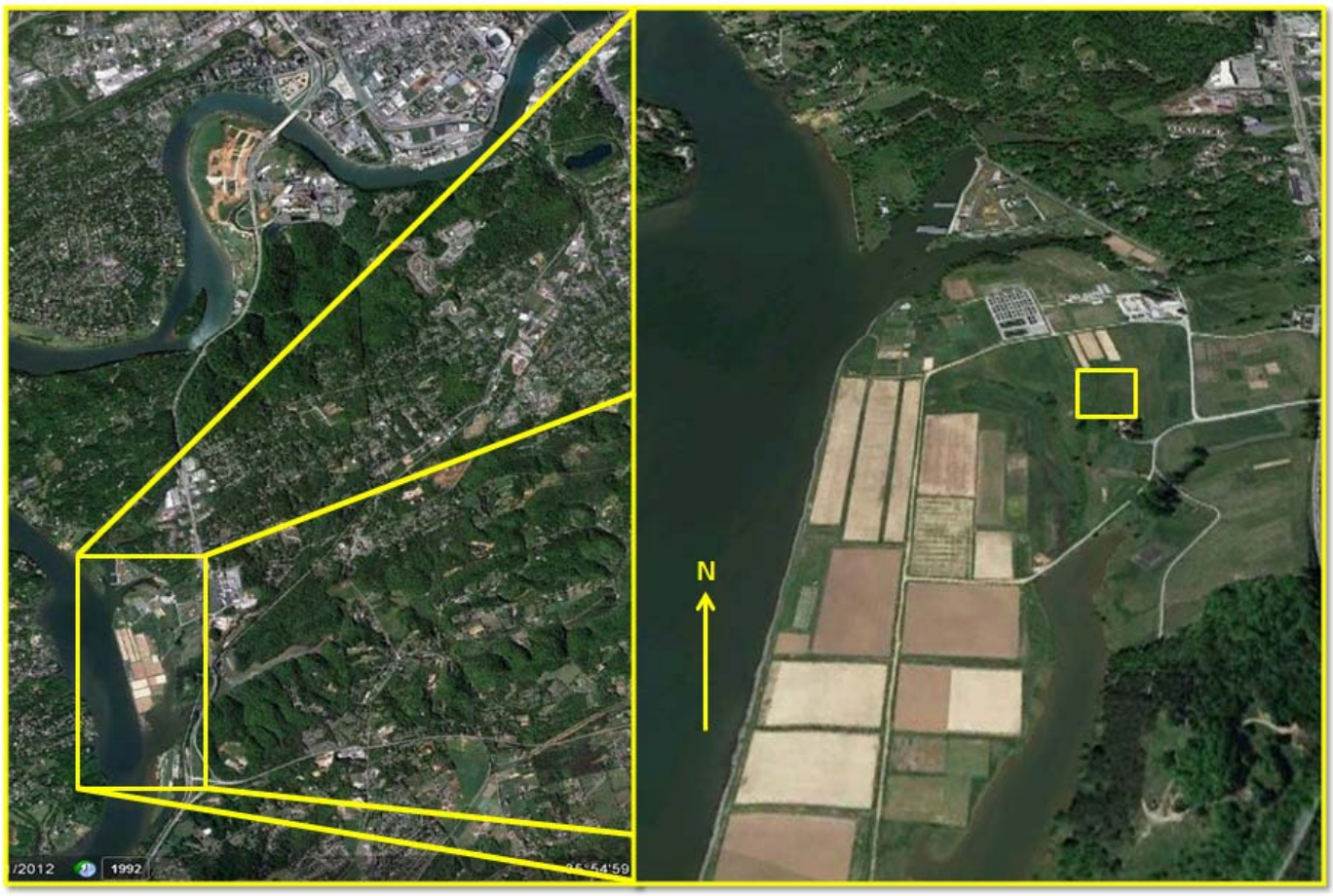


Figure 23. Location of the University of Tennessee Agricultural Extension Center, Knoxville, TN. The yellow square located in the zoomed in map shows the location of the study area (Google Earth).

6.3 DATA ACQUISITION AND ANALYSIS

The MASW data was collected for linear, circular, cross and random arrays at the University of Tennessee agricultural field test site in eastern Tennessee USA, using 2, 24-channel Geometrics Geode seismograph with 40 Hz spike coupled geophones with spike firmly

planted on the ground. The data was collected in SEG2 format with a recording time of 1000 ms and sample interval of 0.5ms. Other parameters like the source-receiver offset distance, total length of the array line and receiver spacing were all estimated depending upon the array type. Acoustic energy was generated by using a 10-lb sledge hammer and metal plate as the seismic source and the data were acquired at 13 different shot points around the 10 m × 10 m grid. No acquisition frequency filter was applied during the recording. To increase signal-to-noise ratio, three impacts at each station were vertically stacked. The receiver array lengths varied depending on the array design but they all shared the same center point. The dimensions and other parameters used for each type of receiver array are described in **Table 6**. Also the grid setup and the locations of the shot points are all portrayed in **Figure 24**. Four different random data sets were collected (all having different X-Y coordinates) in order to determine the accuracy of the array. Typical shot gathers for each type of array as acquired in the field are shown in **Figure 25**. Also schematic representation of various array designs as deployed within the 10 m × 10 m grid in the field are shown in **Figure 26 (a)-(b).**

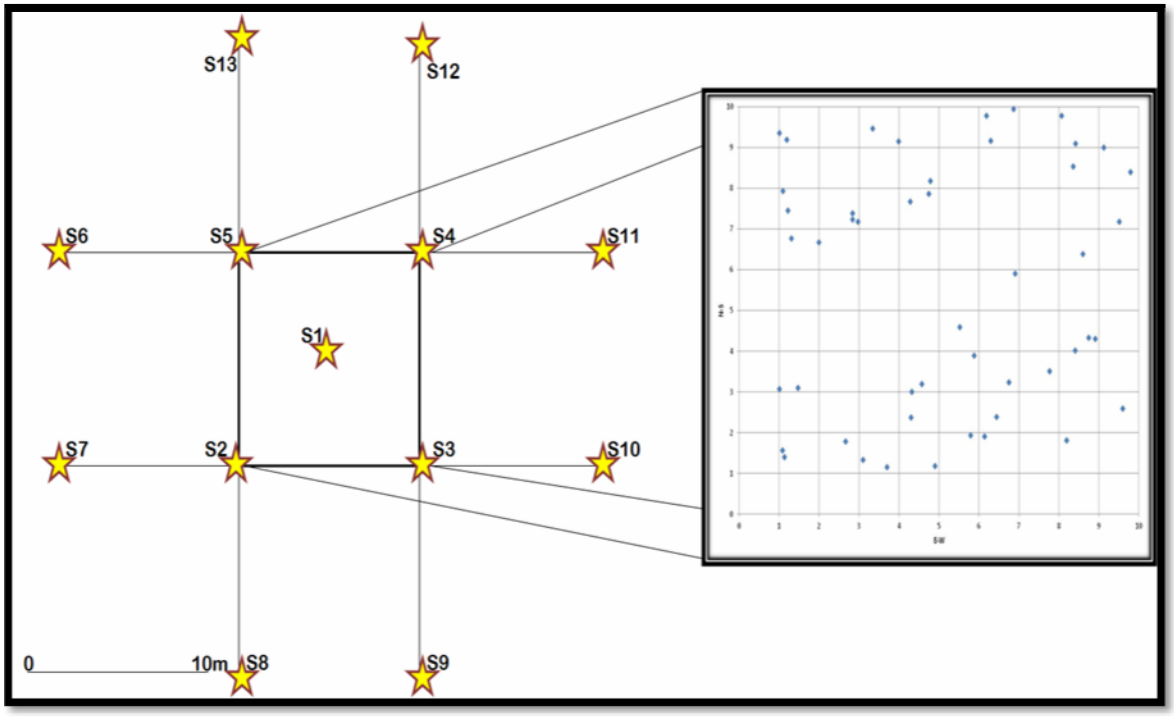


Figure 24. The figure on the left represents the shot point locations as deployed on the ground. There are total 13 shot points from which data was collected. The distance between each shot point location is 10 m. The figure on the right represents the random arrangement of geophones (small circles) inside a 10 m×10 m grid.

Table: 6. Parameters as used in the field for different receiver arrays

Survey Type	Linear EW	Linear NS	Circular	Cross	Random-1	Random-2	Random-3	Random-4
File Name	LinearNS_MASW.dat	LinearEW_MASW.dat	Circular_MASW.dat	Cross_MASW.dat	Random_MASW.dat	Random_MASW.dat	Random_MASW.dat	Random_MASW.dat
Survey purpose	1-D Vs profiling	1-D Vs profiling	1-D Vs profiling	1-D Vs profiling	1-D Vs profiling	1-D Vs profiling	1-D Vs profiling	1-D Vs profiling
Data format	SEG-2	SEG-2	SEG-2	SEG-2	SEG-2	SEG-2	SEG-2	SEG-2
Acquisition	48-channel	48-channel	48-channel	48-channel	48-channel	48-channel	48-channel	48-channel
Seismic source	Sledge hammer	Sledge hammer	Sledge hammer	Sledge hammer	Sledge hammer	Sledge hammer	Sledge hammer	Sledge hammer
Receivers	40 Hz	40 Hz	40 Hz	40 Hz	40 Hz	40 Hz	40 Hz	40 Hz
Receiver array	Linear	Linear	Circular	Cross	Random	Random	Random	Random
Array dimensions	24m	24m	10m diameter	24m	100 m (square)	100 m (square)	100 m (square)	100 m (square)
Receiver spacing	0.5 m	0.5 m	0.63 m	1 m	Random	Random	Random	Random
Source offset	5m	5m	10 m around the grid	10 m around the grid	10 m around the grid	10 m around the grid	10 m around the grid	10 m around the grid
Sampling interval	0.5 ms	0.5 ms	0.5 ms	0.5 ms	0.5 ms	0.5 ms	0.5 ms	0.5 ms
Recording time	1000 ms	1000 ms	1000 ms	1000 ms	1000 ms	1000 ms	1000 ms	1000 ms
Record numbers	1017-1024	1025-1033	1000-1012	1000-1013	1005-1017	1018-1030	1031-1045	1046-1058

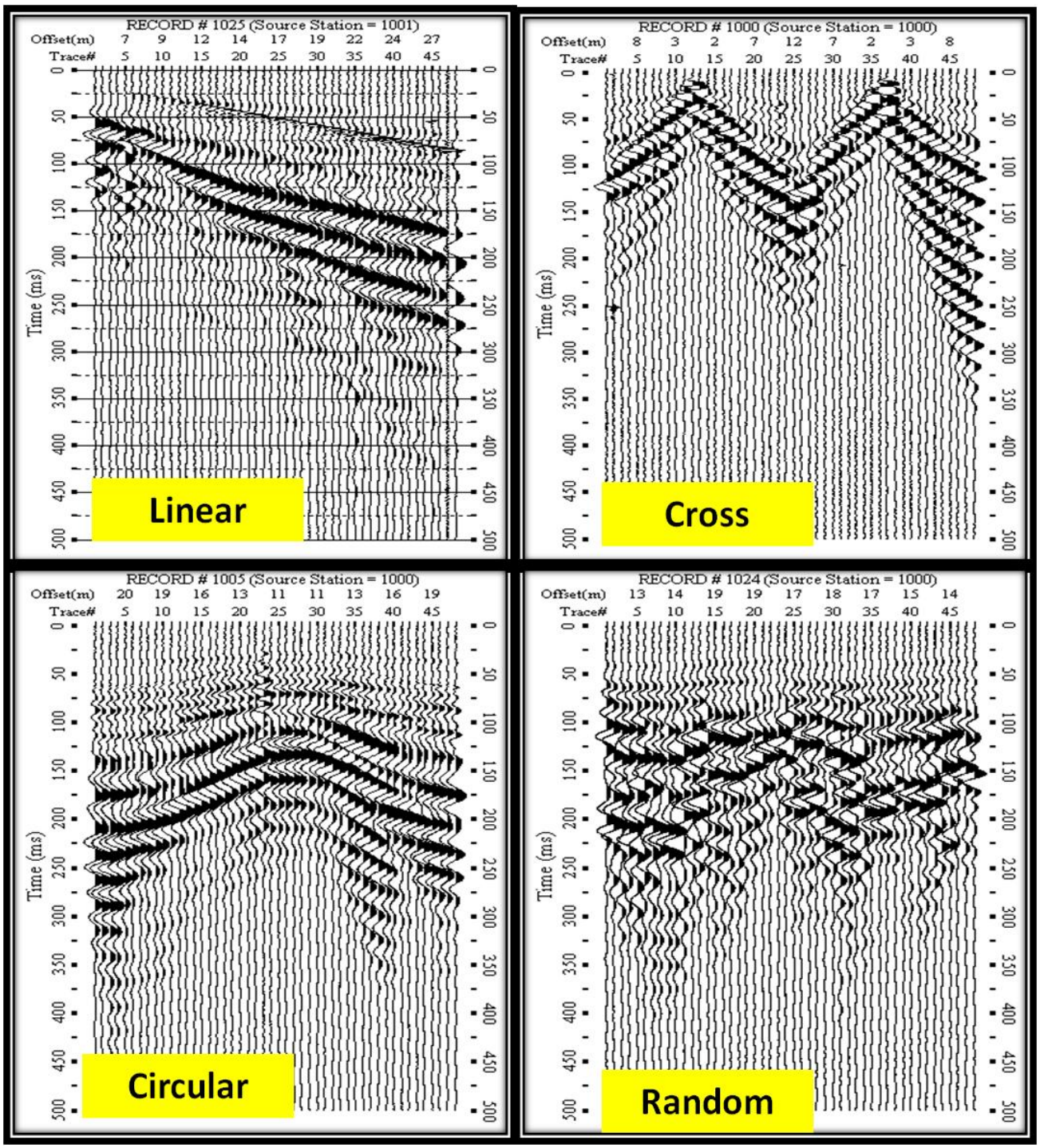


Figure 25. Shot gathers for various arrays. The x-axis represents offset (m) and trace numbers and y-axis represents time (ms). Data was collected for 1000ms but only the first 500ms is shown here.

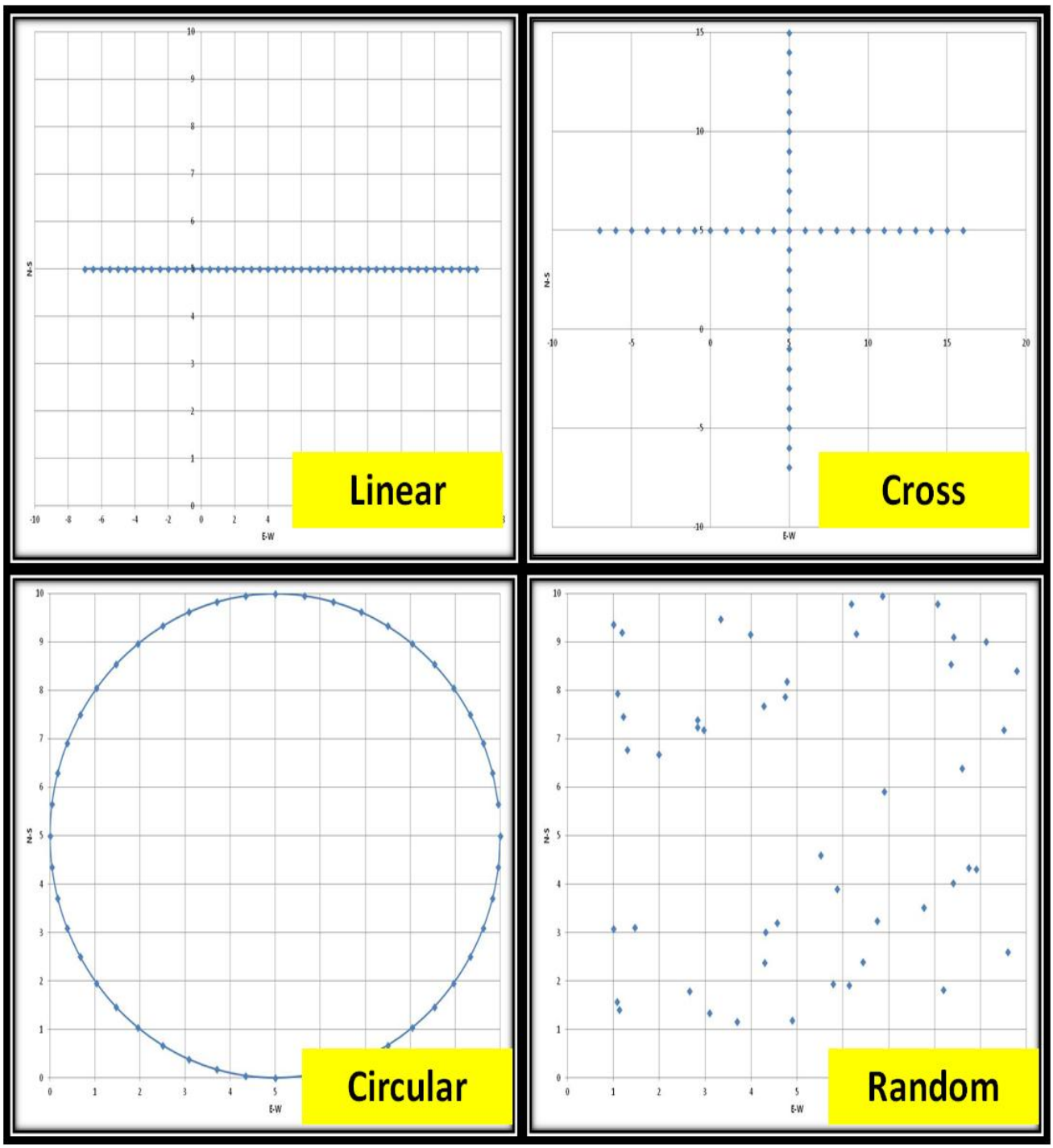


Figure 26 (a). Schematic representation of various array designs as deployed in the field. The x-axis represents E-W and y-axis represents the N-S directions.

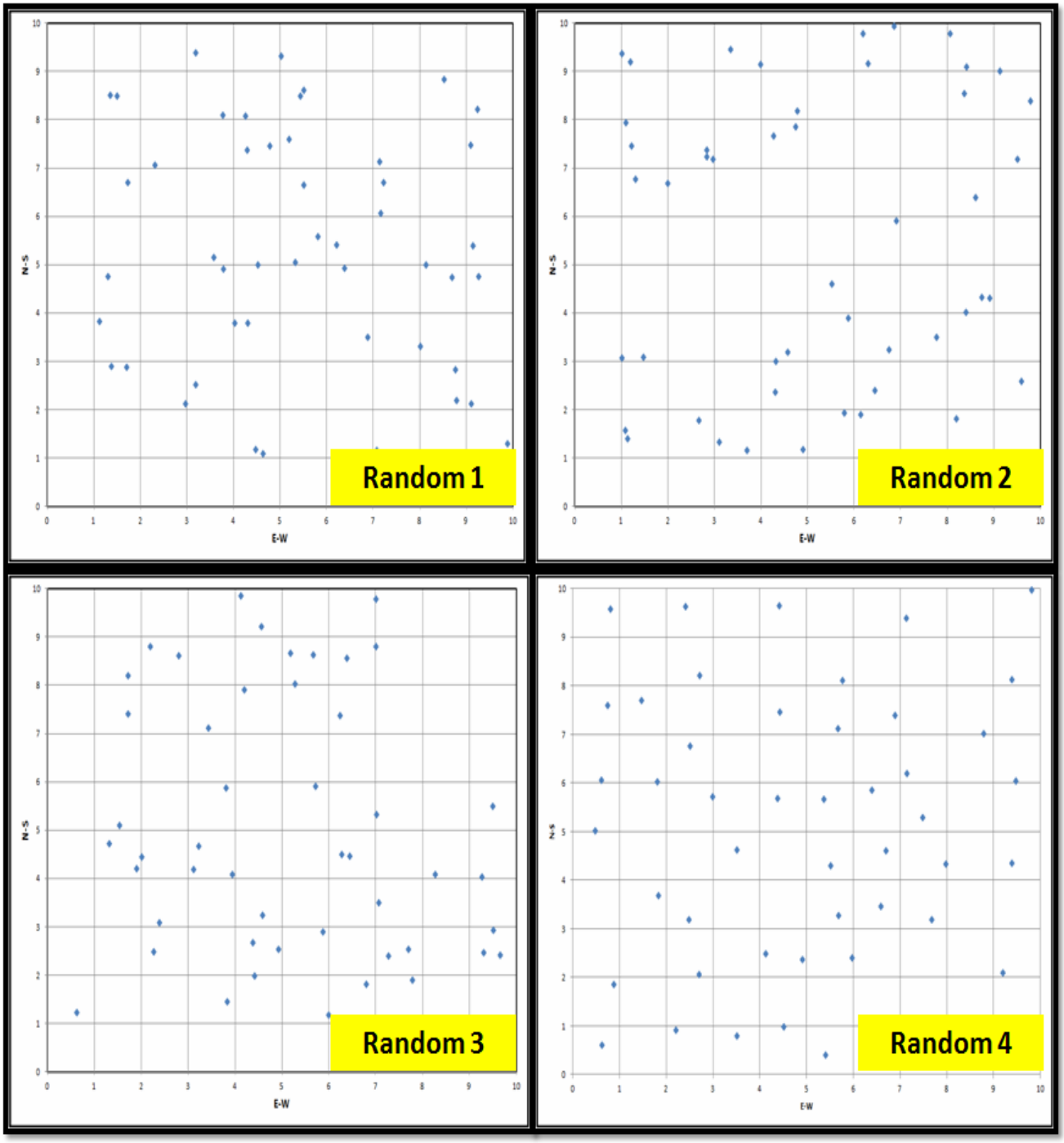


Figure 26 (b). Schematic representation of four different random arrays (different receiver spacing with different x and y coordinates) as deployed on the ground in a 10 by 10 m grid. The x-axis represents E-W and y-axis represents the N-S directions

The obtained surface wave data was processed using SURFSEIS software developed by Kansas Geologic Survey and involved the following process. First the data is converted from SEG-2 to KGS format and the field geometry was encoded into the seismic trace headers. The next step involves converting time-domain data into frequency domain. A detailed flow chart representing different steps involved in data processing is shown in **Figure 27.**

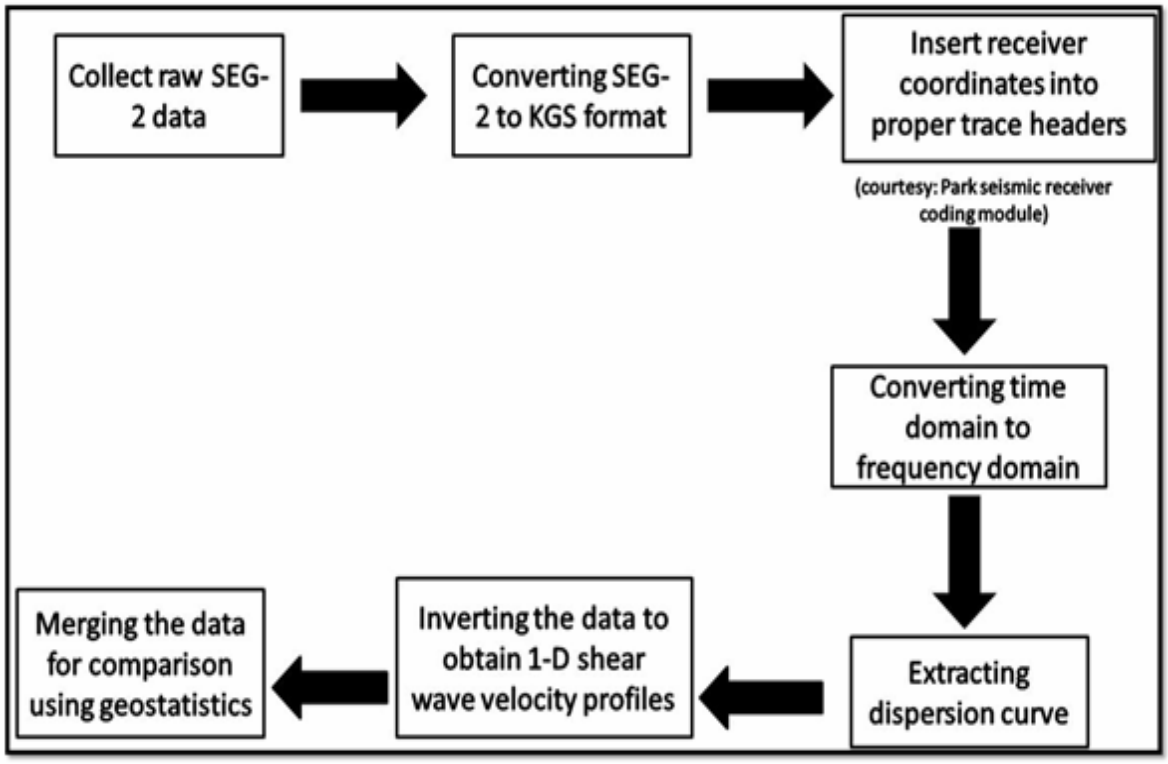


Figure 27. Schematic representation of steps involved in data processing and analysis.

Average dispersion curve is obtained combining all 13 records using frequency range 1-100 Hz and phase velocity range 10-3000 m/s. This process is repeated for all receiver array types and the dominant frequency of surface waves varied around 30-55 Hz for different arrays. A very good signal to noise ratio was obtained for all records. The dispersion images obtained for various conventional arrays and for four different random arrays are shown in **Figure 28 (a)-(b)**. It can be observed that the dispersion of the fundamental mode of surface waves is very clear

in the frequency range from 10-40 Hz for conventional arrays but the fundamental mode extends only up to 30 Hz for random array (**Figure 29**) with a steep decrease of phase velocity in the range 12-17 Hz down to minimum phase velocity of around 340 m/s. No Rayleigh wave energy is found propagating lower than 10 Hz and this part of the dispersion image appears blank for all array types. Part of the reason for this observation may be the presence of stiff basement rocks. In some of the dispersion images some higher modes of surface waves are clearly visible above 18 Hz. Once the bounds (upper and lower limits of phase velocities for the dispersion curve to be extracted) are set, the dispersion curve is extracted automatically within the given range. The total number of dispersion picks that constitutes the dispersion curve was set to 30 with equal-wavelength frequency interval used to make the frequency interval denser at low and coarser at higher frequencies. The dispersion curves extracted for various conventional and random array agree closely especially at frequencies 10-18 Hz although there are discrepancies at higher frequencies around 20-32 Hz between the conventional arrays and the random array (**Figure 31**). It can also be observed that out of the four different random arrays, the dispersion image corresponding to random 4 is crisper and the fundamental mode can be readily identified in it when compared to the other random array images. A graphical representation of the dispersion picks (**Figure 30**) for the four random arrays show that random 4 is different than random 1, 2, and 3 in a way that the fundamental mode for random 4 starts around 10 Hz and extends up to 32 Hz, which closely resembles the conventional arrays whereas random 1, 2, and 3 starts around 14 Hz and extends up to 32 Hz. This deviation might have occurred due to over estimated phase velocities, which is a typical phenomenon caused by dominating energy from higher modes (Park et al., 1999).

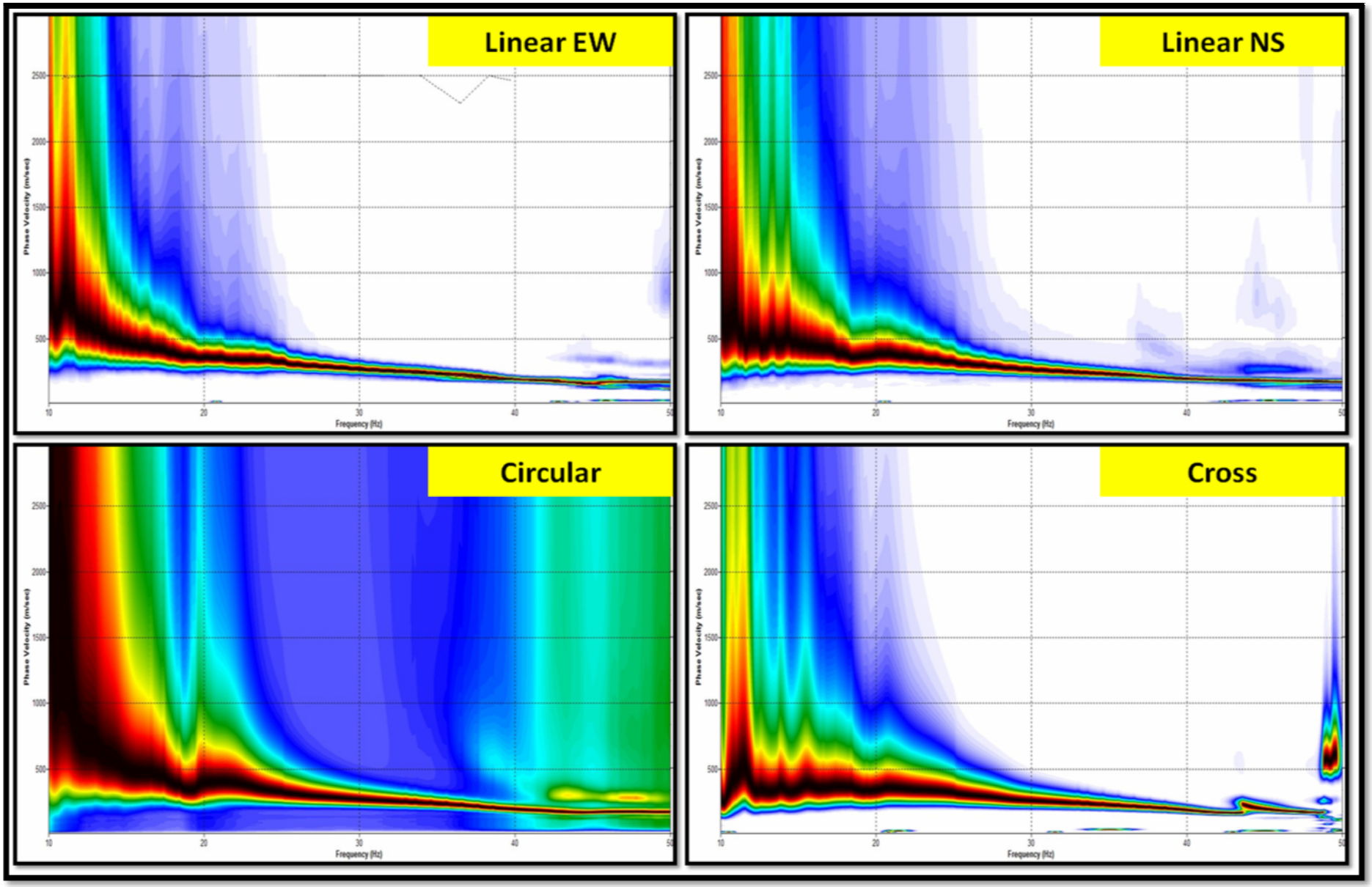


Figure 28 (a). Dispersion images for conventional Linear (EW and NS), Cross, and Circular receiver arrays. The x-axis represents Frequency (Hz and Y-axis represents Phase Velocity (m/s). Data was processed for frequencies from 1-100 Hz and phase velocities from 100-3000m/s but data l is displayed only from 10-50 Hz as surface wave dispersion curves are dominant at these frequencies.

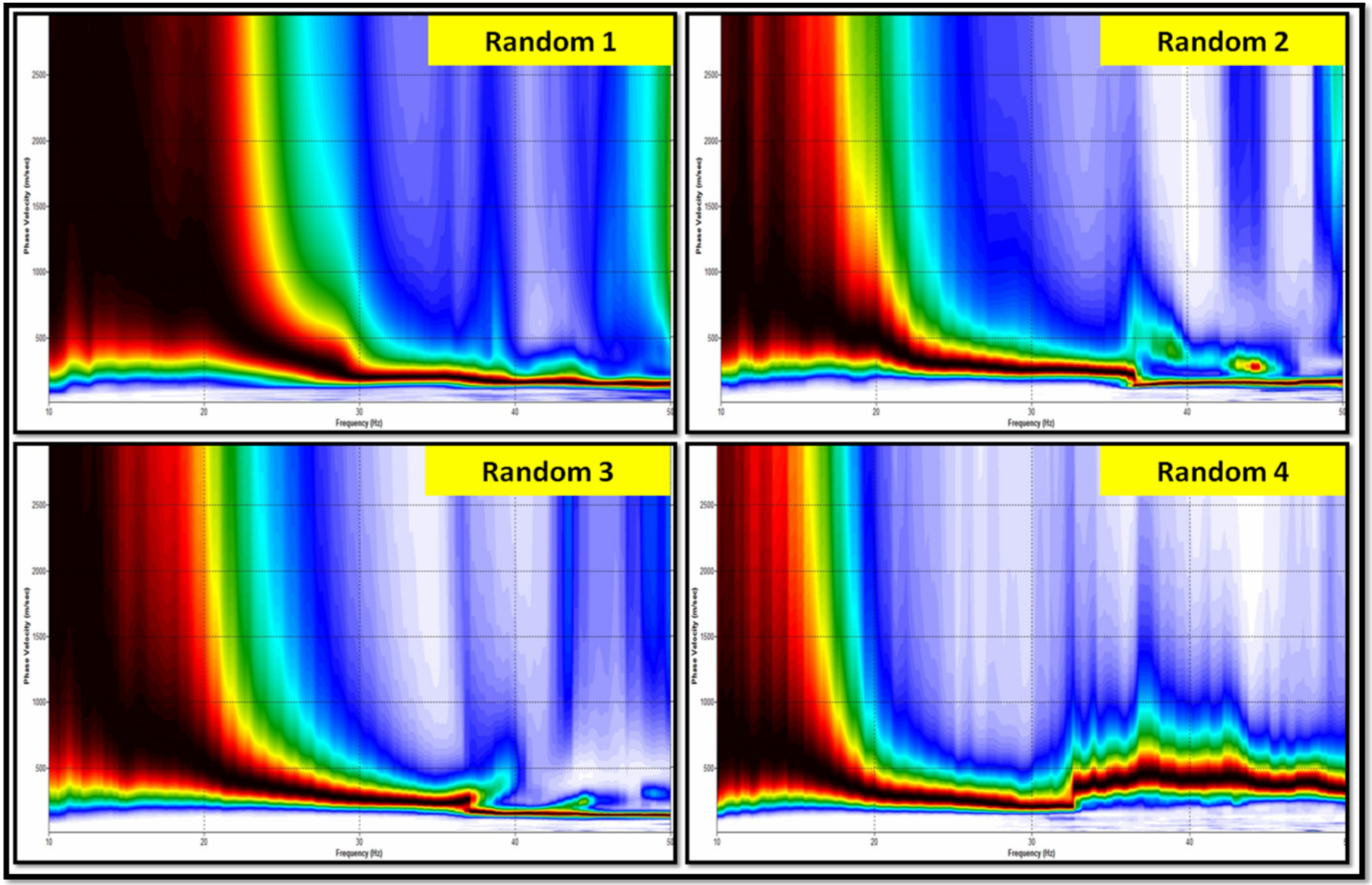


Figure 28 (b). Dispersion images for four different random receiver arrays. The x-axis represents Frequency (Hz) and Y-axis represents Phase Velocity (m/s). Data was processed for frequencies from 1-100 Hz and phase velocities from 100-3000m/s but data here is displayed only from 10-50 Hz as surface wave dispersion curves are dominant at these frequencies.

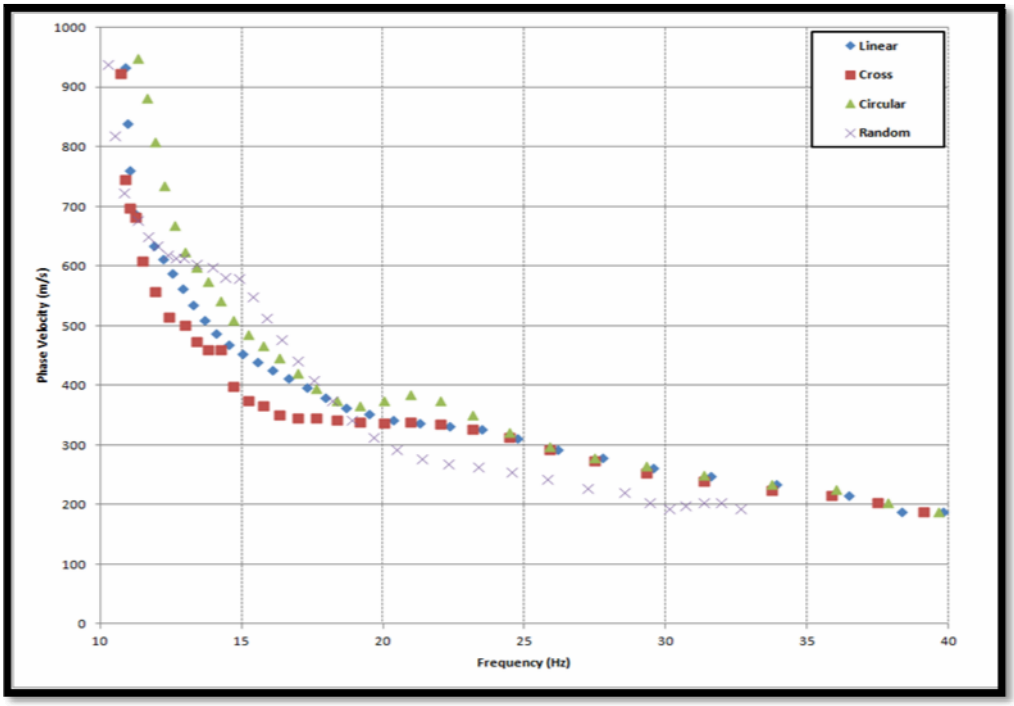


Figure 29. A graph representing dispersion curve comparison for four types of receiver arrays. The x-axis represents frequency (Hz) ranging from 10-40 Hz and y-axis represents phase-velocity (m/s) ranging from 0-1000 m/s.

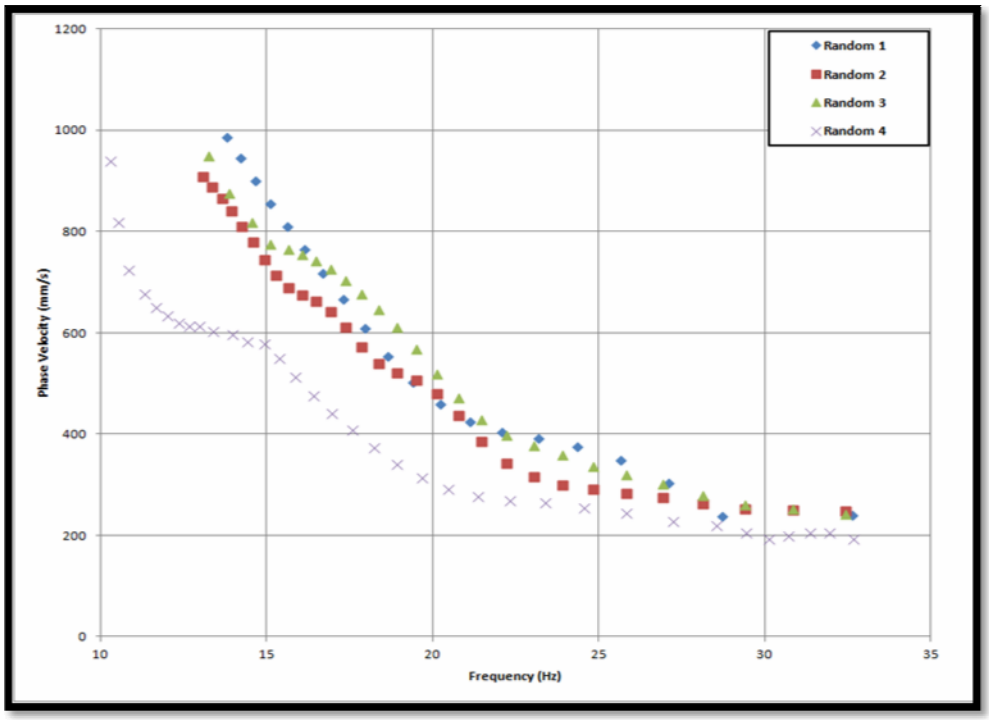


Figure 30. Comparison of dispersion curves for various random array distributions. The x-axis represents frequeny (Hz) ranging from 10-35 Hz and y-axis represents phase-velocity (m/s) from 0-1000 m/s. It is observed that random 1,2, and 3 curves show higher velocity values when compared to random 4.

One-dimensional (1D) inversion of dispersion curves was performed using a gradient based iterative solution to the weighted equation (Xia et al., 1999) using Levenberg-Marquardt method. Figures 6.10 and 6.11 represent the results of inversion. In this method, an initial earth model (where the thickness of the layers increases with depth) with ten layers is used as a base model and is applied to the real data. The maximum depth of investigation is defined by the size of the array and the lowest frequency of the dispersion curve, which in my case was around 30 m. The stopping criteria for inversion was maximum 12 iterations or RMS error in phase velocity lower than 5. The P-wave velocity was fixed to S-wave velocity using the Poisson ratio 0.4.

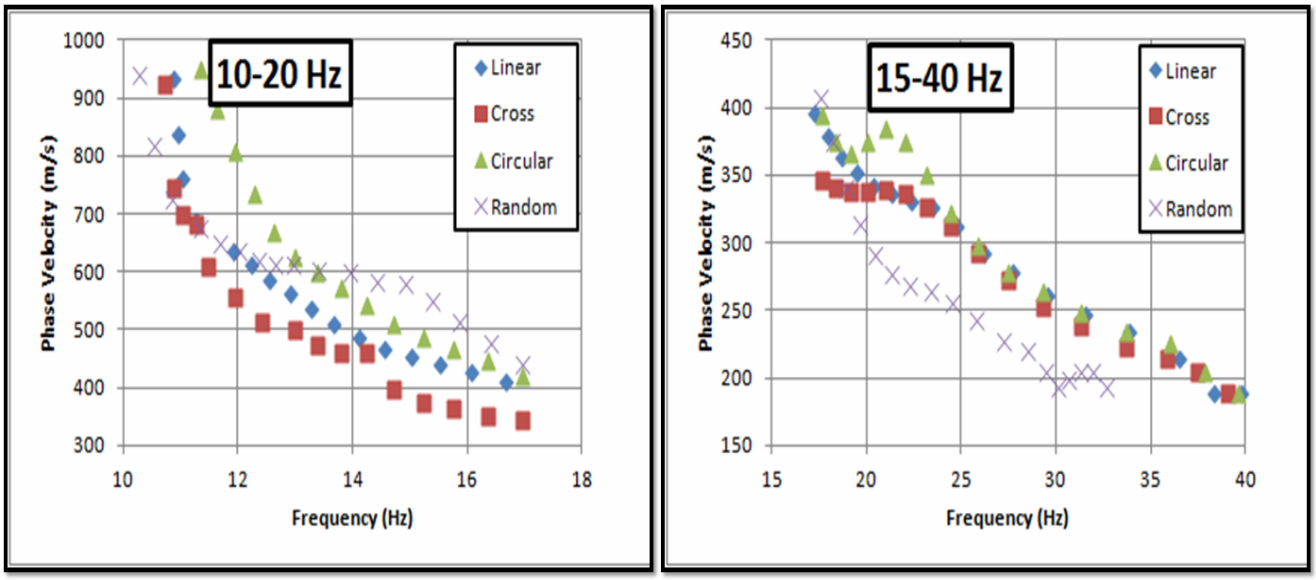


Figure 31: Schematic graphs representing dispersion picks split up into 10-20 Hz and 15-40 Hz to observe the differences within the dispersion picks for clarity. It can be observed that at lower frequencies the phase velocity values agree closely with each other and at higher frequencies (starting from 18 Hz to 32 Hz) the random deviates from the conventional arrays.

6.4 RESULTS

The 1-D shear wave velocity profiles obtained with different types of arrays are shown in **Figures 32 (a)-(b)**. The variation of Vs velocities at all depths seems to be pretty consistent for all array types. The depth to the bedrock can be clearly identified at around 12 m depth from all array types. **Figure 35 (a)** represents a soil profile obtained on the test site using cross hole and borehole data. The obtained was compared both graphically (**Figures 33 and 34**), statistically (Table 6.2) and also from the 1-D Vs profiles (**Figure 32 a-b**).

Comparison of velocity profiles up to a depth of 30 m shows the following results:

a) All the profiles start with thin layer (1-2m thick) and are characterized by MASW shear-wave velocities between 200-400 m/s on an average for all array types. This zone primarily consists of low plasticity organic silts.
b) In the depth range of 2-3 m there is a low velocity layer (130-190 m/s) which is prominent in almost all the profiles. This layer is characterized by silts that grades to silty sand. It is observed from the core samples taken from the site that the silt and sand layers are laterally extensive.
c) It can also be observed from the Vs profiles that there is a slight decrease in the velocities at 7.5-10 m depth and this might be due to the transition of silt to sand. This transition depth can also be verified from the particle size analysis that was done on the core data acquired from this site. It was used for determining the gradational sequence of the material from the site. These tests were done at several depths and the one done on the 7.5 m sample showed that the fine material begins to grade to sand and further grades to coarser sand and gravel.

d) After approximately 10 m depth (at around 12 m) the shear wave velocity values increase gradually until 30m from 375 m/s to 880 m/s in linear array, 400 m/s to 1000 m/s for cross, 500 m/s to 975 m/s for circular and from approximately 400 m/s to 900 m/s in random. This increase in velocity values may correspond to either clay or saprolite formation above bed rock. Also the highest velocity found in the inversion was around 900 m/s which is indicative for bedrock which is characterized by calcareous shale with some limestone interbeds.

Although there are variations within each array with respect to each depth, the S-velocities from dispersion of surface waves for all the depths on an average are comparable with each other and determine geologically similar results. The average shear-wave velocity in upper 30 m (Vs,30) which is a parameter widely applied in seismic microzonation, also the main parameter for ground type classification in Eurocode 8 standard (EUROCODE 8, 2003), was computed using the following expression for each array type.

$$V_{S,30} = \frac{30}{\sum_{i=1,N} \frac{h_i}{V_i}} \quad \ldots\ldots (6.1)$$

Where h_i and V_i denote the thickness (in m) and shear-wave velocity (in m/s) in the i-th formation of layer, in a total of N, existing in the top 30 meters. The following values were obtained for each array:

Array type	Vs30 (m/s)	Class
Linear	152	E
Cross	142	E
Circular	156	E
Random 4	148	E
Random 3	198	D
Random 2	182	D
Random 1	186	D

It can be inferred from the above values that the investigated site is classified as ground type E (Vs<180 m/s) from all different types of arrays which is a characteristic of soft soils except for random arrays 1, 2, and 3 which are characterized more as stiff soil and not soft soil. They show higher values as an effect of overestimated phase velocity values in the dispersion curves. Considering also the stratigraphic description of the site (**Figure 35 a**) as well as the Vs 30 values the ground type is described as: quaternary alluvial deposits exhibiting coarse gravel materials grading upward to finer texture sands and silts.

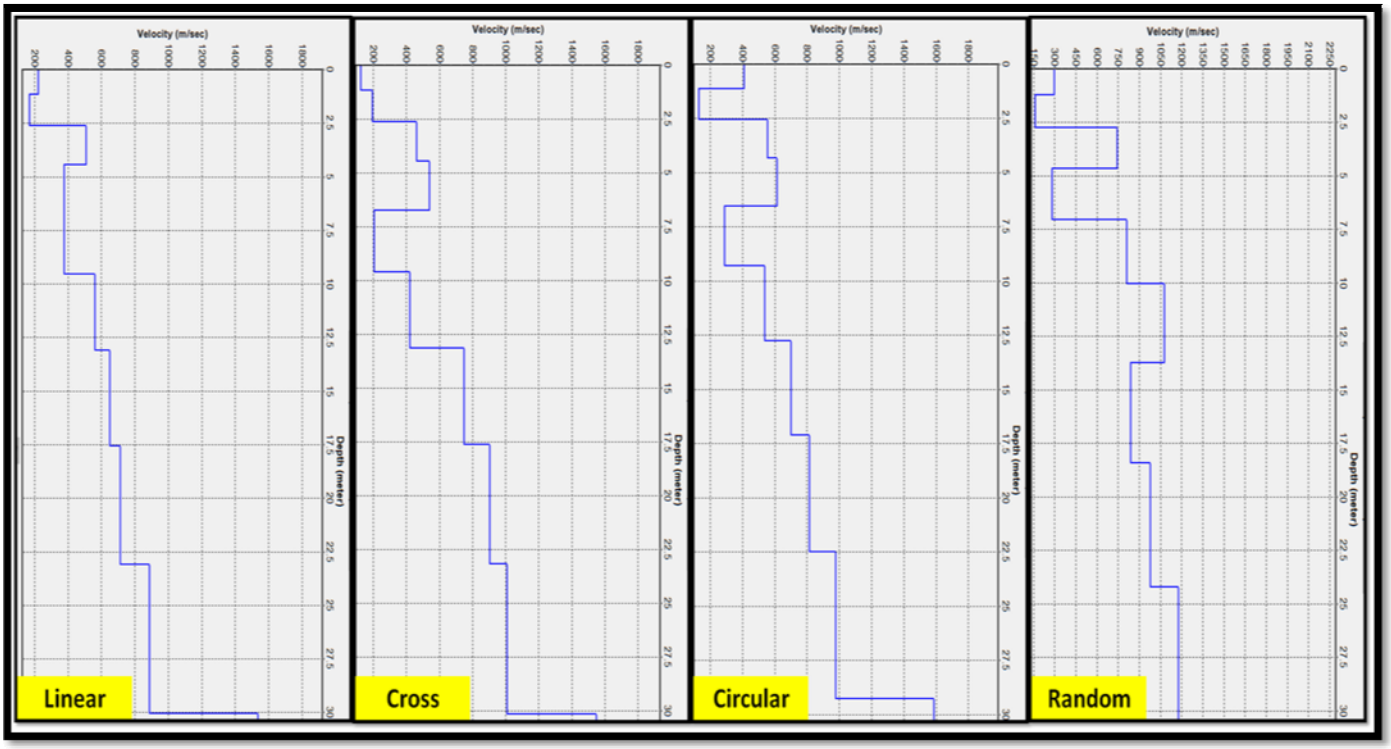


Figure 32 (a). 1-D shear wave velocity profiles for various conventional and random receiver arrays obtained by inverting the phase velocity picks from Figure 6.6 (a).

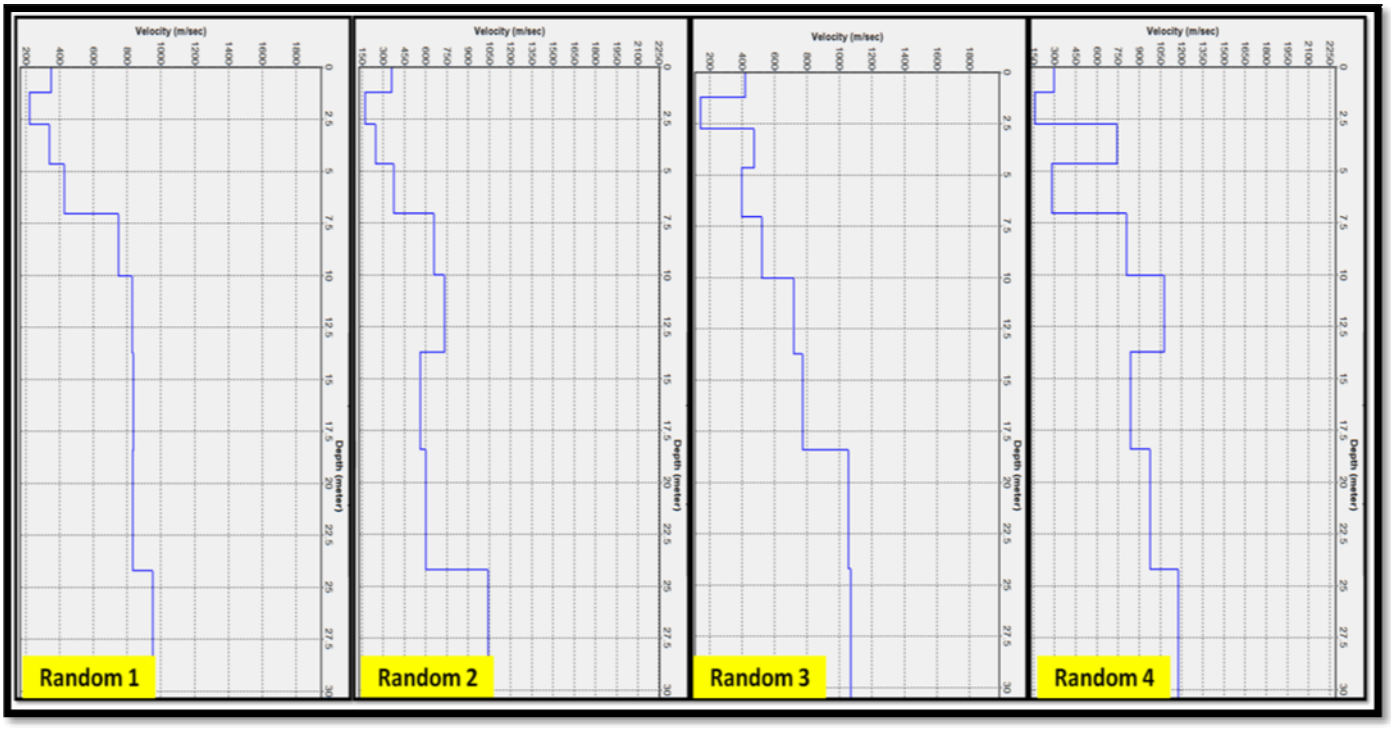


Figure 32 (b). 1-D shear wave velocity profiles for various random arrays obtained by inverting the phase velocity picks from figure 6.6 (b).

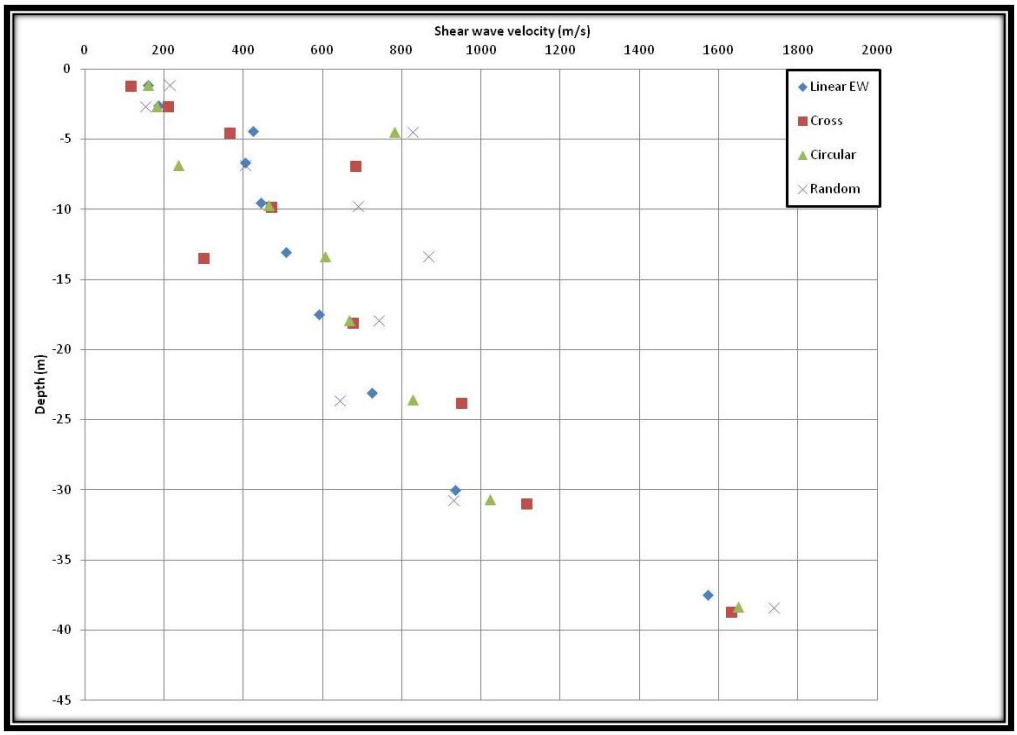


Figure 33. 1-D shear wave velocity profiles for conventional and random arrays calculated from the dispersion curve picks.

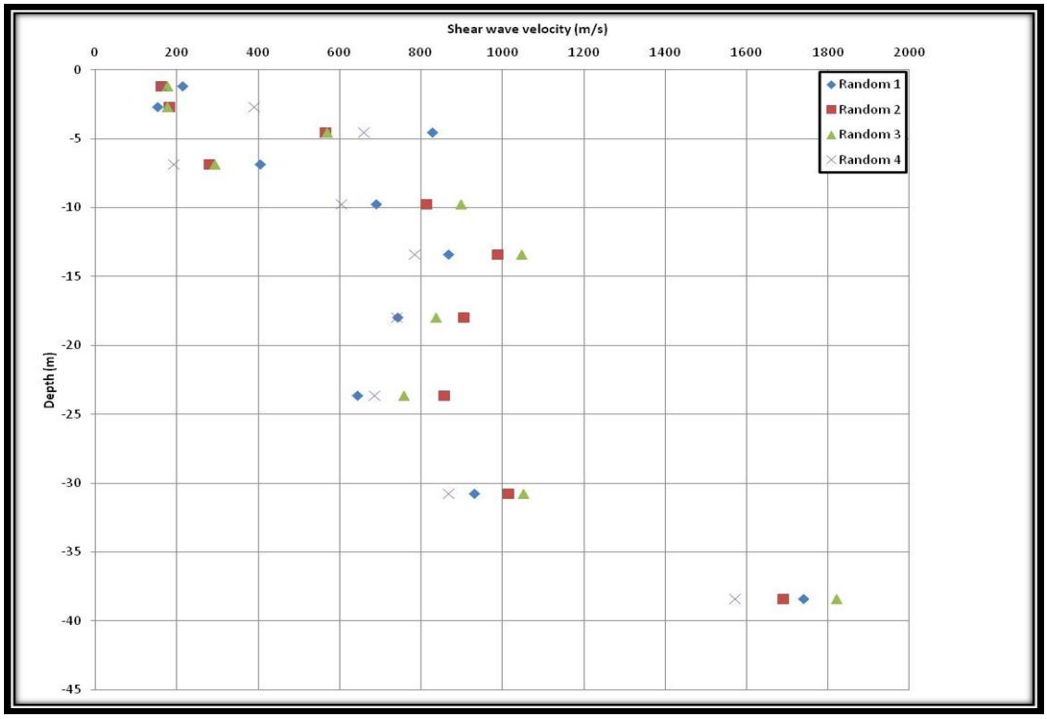


Figure 34. Graphical comparison of four different random array1-D Vs profiles.

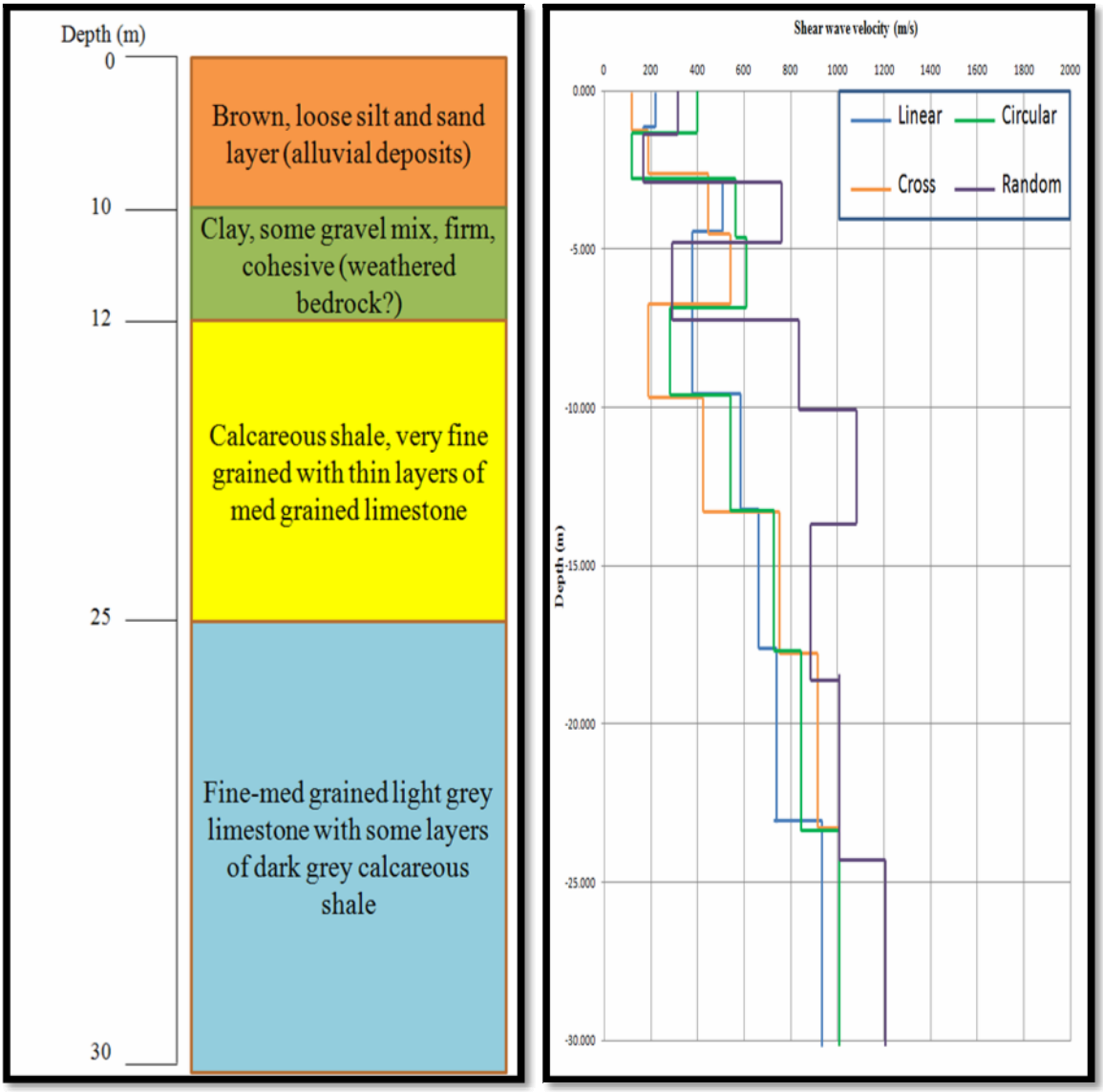


Figure 35 (a) Schematic stratigraphic column representing various soil layers with approximate depths (in meters) as obtained from the bedrock core hole log data. Four basic Lithologic units have been identified from the multilevel piezometer that was installed in bedrock hole. (b) All four 1-D Vs profiles shown together for close comparison.

6.5 STATISTICAL ANALYSIS

In order to further compare the datasets obtained from different array in more quantitative way, we performed an analysis of variance (ANOVA) on all eight data sets for both dispersion and inversion data sets. The results showing significance levels for various models and the

interaction between different geophone patterns with different variables (for example; frequency and phase velocity in case of dispersion data; and depth vs. Shear-wave velocity in case of inversion data) are tabulated in **Tables 7, 8, and 9**. Statistical analysis was also run on the 3 sets of data replicas and was observed that there is no significant difference within the data sets with respect to the frequency, phase velocity and Vs values (**Table 8**).

Table 7 summarizes the statistical analysis performed on dispersion data with a) frequency and b) phase velocity as a dependent variable and on inversion data with c) Vs as dependent variable. In the table, pattern represents the geophone arrangement (linear, cross, random etc.) and data represents the replicas collected for each arrangement. Following points can be inferred from the obtained values.

a) **Table 7 a** shows that there is no significant difference between the replicas ($\alpha > 0.05$) and also between the patterns within the data sets. But it is observed that there is significant difference within the patterns with respect to the frequency ranges.
b) **From Table 7 b** it can be observed that there is no significant difference between the replicas and the patterns within the data sets but there is a significant difference within the patterns with respect to the phase velocity values.
c) **From Table 7 c** it can once again be inferred that there is a significant difference within the pattern with respect to the shear wave velocity values and also between the depth and pattern a significant difference has been observed.

In order to further analyze the data to observe where the differences occur, each set of geophone array data is compared to the other array types using SPSS programming tool. The results are summarized in **Table 9**.

It is clearly observed that the linear, circular and cross array data correlate very well with the random 4 data but are significantly different from random 1, 2, and 3. Also it can be observed that there is no significant difference within the three random (1, 2, and 3) sets but they are significantly different from random 4. These results agree with the results obtained through graphical comparison. Some of these variations pertaining to the dispersion data in the three random sets (1,2, and 3) could be due to azimuthal variations in the subsurface materials that may have resulted in slightly different dispersion characteristics including different amount of higher modes energy.

6.6 CONCLUSIONS

Performed investigations of comparing the newly developed random array with four different types of MASW geophone arrays have shown that they are all quite effective in determining shallow shear-wave velocity profiles and that the results obtained from random array are comparable with that of the conventional arrays. Although there are some slight variations in Vs values within the arrays, obtained one-dimensional velocity profiles are similar to acceptable extent. The average shear-wave velocity in the 30 m thick layer of sediments is between 140 m/s to 155 m/s characterizing the soil to be soft soil. The depth to the bedrock could be identified at approximately 12 m depth in all receiver array types including the newly developed random array. It is also inferred from the field experiments that the more dispersive the geophones are in a random array, the better the resolution of the dispersion image, and thus the 1-D Vs interpretations. It can be concluded thus from the comparison of various receiver arrays, the estimated bedrock depths and proximal ground truth, that the interpretation of the 1-D MASW shear-wave velocity profiles from different array types is reasonably reliable and the random array profiles are quite comparable with that of the conventional to an acceptable level.

The implication is that the dispersion curves from various conventional and random receiver arrays are also reliable. Therefore, it can safely be concluded from this study that random arrangement of geophones can be used to determine the geotechnical properties of the subsurface.

Table 7. Statistical analysis performed on dispersion and inversion data using SAS and SPSS programming with dependent variables (a) frequency; (b) phase velocity (c) Vs. Pattern represents the geophone arrangement and data represents the 3 replicas obtained for each set of arrangement.

(a)

Dependent Variable: Frequency					
Source	DF	Type III SS	Mean Square	F Value	Pr > F
Pattern	7	1316.923	188.132	2.714	0.009
data	2	447.68	223.84	3.229	0.4
Pattern*data	14	988.545	70.61	1.019	0.432

(b)

Dependent Variable: Phase Velocity					
Source	DF	Type III SS	Mean Square	F Value	Pr > F
Pattern	7	3112916.827	444702.404	8.498	0.00
data	2	71446.172	35723.086	0.683	0.506
Pattern*data	14	984972.513	70355.179	1.344	0.8635

(c)

Dependent Variable: Vs					
Source	DF	Type III SS	Mean Square	F Value	Pr > F
Pattern	7	823349.116	117621.302	7.512	0.000
Depth*data	27	589955.467	21850.202	1.396	0.121
Pattern*data	11	2396607.787	21888.79	1.398	0.186
Depth*pattern	72	240776.689	33286.219	2.126	0.000

Table 8. Statistical analysis performed on the three replicas of both (a) dispersion and (b) inversion data using SAS and SPSS programming.

(a)

		Significance level	
		Frequency	Phs. Velocity
Data 1	Data 2	0.07	0.94
	Data 3	0.059	0.855
Data 2	Data 1	0.07	0.94
	Data 3	0.996	0.652
Data 3	Data 1	0.059	0.855
	Data 2	0.996	0.652

(b)

Dependent Variable:Vs		Significance level
Data 1	Data 2	0.421
	Data 3	0.61
Data 2	Data 1	0.421
	Data 3	0.074
Data 3	Data 1	0.61
	Data 2	0.074

Table 9. Statistical analysis performed on each array type using SAS and SPSS programming for (a) dispersion data with phase velocity as dependent variable; (b) inversion data with Vs velocity as dependent variable. The yellow columns represent significant difference between the arrays. For example the circular array in the first column is significantly different from random 1, 2, and 3 arrays both in the phase velocity and Vs velocity values but shows no significant difference from the other arrays.

(a)

Dependent Variable: Phase Velocity					
		Significance level			Significance level
Circular	Cross	0.329	Random 1	Cross	0
	Linear EW	1.000		Circular	0.041
	Linear NS	1.000		Linear EW	0.022
	Random 1	0.041		Linear NS	0.028
	Random 2	0.013		Random 2	1
	Random 3	0.015		Random 3	1
	Random 4	1.00		Random 4	0.023
Linear EW	Cross	0.325	Random 2	Cross	0
	Circular	1		Circular	0.013
	Linear NS	1		Linear EW	0.005
	Random 1	0.022		Linear NS	0.008
	Random 2	0.005		Random 1	1
	Random 3	0.007		Random 3	1
	Random 4	1		Random 4	0.006
Linear NS	Cross	0.311	Random 3	Cross	0
	Circular	1		Circular	0.015
	Linear EW	1		Linear EW	0.007
	Random 1	0.028		Linear NS	0.009
	Random 2	0.008		Random 1	1
	Random 3	0.009		Random 2	1
	Random 4	1		Random 4	0.008
Cross	Circular	0.329	Random 4	Cross	0.485
	Linear EW	0.325		Circular	1
	Linear NS	0.311		Linear EW	1
	Random 1	0		Linear NS	1
	Random 2	0		Random 1	0.023
	Random 3	0		Random 2	0.006
	Random 4	0.485		Random 3	0.008

(b)

Dependent Variable: Vs Velocity					
		Significance level			Significance level
Circular	Cross	0.842	Random 1	Cross	0
	Linear EW	0.641		Circular	0.025
	Linear NS	1		Linear EW	0
	Random 1	0.025		Linear NS	0.006
	Random 2	0.718		Random 2	0.692
	Random 3	0.047		Random 3	1
	Random 4	0.998		Random 4	0.003
Linear EW	Cross	1	Random 2	Cross	0.718
	Circular	0.641		Circular	0.052
	Linear NS	0.89		Linear EW	0.02
	Random 1	0		Linear NS	0.42
	Random 2	0.02		Random 1	0.692
	Random 3	0		Random 3	0.823
	Random 4	0.952		Random 4	0.3
Linear NS	Cross	0.977	Random 3	Cross	0
	Circular	1		Circular	0.047
	Linear EW	0.89		Linear EW	0
	Random 1	0.006		Linear NS	0.012
	Random 2	0.42		Random 1	1
	Random 3	0.012		Random 2	0.823
	Random 4	1		Random 4	0.006
Cross	Circular	0.842	Random 4	Cross	0.994
	Linear EW	1		Circular	0.998
	Linear NS	0.977		Linear EW	0.952
	Random 1	0		Linear NS	1
	Random 2	0.052		Random 1	0.003
	Random 3	0		Random 2	0.3
	Random 4	0.994		Random 3	0.006

Chapter-7

Forward modeling experiments for dispersion curve resolution pertaining to random array MASW

Note: This Chapter is written specifically to be submitted directly as a manuscript. Therefore, there is some repeated material and overlap with previous and subsequent chapters.

Yeluru, P.M., Baker, G.S., McMechan, G., and Penumadu, D., in prep.

ABSTRACT

The shear wave (Vs) velocity of near-surface materials (like soil, rocks etc.) and its effect on seismic wave propagation are of fundamental interest in many geotechnical and environmental studies. Advances in multi-channel seismic acquisition, either active or passive, in acquiring reliable 1-D or 2-D shear wave velocity profiles have greatly improved our ability to determine the engineering properties (e.g., Poisson's ratio) of Earth's shallow subsurface, especially when using the seismic multi-channel analysis of surface waves (MASW) technique. Also as lunar exploration advances and deployment of large structures, landing of large spacecraft, and excavating for mining or human habitation on the moon becomes necessary, a new scheme of using randomly distributed geophones that would be deployed from a mortar-type device, instead of a conventional linear array, will be critical because of the substantial logistical challenges associated with arranging an accurate linear or circular array robotically. Initial field results have shown that reliable dispersion curves can be obtained using random geophone array and that they are quite comparable with the dispersion curves obtained from conventional arrays. Influence of random geophone array on the resolution of dispersion curve using forward modeling method in multichannel analysis of surface wave (MASW) surveys is described here on a theoretical perspective of the dispersion curve imaging method used during a normal implementation of MASW method. Parameters like clustered geophones, skewness of receivers, different receiver numbers, and increased grid dimensions and their influence on dispersion image are described in this study.

7.1 INTRODUCTION

The multi-channel analysis of surface waves (MASW) seismic method (Park et al., 1999) utilizes a multi-channel seismic recording system to estimate near-surface S-wave velocity from dispersion property of high-frequency (>2 Hz) Rayleigh waves (**Figure 36**). The method has been steadily gaining popularity and attention from the near-surface geophysical and engineering communities, and has been successfully applied to various near-surface problems, such as mapping bedrock (Miller et al*.,* 1999), studying pavement structures (e.g., Ryden et al*.,* 2006) and liquefaction studies (e.g., Nazarian et al*.,* 1983). The MASW uses a multi-channel array, which makes it possible to distinguish the fundamental-mode from higher modes and body waves. Depending on the source used to generate surface waves, there are two types of MASW surveys: the active method that utilizes a controlled impact source like a sledge hammer, and the passive method that utilizes ambient noise such as vehicle traffic or tidal motion. The active method is considered to be the conventional mode of survey, collecting data in a roll-along mode using an active seismic source and a linear receiver array. The passive remote method utilizes ambient cultural noise such as traffic, thunder, tidal motion, etc., and employs a 2-D surface receiver array such as a cross, circular, or random array to record passive surface waves.

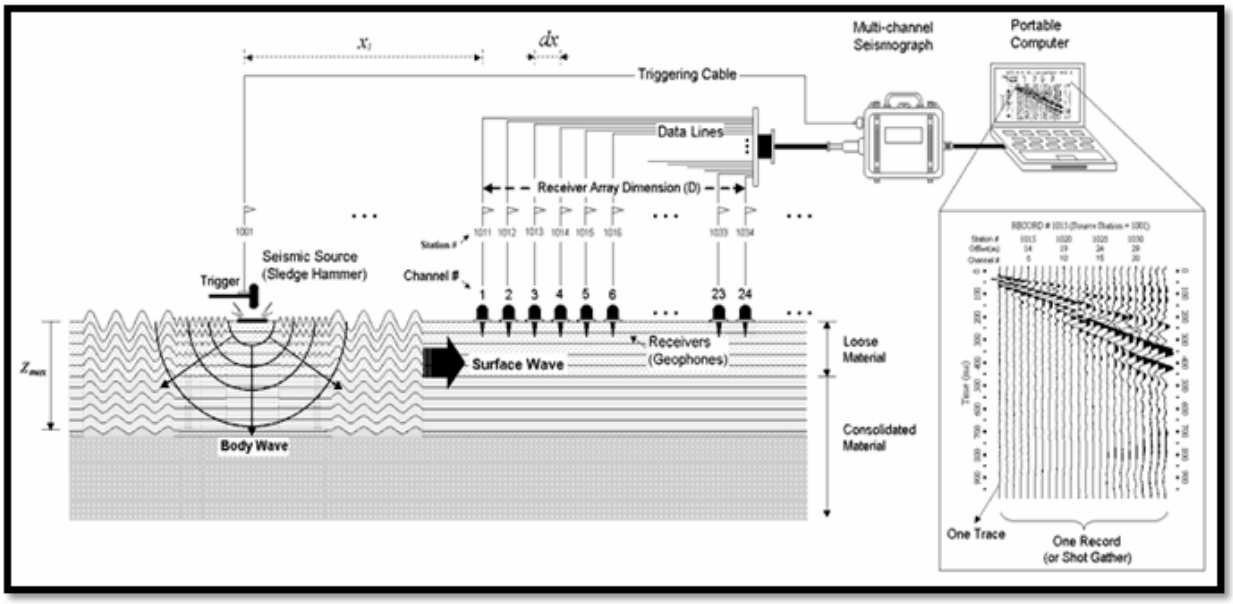


Figure 36. Typical multichannel seismic surface-wave experiment setup (modified from Park et.al., 1999)

A new scheme of using randomly distributed geophones that would be deployed from a mortar-type device instead of a conventional linear array is necessary for lunar exploration because of the substantial logistical challenges associated with arranging an accurate linear or circular array robotically. For example, rovers that are used to move around on lunar surfaces cannot easily move in a linear fashion or in a symmetrical circular motion to arrange the geophones due to constraints imposed by surface clutter such as rocks and boulders. Therefore it is difficult to arrange the geophones in an organized manner on a lunar surface or in any kind of urban areas for that matter, where some places are in accessible. Initial results indicate that robust dispersion curves (and thus subsurface models of engineering properties) are obtained from the random array geometries (Yeluru et.al. 2008). In this study, using forward modeling technique we analyze how various parameters like the skewness, number of geophones etc. influence the resolution of the dispersion image obtained from a random array.

Forward seismic modeling is a process through which a subsurface geologic model, in one-two- or three dimensions, is transformed into a synthetic seismic record of one-two or three dimensions. Synthetic seismic records are generated before and after the acquisition of seismic field data. Synthetic seismic records generated before field acquisition are used to determine if an intended/expected geologic target will generate an interpretable signature on output processed seismic data. Synthetics can also be a valuable tool with respect to the design of an acquisition program (for example; field acquisition parameters, sources, receivers etc.). The main idea behind forward modeling is to generate synthetic seismograms for a given geologic model of the subsurface and then compare it with the real seismic data acquired in the field. And if the two data sets agree closely within an acceptable level of accuracy, the assumed geologic model is considered to be a reasonably accurate model of the subsurface. If not, then the geologic model is altered, and a new synthetic record is computed and compared. This process is continued, iteratively, until a satisfactory match is obtained between the real and synthetic data. It is just the opposite of inverse modeling approach in which geologic parameters are computed from real data. But in reality, both the methods are used for the same goal-the determination of the geologic structure and lithology of the subsurface.

7.2 MODELING PROGRAM OVERVIEW

The modeling software used in this study is 3-D eighth-order staggered-grid finite-difference seismic modeling in anisotropic media using 21 elastic constants developed by the University of Texas-Dallas (UTD). This program synthesizes 3-component commons-source particle velocity seismograms for a 3-D anisotropic media (21 elastic constants) using eighth-order finite difference extrapolation on a staggered grid. The upper surface of the volume is

either the free surface (zero-stress) or an absorbing condition (using tapering). One run of the program produces one three-component common-source gather for a set of receivers at any specified locations, or for two intersecting linear arrays of receivers parallel to the horizontal axes. Hudson's (1980) second order scattering theory is used to parameterize media with dry or fluid saturated crack systems (Martinez). The complete system is coded in Fortran 77, and has been tested in Unix environment using a SUN E6000. More detailed explanation about the software can be found in the documentation (Martinez and McMechan). For this particular study, we set the surface to be a free surface (to obtain surface waves) and used the vertical component of the shot gather. Also the model parameters that were used for modeling experiments in this study are all mentioned in Appendix C.

7.3 THEORY OF SURFACE WAVE PROPERTIES

Elastic properties of near-surface materials and their effects on seismic-wave propagation are of fundamental interest in groundwater, engineering and environmental studies. In a vertically heterogeneous medium, the phase velocity of surface waves is a function of frequency (called dispersion curves). S-wave velocity is one of the key parameters in construction engineering (Rayleigh (1885) waves are surface waves that travel along a free surface. They travel elliptical in a counterclockwise direction. The motion is constrained to a vertical plane that is consistent with the direction of wave propagation. Therefore longer wavelengths penetrate deeper than shorter wavelengths for a given mode and generally exhibit greater phase velocities, and are more sensitive to the elastic properties of the deeper layers (Babuska and Cara, 1991). On the other hand, shorter wavelengths are sensitive to the physical properties of the surficial layers. Due to this reason, a particular mode of surface wave will possess a unique phase velocity

for each unique wavelength, leading to the dispersion of seismic signal. This dispersion curve thus obtained from Rayleigh waves is a function of shear wave (S-wave) velocity, layer thickness, density, and compressional wave (P-wave) velocity associated with each geologic layer, listed in the decreasing order of priority (Xia et al. 1999). Therefore, it is in principle possible to obtain S-wave velocity information from inverting the dispersive phase velocity of the surface wave (Dorman and Ewing, 1962; Aki and Richards, 1980; Mari, 1984). Rayleigh waves are non-dispersive in case of a solid homogeneous half-space and travels with a velocity of approximately 0.9194 v_1, if Poisson's ratio is equal to 0.25, where v_1 is the S-wave velocity in the half-space (Sheriff and Geldart, 1985). However, they become dispersive when its wavelengths are in the range of 1 to 30 times the layer thickness (Stokoe et al., 1994). They travel at a velocity equal to 0.9194 v_1 (where v_1 is the S-wave velocity of the layer) when the Rayleigh wave wavelengths are less than the layer thickness and they travel at a velocity equal to 0.9194 v_2 (where v_2 is the S-wave velocity of the half-space).

7.4 CONSIDERATIONS FOR NUMERICAL SIMULATIONS

Rayleigh-wave dispersion curves for any layered earth model (**Figure 37**) can be calculated by Knopoff's method (Schwab and Knopoff, 1972). Rayleigh-phase velocity, C_{Rj} is determined by a characteristic equation F in its nonlinear, implicit form:

$$F\ (f_j, c_{Rj}, v_s, v_p, \rho, h)=0 \quad (j = 1,2,\ldots,m) \quad \ldots\ldots..(7.1)$$

Where f_j is the frequency, in Hz; c_{Rj} is the Rayleigh-wave phase velocity at frequency f_j ; $v_s = (v_{s1}, v_{s2},\ldots..v_{sn})^T$ is the S-wave velocity vector, with v_{si} the shear-wave velocity of the ith layer; n is the number of layers; $v_p = (v_{p1}, v_{p2},\ldots..v_{pn})^T$ is the compressional P-wave velocity vector, with v_{pi} the P-wave velocity of the ith layer; and $\rho = (\rho_1, \rho_2,\ldots., \rho_n)^T$ is the density vector, with ρ_i the

density of the ith layer. So for a given set of model parameters (v_s, v_p, and ρ) and a specific frequency (f_j), the roots of equation (7.1) are the phase velocities. In this study, Hudson's (1980) second-order scattering formulism is used to compute the synthetic seismograms. A detailed work flow explaining systematic procedure for generating dispersion image from the synthetic seismogram is shown in **Figure 39**.

Table 10. A layered earth model parameters

Layer	Vs (m/s)	Vp (m/s)	Density (kg/m3)	Poisson ratio
1	168	421	2000	0.4
2	279	697	2000	0.4
3	340	850	2000	0.4
4	523	1308	2000	0.4
5	564	1409	2000	0.4
6	645	1614	2000	0.4
7	669	1673	2000	0.4
8	794	1985	2000	0.4
9	911	2278	2000	0.4
half space	1035	2589	2000	0.4

7.5 SENSITIVITY OF THE MODELING SOFTWARE

In order to test the sensitivity of the modeling program, one-dimensional high frequency rayleigh waves due to a ten-layered model (**Figure 37**) were simulated using the finite-difference method (Martinez et al). For starting model I took the velocities obtained from the inversion of random array MASW field data to generate the synthetic seismogram, and thus the dispersion image. The 1-D shear wave velocity profile thus generated from the above model is compared to the one obtained from the field data. If they correlate well with one another, then that layered model can be used for further simulations, if not, then the model parameters were changed until we get a reliable fit between the field and modeled data. A number of iterations were performed in order to get the best fit and the result is shown in **Figure 38** as: modeled curve which corresponds to the model parameters assumed, and field curve which corresponds to the Vs profile obtained from the field random data. The fit between the field and modeled curve in terms of velocity and depth is very good, except for a few depths which show some small variation (deviation) from the original field data.

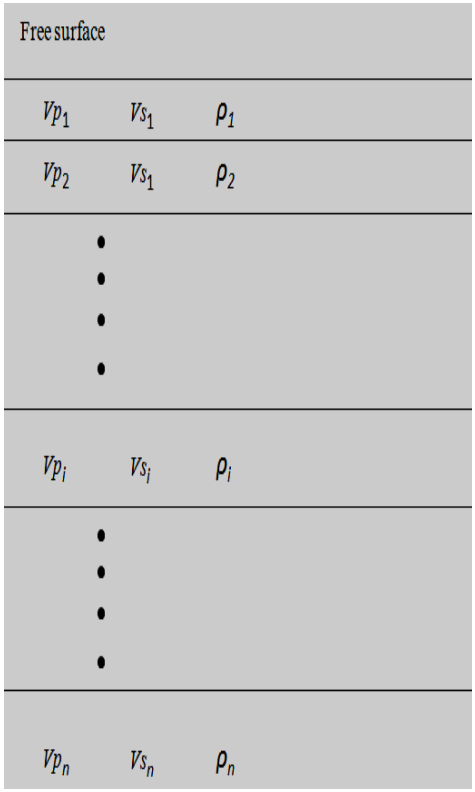


Figure 37. A layered earth model and corresponding parameters of compressional wave velocity (V_p), shear-wave velocity (V_s), and density.

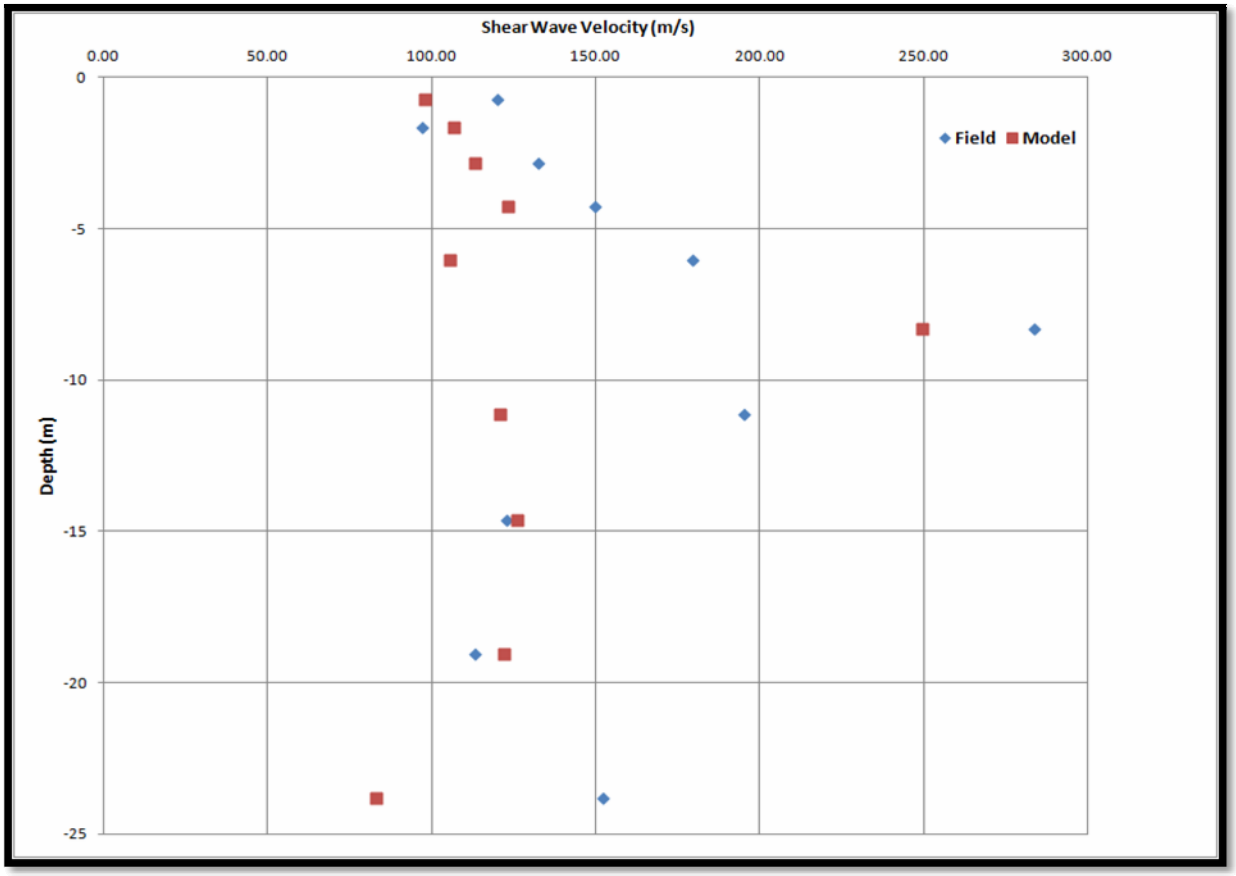


Figure 38. Graph representing correlation between the field and modeled data. The x-axis represents shear-wave velocity (m/s) and y-axis represents depth (m).

7.6 ANALYTICAL CONSIDERATIONS FOR DISPERSION CURVE ANALYSIS OF RANDOM ARRAY MASW

In case of a 2-D geophone array (like cross, circular, or random) the imaging and analysis of the dispersion curve deals with two main issues: 1) The sharpness of the image (which is usually controlled or judged by the thickness of dispersion image bands), and 2) how accurately it images the theoretical curves (we often observe some distortions at lowest frequency region of the dispersion image), and what kind of computational artifacts it generates. The resolution (sharpness) of the dispersion image is mainly controlled by the total length (D) of the receiver spread, which in case of a 2-D array is the maximum length of the array along the direction of

the source. The length of the receiver spread (D) is directly related to the longest wavelength (λmax) that can be analyzed from the dispersion curve, which in turn determines the maximum depth of investigation (Z_{max}). The mathematical relations associated with the above concepts can be expressed as;

$$D = mZ_{max} \quad (1 < m < 3) \ldots\ldots\ldots (7.2)$$

$$Z_{max} = 0.5\,\lambda_{max} \quad \ldots\ldots\ldots\ldots\ldots\ldots (7.3)$$

On the other hand, the receiver spacing (dx) is related to the shortest wavelength (λ_{min}) and therefore determines the shallowest possible depth of investigation (Z_{min}). It is given by;

$$Z_{min} = kdx \quad (0.3 < k < 1.0) \ldots\ldots (7.4)$$

The receiver spacing (dx) also determines the computational artifacts caused due to aliasing effect. It sometimes generates some curved streaks in the dispersion image that is caused at the point of dispersion where the wavelength becomes less than one half of dx. In case of random array, since the separation between each geophone is not constant, we calculate dx to be the minimum separation between two geophones, and this sometimes may cause the aliased streaks in the image.

Therefore for any given random array geometry, the one that satisfies the conditions of generating high resolution dispersion image and which results in longer wavelength (λ_{max}), is considered to be the most optimum method that can be utilized for acquiring random array MASW data.

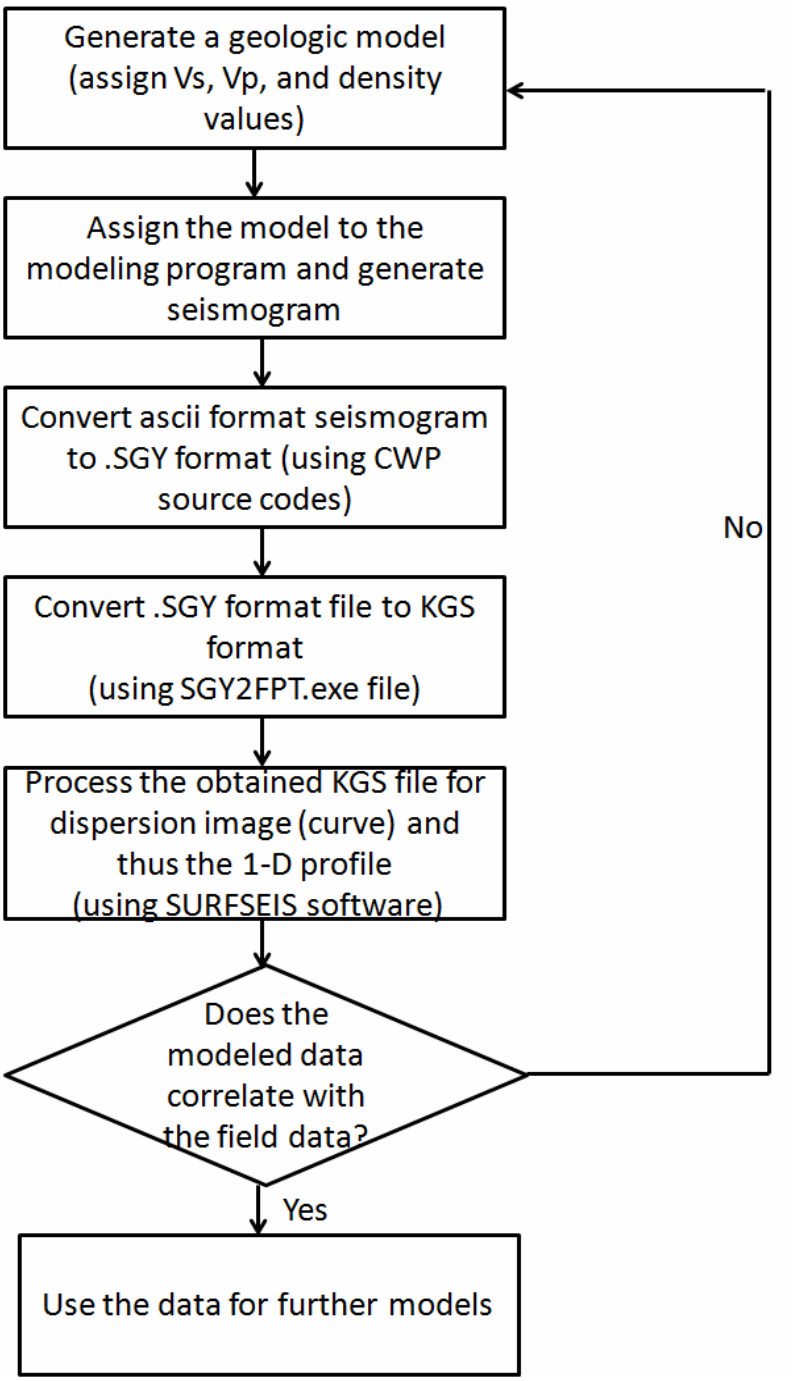


Figure 39. Flow chart explaining step-by step process of modeling shot gathers

7.7 MODELING RESULTS

7.7.1 Clustered Array

Many naturally occurring spatial distributions show a pronounced tendency toward clustering. Cluster analysis or Clustering, in general, means a group of the same or similar elements gathered or occurring closely together, as a bunch. In general sense, the process of clustering involves assigning a set of objects into groups (called clusters) so that the objects in the same cluster are more similar to each other than to those in other clusters. In this experiment, on the other hand, I generated 48 random numbers with different x-y coordinates and clustered them in such a way that most of the geophones are grouped at one places except for few scattered around inside the grid. Typical clustered arrangements used for this experiment are shown in **Figure 40**. The earth model from **Table 10** was used to generate seismograms for clustered random array. Shot gathers and corresponding dispersion images obtained in all four cases are shown in **Figure 41**. As can be observed from the cluster array figure, that out of the four, the geophones in cluster 2 are less clustered and that of cluster 4 are most clustered.

The main aspects for comparing dispersion images for various arrangements, as explained above, are the smoothness of the dispersion image/curve and the longest wavelength (λ_{max}) it can travel which ultimately determines the maximum depth of penetration (Z_{max}) of the surface waves used for analysis. It is observed that the dispersion images pertaining to cluster 1, 2, and 3 do not cause any appreciable change in resolution except for cluster 4 which has lowest resolution of all. The longest wavelength travelled by a surface wave can be calculated from the dispersion curve extracted from the image by selecting the phase velocity (C) pertaining to the lowest frequency (f_{min}) and using the basic relation:

$$\lambda_{max} = C/f_{min} \quad \ldots\ldots\ldots(7.5)$$

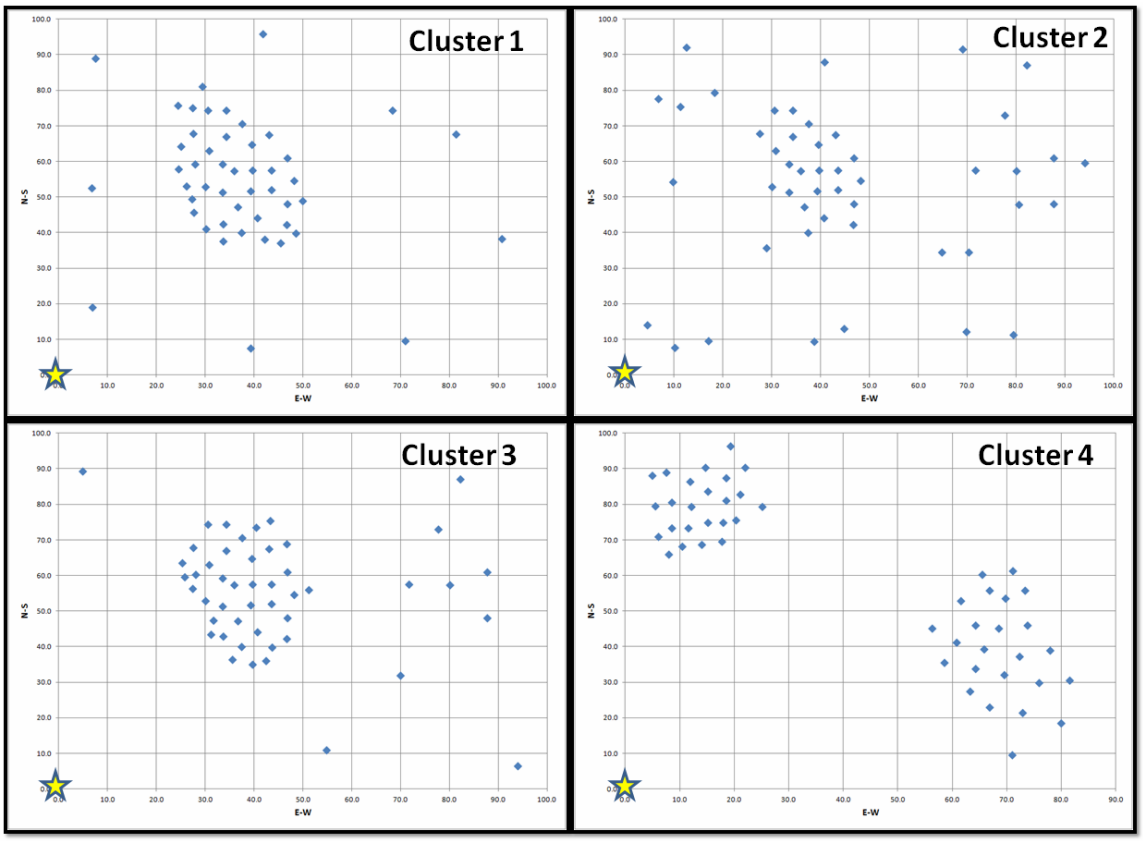


Figure 40. Four different cluster array geometries used in the modeling. The x-axis represents the E-W direction and y-axis represents the N-S direction. The star represents the shot point location (which is located at the origin).

Table 11 illustrates different λ_{max} values obtained for different cluster arrays and it is observed that cluster 2 has the highest and cluster 4 has the lowest λ_{max} value. It can be observed from figure 6 that out of the four geometries, cluster 2 is the least clustered and cluster 4 the most clustered array. Therefore based on all the above facts, it can be interpreted that the less clustered the receiver spread is the more better the resolution of the dispersion image and the larger the depth of penetration (Z_{max}).

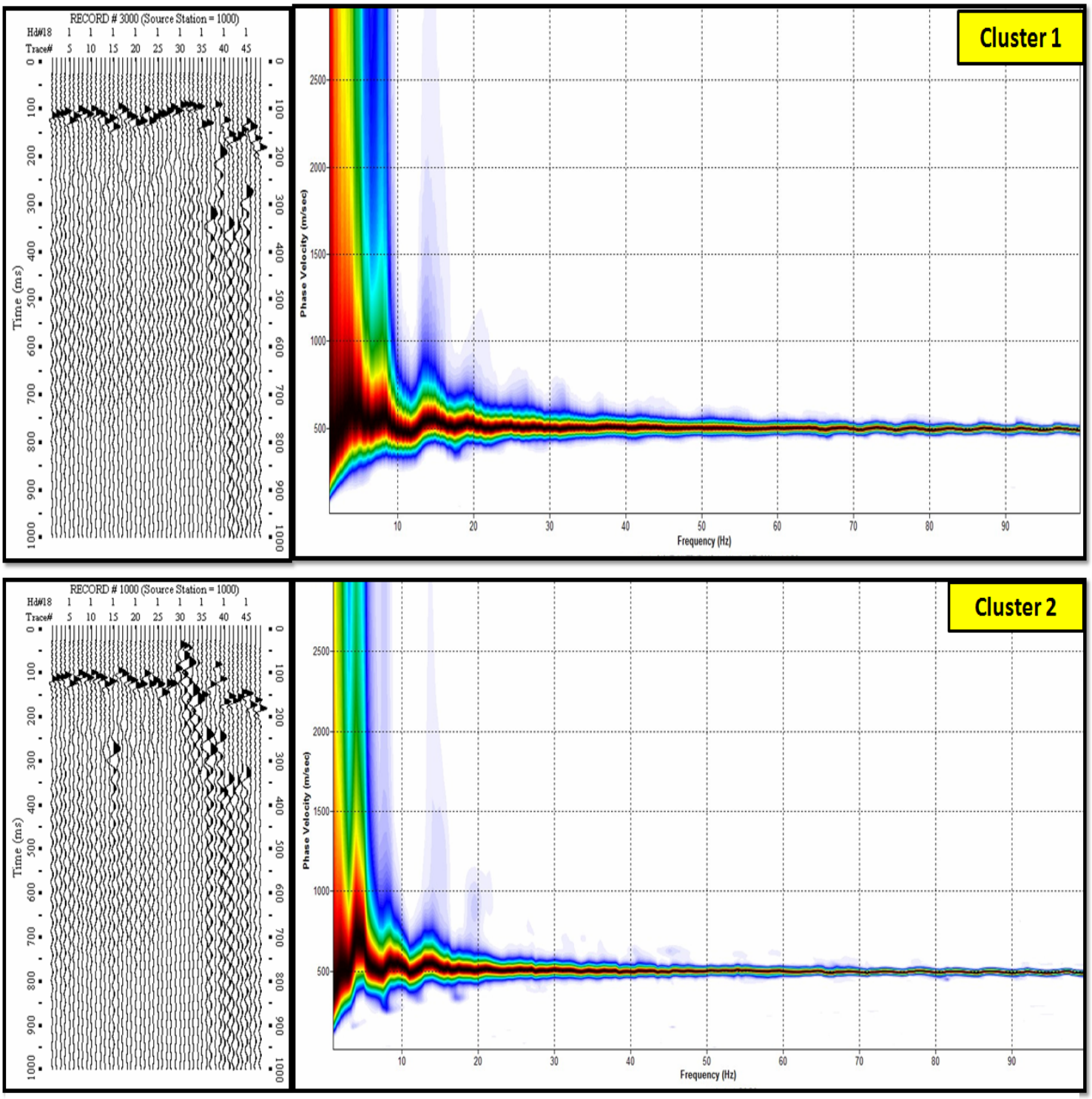


Figure 41. Shot gathers and corresponding dispersion images obtained for four different clustered arrays. The X-axis represents frequency range 1-100 Hz and Y-axis represents phase velocity range 10-3000 m/s

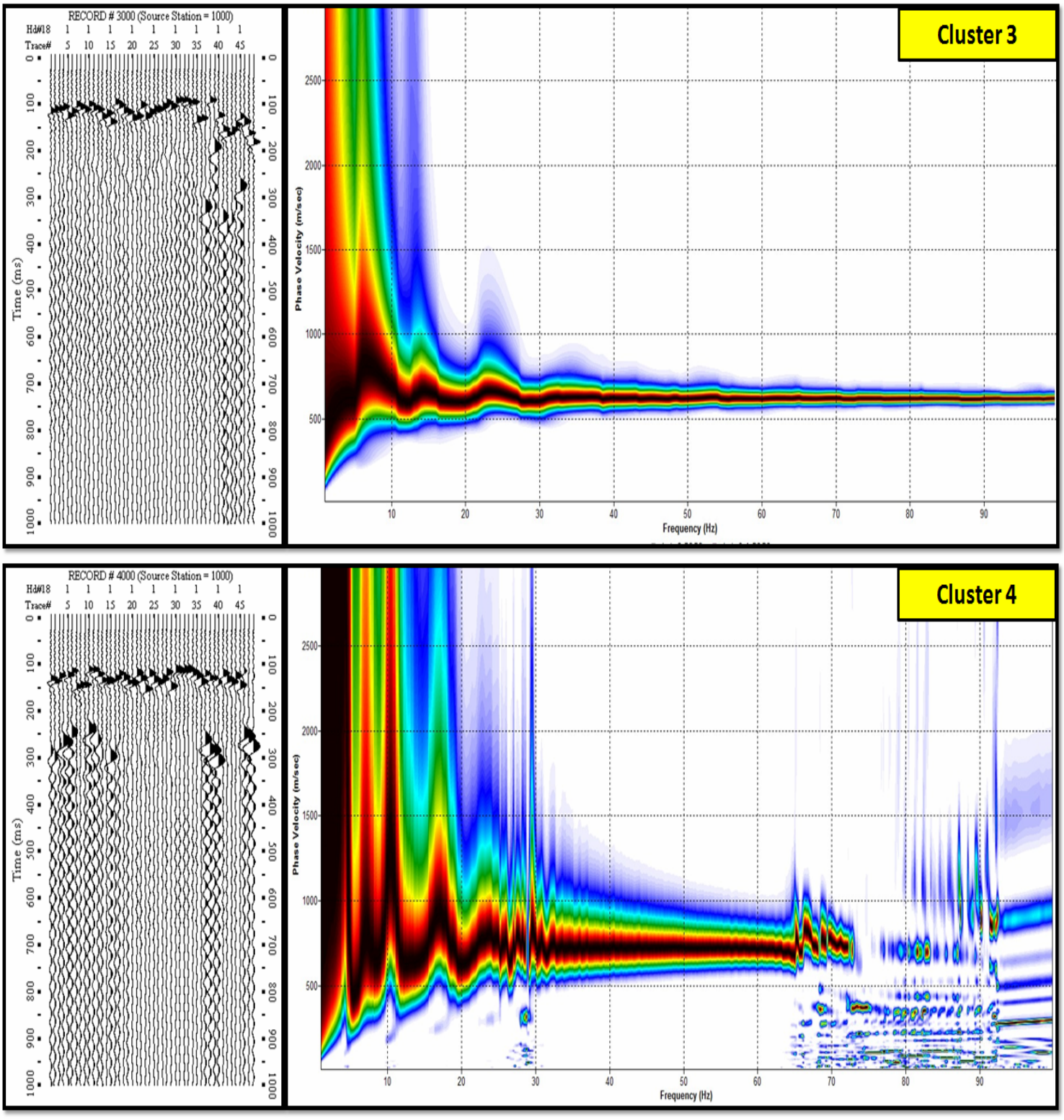


Figure 41. (contd…).

Table 11. Longest wavelength (λmax) and corresponding approximate depth of investigation (Zmax) calculated for each type of configuration

Array type	λmax(m)	Zmax(m)
cluster 1	176	88
cluster 2	183	92
cluster 3	159	79
cluster 4	98	49
normalskew	118	59
leftskew	115	58
rightskew	93	47
24 chan	163	82
48 chan	243	121
96 chan	226	113

7.7.2 Skewness Effect

In statistical terms, skewness is a measure of the symmetry of the probability distribution of a real-valued random variable. The skewness value can be positive or negative, or even undefined (from http://en.wikipedia.org/wiki/Skewness). A positive skew indicates that the mass of the distribution is concentrated on the left side of the figure. It has relatively few high values and the right tail is longer. A negative skew on the other hand indicates that the mass of the distribution is concentrated on the right of the figure. It has relatively few low values and the left tail is longer.

A zero value usually indicates that the values are relatively evenly distributed on both sides of the mean, implying a symmetric distribution (http://en.wikipedia.org/wiki/Skewness). Using this concept ninety-six (96) skewness values were generated using SPSS statistical programming tool for normal, right, and left skew values. The distribution of the geophones around the grid for all three cases is shown in **Figure 42**.

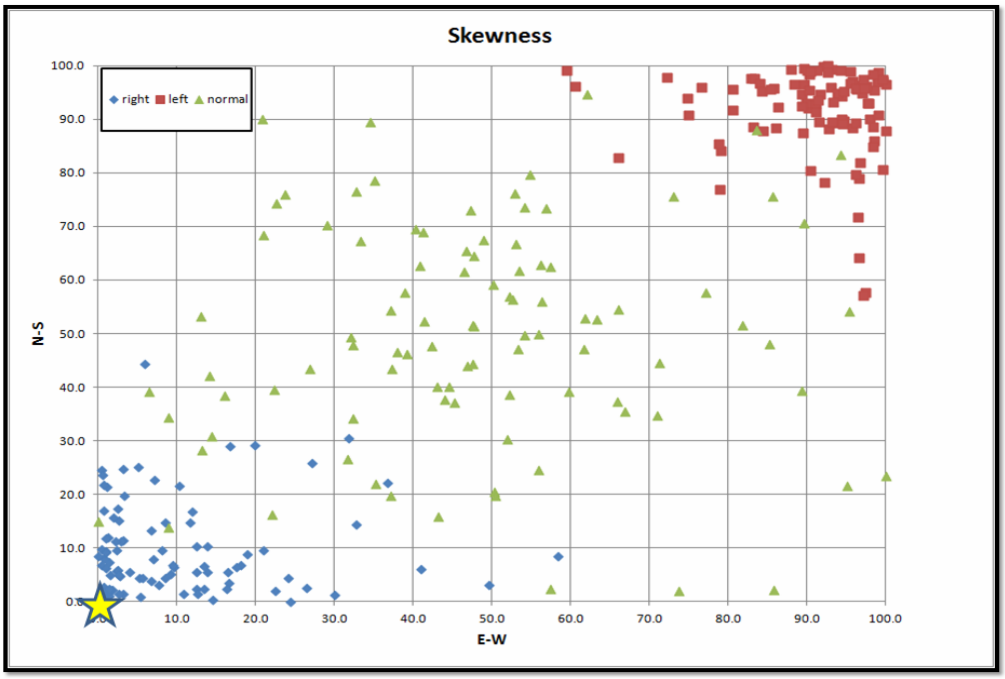


Figure 42: Graphical setup for the geophone coordinates as deployed around the grid for normal, left and right skewed data. The star represents the source location (at origin) in all three cases.

Considering such situation could be critical on lunar or any other kind of planetary surface, when there might occur a case where the geophones could all be skewed to either right or left while being deployed robotically or by an astronaut. **Figure 43** shows the shot gathers and the influence under the skewness condition on dispersion image resolution. In this figure it can be observed that the normal skew data results in higher resolution dispersion image for obvious reasons. But the images obtained from right and left skew also shows a prominent dispersion image. Taking into consideration the fact that the geometry pertaining to higher λ_{max} value is considered to be the best possible one, the dispersion curves for all three cases were processed for frequency range 1-100 Hz with 5 Hz increment and the phase velocity (C) for a range 10-3000m/s with 10 m/s increment. The phase velocity (C) corresponding to f_{min} was determined. Then by using equation 5 the longest wavelength travelled by surface waves in each case was calculated. It is observed in

this case (Table 11) that a normally skewed geophone arrangement yields the highest λ_{max} and posses the best resolution dispersion image.

7.7.3 Total Number of Traces

The total number of traces (***N***) takes into account the number of traces included in a data set being analyzed for dispersion curves. It is also equal to the number of channels used if one shot gather is being analyzed. **Figure 44** illustrates the effect of ***N*** on resolution of dispersion image and it is clearly observed that more number of traces results in higher resolution. There are certain factors that can be associated with the total number of traces like the length of spread (***D***), or the receiver spacing (***dx***) both of which were held constant in this case. It has been examined from previous results (Park et.al., 2001) that a higher number of channels can always result in high resolution dispersion image only when accompanied by an increase in ***X*** and it is not of any benefit if we just increase ***N*** without any increase in ***X***. Also the receiver spacing (***dx***) should be long enough to record surface waves but too long would cause spatial aliasing problems (Park et al., 2001)

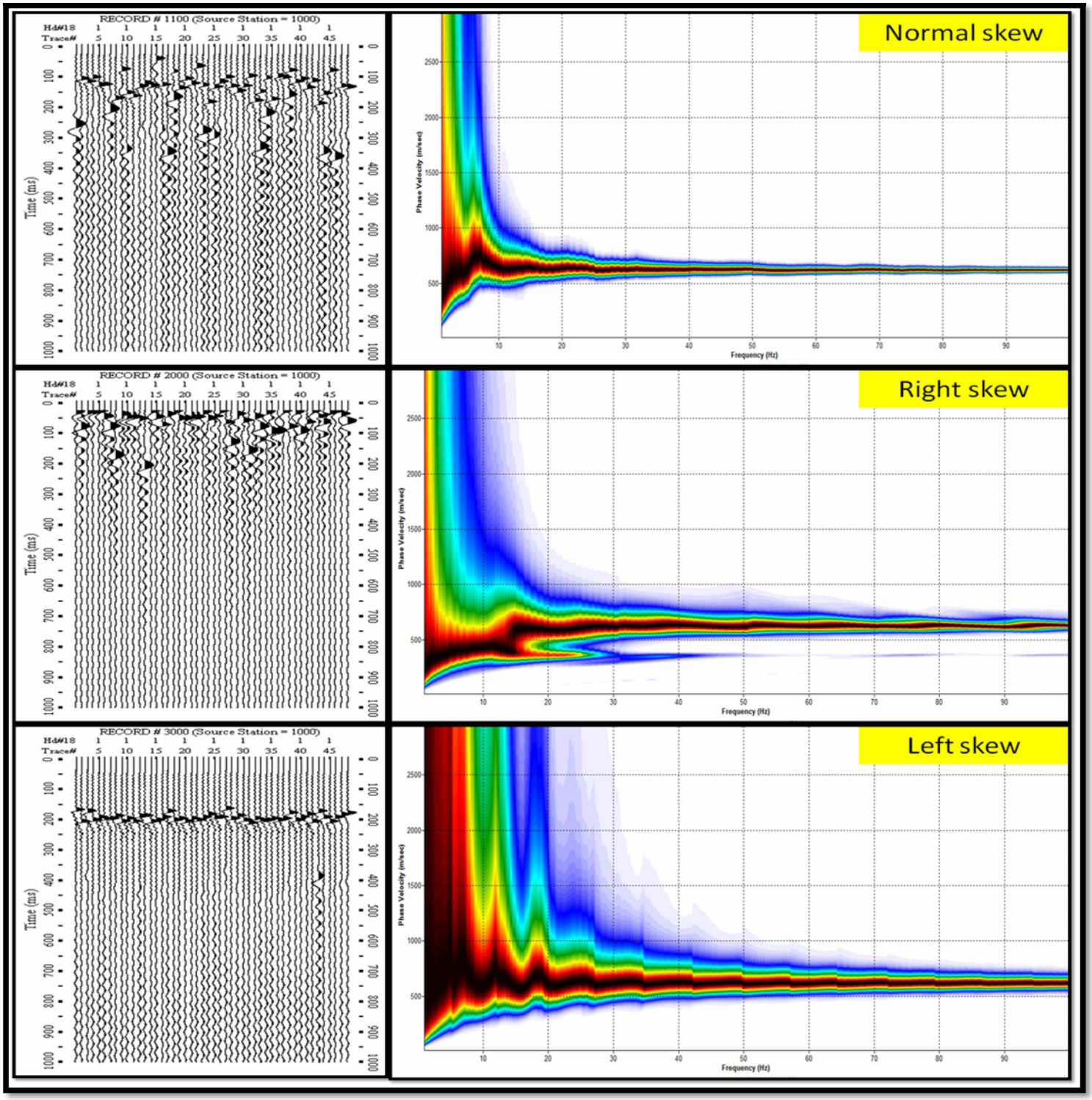


Figure 43. Shot gathers for Normal, Left and Right skewed models and their corresponding dispersion images. The X-axis on the dispersion image represents frequency (Hz) range 1-100 Hz and the Y-axis represents phase velocity (m/s) range 10-3000 m/s.

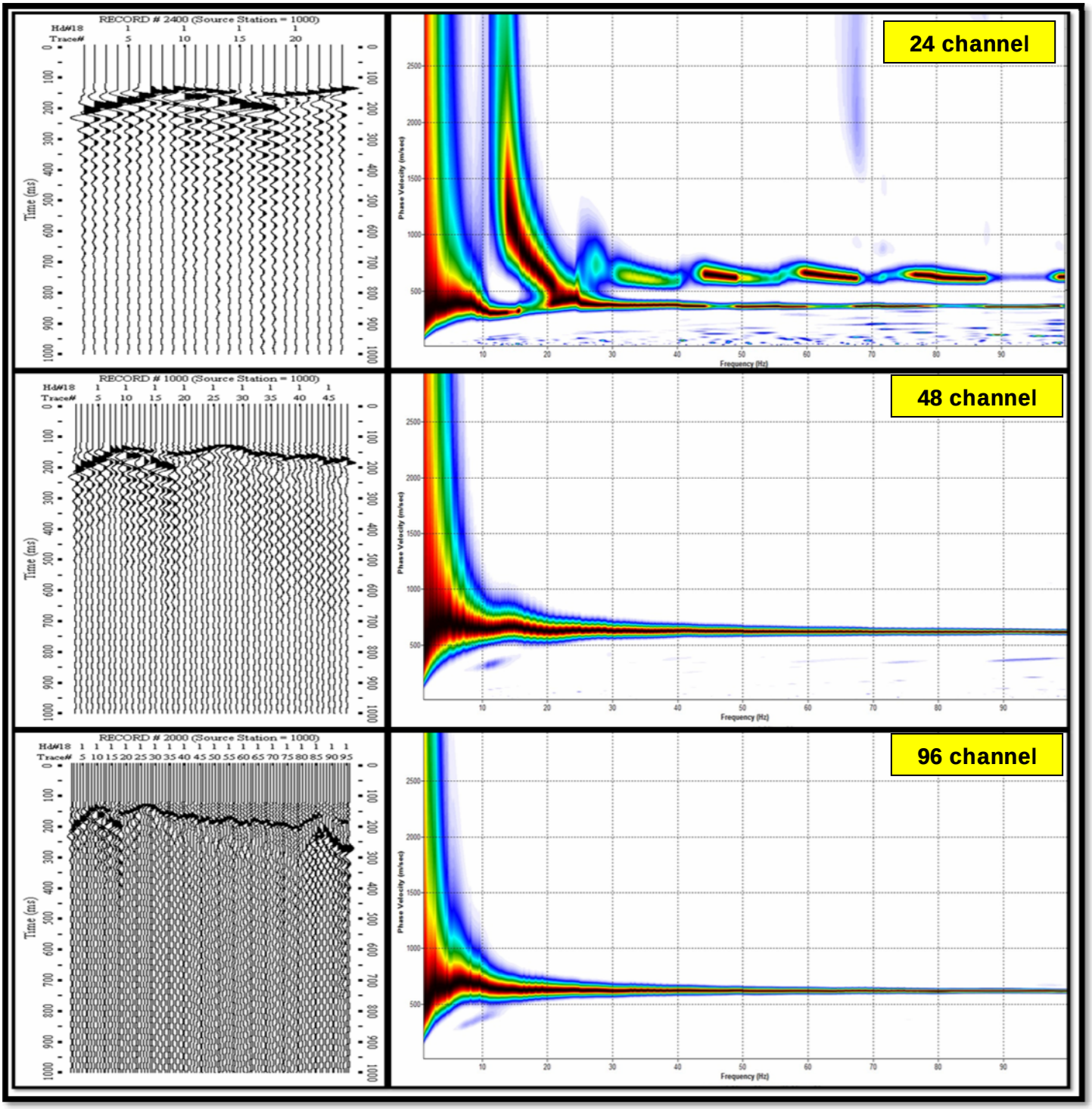


Figure 44. Modeled shot gathers and corresponding dispersion images for different number of channels. The X-axis represents frequency range 1-100 Hz and Y-axis represents phase-velocity range 10-3000 m/s.

7.8 DISCUSSION

In this study the influence of some key acquisition parameters pertaining to random array geometry on the resolution of dispersion image has been examined. All the results were examined and interpreted purely on theoretical basis explained in the previous sections. Although reliable data results and key parameters concerning the acquisition design can be obtained from forward modeling experiments, there are always other factors that need to be considered while collecting real field data. Some of them include near and far field effects (Park et al., 1999), lateral inhomogeneity in the subsurface and other surficial objects that may disturb the measurements. Therefore all these factors should be considered along with the parameters explained above while determining the optimum parameters for a random array MASW survey.

7.9 CONCLUSIONS

The following conclusions can be drawn based on formulistic perspective of the dispersion curve analysis for a random array MASW survey.

- The least clustered (more dispersed) random geometry is preferred in order to obtain higher resolution dispersion image and a higher λ_{max}.
- A normally skewed geophone array yields a better resolution dispersion image and a higher λ_{max}.
- A higher number of traces results in a higher resolution dispersion image, but it is necessary to increase the number of traces only if you are increasing the area of coverage.

CHAPTER-8

Adapting a random-array acquisition scheme for a seismic surface-wave study of a lunar analog site at Black Point Lava Flow, Arizona USA, as a potential rover-friendly methodology

Note: This Chapter is written specifically to be submitted directly as a manuscript. Therefore, there is some repeated material and overlap with previous and subsequent chapters.

Yeluru, P.M., Baker, G.S.,, and Park, C.B., in prep.

ABSTRACT

The geology of Earth's moon has previously been examined via telescopic observations, orbiting spacecraft readings, lunar sample analysis, and also from some geophysical data. Previous researchers have examined layering of the moon and models exist explaining the velocity variations in the mantle and core (Wieczorek et al., 2006). Also, many studies and measurements were made to determine various physical properties of the lunar surface at depths varying from a few micrometers to a few tens of centimeters (Carrier et al., 1991). There is an increasing need to understand the geotechnical properties of the lunar surface as plans progress to send robotic rovers to the moon, and as more thought is given to construction of lunar bases and other lunar facilities (Carrier et al., 1991) . Geotechnical or Engineering properties are those properties that effect construction and engineering. Engineering properties--like shear strength, shear modulus and Poisson's ratio--are key parameters for civil engineering works, as they characterize the mechanical behavior of geotechnical materials under various types of loading. Therefore, understanding the physical and engineering properties within the upper 30 m of the lunar subsurface will be critical for lunar exploration if deployment of large structures, large-scale excavation, and/or landing of large spacecraft on the surface is desired. The geotechnical measurements taken or measured till date on the lunar surface were either *in situ* (by robots and astronauts) by drilling holes into the surface or by using cone penetrometer techniques which are invasive (require drilling boreholes) techniques, by remote sensing from the Earth's surface and from lunar orbit or in the laboratory on returned samples. However, no studies (or datasets) currently exist regarding the engineering properties of the shallow (<30 m) lunar subsurface that were acquired using near surface seismic methods. Advances in near-surface geophysical techniques, such as Multi-channel Analysis of Surface Wave (MASW), has greatly increased our

ability to map subsurface variations in physical properties. The MASW method involves deployment of multiple seismometers to acquire 1-D or 2-D shear wave velocity profiles that can be directly related to various engineering properties. The advantage of this technique over drilling boreholes or any other geophysical technique is that it is less intensive, non-invasive, more cost-effective, and more robust because strong surface-wave records are almost guaranteed. In addition, data processing and analysis is fairly straightforward, and the MASW method allows for analysis of a large area of interest as compared to drilling boreholes. The purpose of this work is to demonstrate the usefulness and capabilities of MASW technique at terrestrial lunar analog sites where the geologic settings, processes and/or materials are somewhat similar to those encountered on the Moon. This study mainly focuses on near surface seismic studies and interpretation of the subsurface geology using random geophone array. A random array is necessary for lunar exploration because of the logistical constraints involved in deploying a linear or circular array robotically or by astronaut.

8.1 INTRODUCTION

Multichannel Analysis of Surface Wave (MASW) data from terrestrial analog environments can help constrain models for evolution of the lunar subsurface and help predict the nature of subsurface properties encountered during future landed scientific or engineering operations on the Moon. MASW method can yield insight into mapping subsurface variations in physical properties, and other important engineering properties of the subsurface—like shear modulus, shear wave velocity and Poisson's ratio (Park et al., 1999), that are the key parameters for any type of civil engineering works, as they characterize the mechanical behavior of geotechnical materials under various types of loading. Multi-channel surface wave data was collected at Black Point Lava Flow (BPLF) site which is 40 km north of Flagstaff, Arizona in

March 2012. This field test was primarily intended to determine the engineering parameters, like shear wave velocities, at a high-fidelity lunar mission simulant using MASW method with randomly distributed geophone arrangement. Such type of array will be necessary for future lunar exploration keeping in mind the logistical constraints involved in deploying a linear or circular array robotically or by astronaut. An initial study (Yeluru et al., 2008) has proven that robust and reliable dispersion images could be obtained using random geophone array. This information obtained on the Moon using this technique should prove to be critical based on the anticipated engineering needs of lunar exploration and on the extreme logistics imposed by lunar exploration. Here, I present a description of the experiment conducted and the results thus obtained.

8.2 LUNAR ANALOG SITES FOR SEISMIC STUDIES

Analog sites are places or spaces on earth that approximate, in some respect, the geological, environmental and putative biological conditions or settings on a particular planetary body, either at the present day or sometime in the past (from en.wikipedia.org/terrestrial analogue sites). Therefore, an analogue may be broadly defined based on the conditions the site is meant to represent and the specific parameters meant to be examined/tested. For example, a meteoritic impact crater site is an obvious analog for the moon where surface geometry, etc. are of interest, whereas a basalt lava plateau that has undergone severe physical weathering is an equally legitimate analog site if the physical properties of the subsurface are of interest. The use of a lunar analog site is an essential component in the development of systems that are planned for lunar and planetary exploration. Also analog experiments help aid astronauts, engineers and scientists to enhance scientific exploration by combining human and robotic efforts. Analogs can

be used to test robotics, vehicles, habitats and in-situ resource utilization in realistic environments that will help us better prepare and understand the complex challenges that will be encountered on the moon.

Selecting an analog site that would best suit my proposed research is an integral element, capable of influencing data and impacting test results. Examples of relevant characteristics of a lunar analog site for my work include terrains, soil properties, meteorology, geologic features, biological changes and remoteness. Investigation of surface processes and comparative studies with other planetary bodies can be carried out using several techniques and methods including, but not limited to, (1) fieldwork and remote-sensing campaigns at terrestrial analog sites; (2) comparisons between terrestrial and planetary datasets; and (3) numerical and computer modeling of geological processes (Tornabene et al.,2005). Few of the many terrestrial analog sites, within United States which are suitable for lunar analogs were studied in detail and the Black Point Lava Flow (BPLF) site was selected. Various locations that can serve as a lunar analog site are explained below (from www.nasa.gov).

Antarctic

These kinds of places are mainly used to test the inflatable habitat concept. When astronauts return to the moon for extended stays, they will require shelter to live and work under for protection from the harsh lunar environment. The site selected was the cold, isolated landscape of Antarctica.

Oceans

Ocean conditions such as the Florida Keys National Marine Sanctuary, serves as a test site for NASA's Extreme Environment Mission Operations. NASA uses the laboratory's lunar-like environment as a semi-permanent site for testing lunar exploration concepts such as

advanced navigation and communication equipment. Astronauts also execute a variety of undersea "moonwalks" at this site. The tests cultivate an astronauts understanding of his or her ability to carry out daily operations in a simulated planetary environment.

Deserts

These sites are used to measure the benefits of using pressurized vehicles as opposed to unpressurized vehicles, and incorporate the findings into upcoming lunar missions. These sites are also needed to conduct short-distance mobility exploration and also engineering evaluation tests to investigate the utility of its robotic vehicle concepts in an earthly moonscape. For this purpose NASA found the sand dunes of Moses lake, Washington. And the desert-like landscape in Black Point Lava flow, Arizona is well suited for testing technologies and procedures for future human-robotic exploration in extreme environments.

Volcanic Terrains

The terrain, rock distribution and soil materials at such sites as in Hawaii and Idaho provide an ideal simulated environment for testing hardware and other equipment to harness local resources for use in human and robotic exploration.

8.3 GEOLOGIC SETTING-BLACK POINT LAVA FLOW

The San Francisco volcanic field is an area of volcanoes in northern Arizona, north of Flagstaff, USA. This field contains approximately 600 volcanoes in age from less than 6 million years old to less than 1,000 years (Miocene to Holocene). The Black Point Lava Flow (BPLF) is a part of the San Francisco volcanic field which is approximately 2 million years old (from en.wikipedia.org/San Francisco field site). Stretched across much of the northern Arizona, the

Black Point Lava Flow resembles an alien landscape on Earth, the perfect place for NASA to test rovers, habitats, space suits and the other equipment that future astronauts will need when they explore the moon, the asteroids as well as Mars and the Moons of the Red Planet (from http://spacecoalition.com). It is considered one of the best and excellent sites for surface system analog sites, because it shares so many terrain and environmental similarities with the Moon, Mars, and near Earth asteroids (from www.nasa.gov). Like so many other planetary bodies, Black Point Lava Flow (**Figure 45**) is a desolate environment with rugged terrain, dust storms, varying soil composition, temperature extremes, deep craters, steep slopes, rolling plains, and volcanic ash fields (from www.earthobservatory.nasa.gov). The BPLF was first considered as a candidate for field testing during the Apollo program. Along with the great combination of Moon- and mars-like features, Black Point Lava Flow is a good analog site for any kind of field experiments because of its large size. It is large enough to accommodate multiple extended missions, including day-long scenarios and long-duration traverse operations. It has enough space to fit a large science and engineering teams (from www.nasa.gov). Considering all the advantages at this site, it is chosen to be an excellent setting for training and systems testing for future exploration missions to the moon.

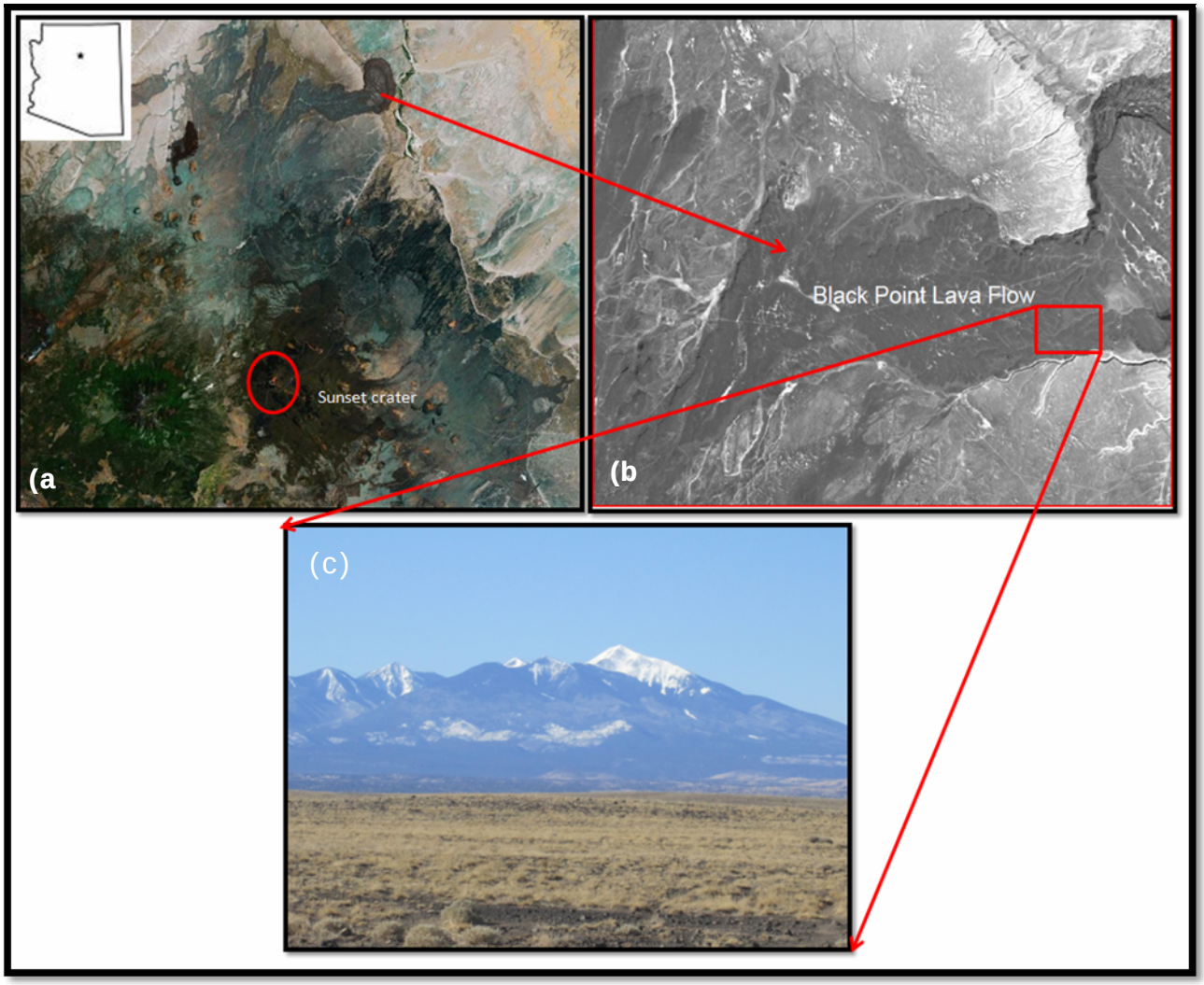


Figure 45. (a) Sunset crater and the Black Point Lava Flow (BPLF), north of Flagstaff, AZ. (b) Box marks the far-east side of the BPLF where seismic data was collected. (Google Earth) (c) A snapshot of the field site.

8.4 FIELD TEST PROCEDURE

The three day field test consisted of collecting MASW data for three different receiver array types: Linear (east-west and north-south traverse), Cross and Random arrays.

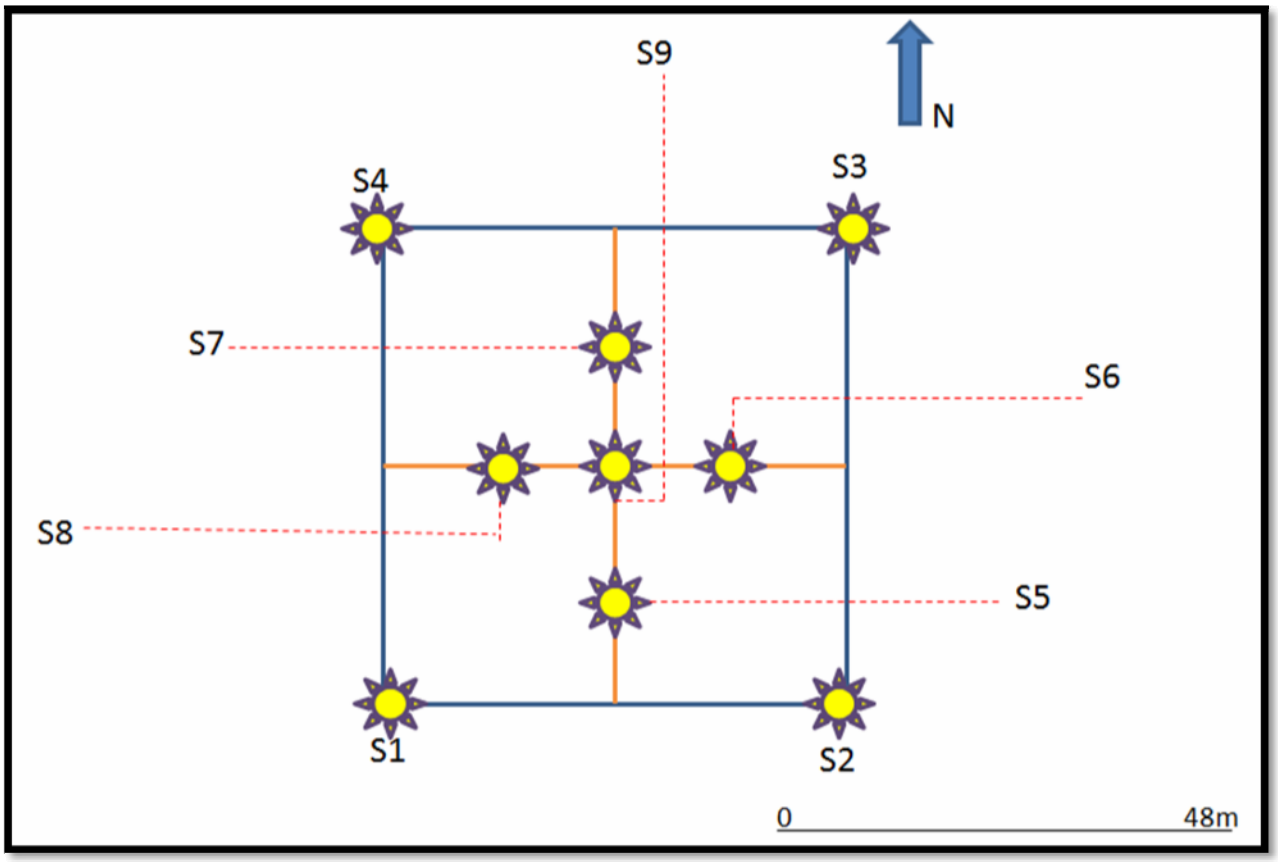


Figure 46 (a). The figure represents the shot point locations as deployed on the ground. There are a total of nine shot points for the 2-D arrays. The yellow markers represent the shot point locations.

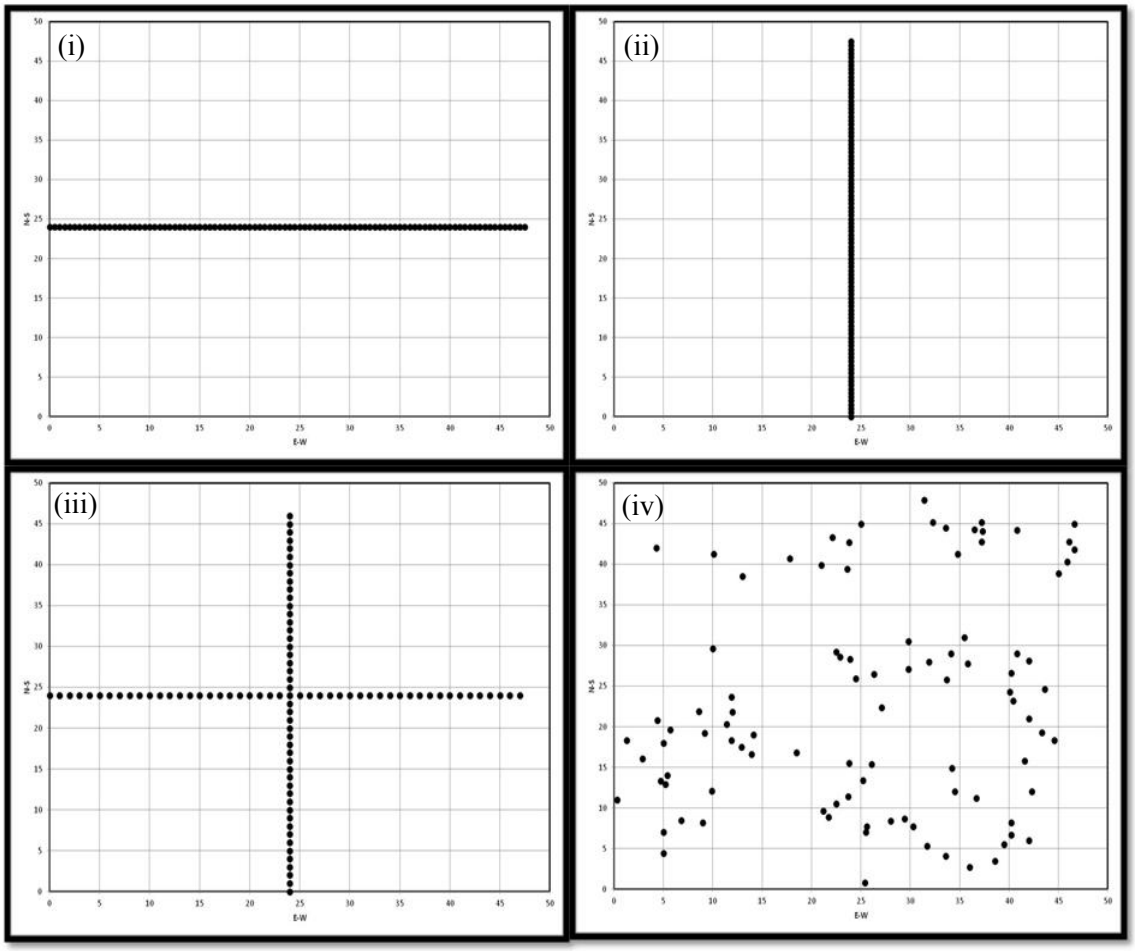


Figure 46 (b). Schematic representation of various receiver arrays as deployed in the field. X-axis represents E-W traverse and Y-axis represents N-S traverse (i) Linear EW (ii) Linear NS (iii) Cross (iv) Random.

8.4.1 Data acquisition

Multi channel data were collected on the BPLF site in Flagstaff, Arizona, using a 96-channel Geometrics start view seismograph with 14 Hz geophones. A 10-lb sledge hammer was used as a seismic source to generate source energy and data was collected on a 48m×48m grid (**Figure 46 a**). Fifteen shot records were shot for the linear arrays (EW and NS traverses) and nine records were shot for cross and random arrays. Graphical representations of various arrays are shown in **Figure 46 b** and a summary of data acquisition parameters are tabulated in **Table 12**. A time sampling interval of 0.5 ms and a total recording time of 1000 ms were used during data

acquisition. No acquisition filter was applied during the recording. Three sets of data were collected for each array. Typical shot gathers for each type of array are represented in **Figure 47**.

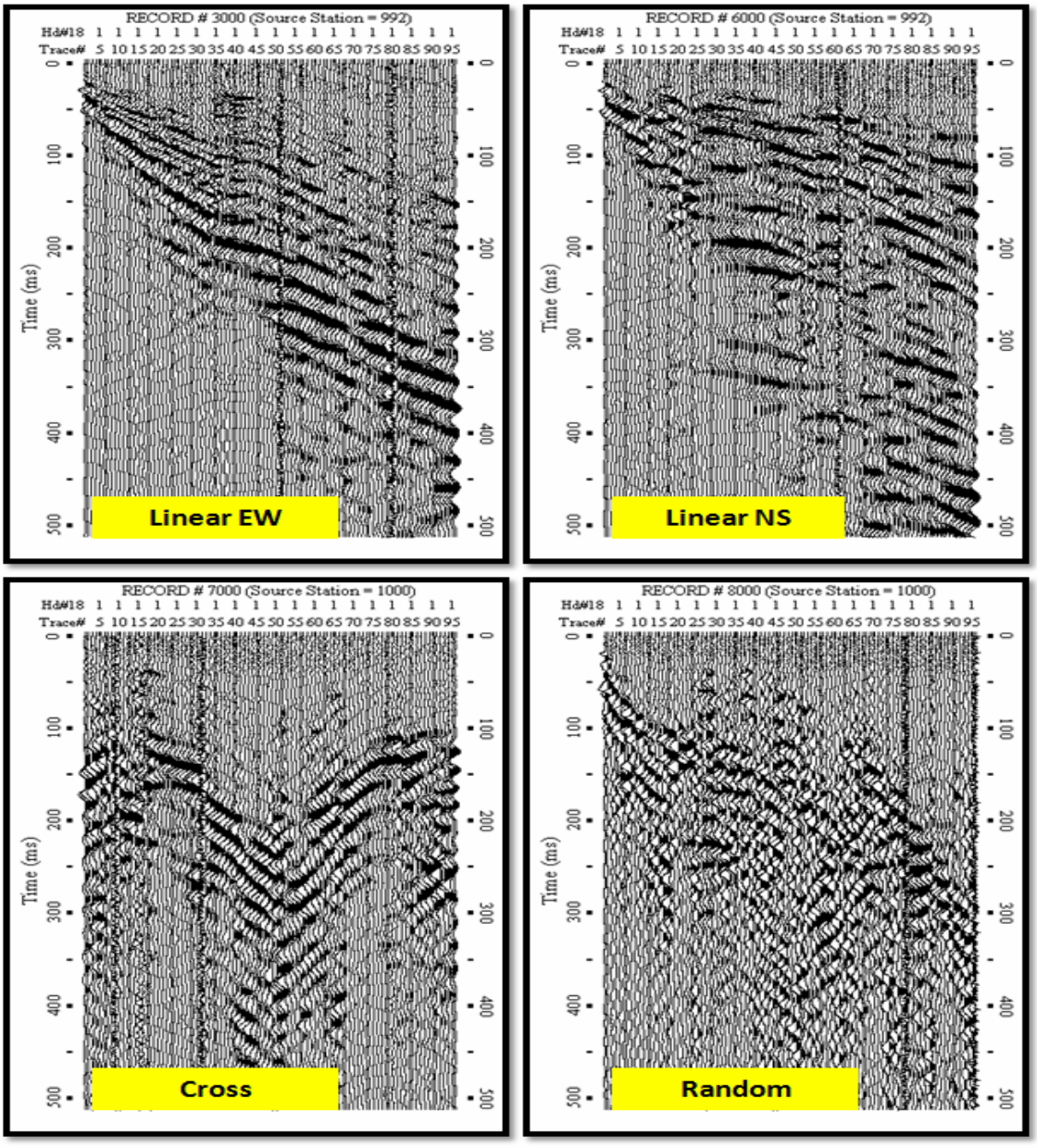


Figure 47. Typical shot gathers for various array types as acquired from the BPLF field site. Data was collected for 1000 ms but only the first 500 ms data is shown here as surface waves are more prominent here.

Table 12: Summary of data acquisition parameters

Survey Type	Active	Active	Active	Active
File Name	LinearNS_MASW.dat	LinearEW_MASW.dat	Cross_MASW.dat	Random_MASW.dat
Survey purpose	1-D Vs profiling	1-D Vs profiling	1-D Vs profiling	1-D Vs profiling
Data format	SEG-2	SEG-2	SEG-2	SEG-2
Acquisition	96-channel	96-channel	96-channel	96-channel
Seismic source	Sledge hammer	Sledge hammer	Sledge hammer	Sledge hammer
Receivers	4.5 Hz	4.5 Hz	4.5 Hz	4.5 Hz
Receiver array	Linear	Linear	Cross array	Random
Array dimensions	48m	48m	48m	48 by 48 m (square)
Receiver spacing	0.5 m	0.5 m	1 m	Random
Source offset	5m	5m	10 m around the grid	10 m around the grid
Sampling interval	0.5 ms	0.5 ms	0.5 ms	0.5 m
Recording time	1000 ms	1000 ms	1000 ms	1000 ms
Record numbers	6000-6015	3000-3015	7000-7008	8000-8008

8.4.2 Data analysis-Dispersion

The acquired data is then processed using SURFSEIS software (developed by Kansas Geologic Survey), which is done mainly in three steps: The first step involves converting the acquired SEG-2 standard data into KGS format. This process is also known as pre-processing in which the raw data in SEG-2 format is converted to the KGS format. After that the data was sorted by applying field geometry to data based on source and geophone locations. The second step involves converting the data from time-domain (Time-Distance) to frequency-domain (Frequency-Phase velocity) using Fourier transforms in which process dispersion curves are generated. The third and final step involves the inversion of surface wave data in order to obtain a 1-D shear wave velocity profile. **Figure 48** represents typical dispersion curves obtained during data processing and the fundamental modes (represented in white dots) that were picked manually as accurately as possible during the process. Dispersion analysis shows that the data

posses dominant frequencies at approximately 15-90 Hz with 0.5 Hz increment and dominant phase velocities at approximately 100-3000 m/s with 10 m/s increment. **Figure 50** represents a graph comparing dispersion curves for different array types. It is observed from the graph how well the dispersion curves correlate with one another, especially at higher frequencies (25-90 Hz).

8.4.3 Data Analysis-Inversion

In the final step of data processing, the dispersion curves are inverted to obtain 1-D shear wave velocity profiles (**Figure 49**). The profiles are calculated using an iterative inversion process requiring the dispersion data as input. The process is automated by using least-squares approach (Xia et al., 1999). In this iteration process, parameters such as Poisson's ratio, density, and thickness of the model are kept constant but only Vs is updated after each iteration. These velocities versus depth profiles generally produce a profile column consisting of ten distinct velocity layers for the site. **Figure 51** is a graph representing shear wave velocities versus depth comparisons for each array type. It is observed that there is a good correlation between Vs values for the array types. The velocities thus obtained are further used to interpret the subsurface geology structure. Also **Figure 52** shows the 1-D shear wave velocity (Vs) profiles obtained from all four arrays on one single graph. It can be observed from the combined graph that starting from surface until 2.5 m depth, there is certain amount of variation within the arrays which might be due to shallow lateral subsurface variations.

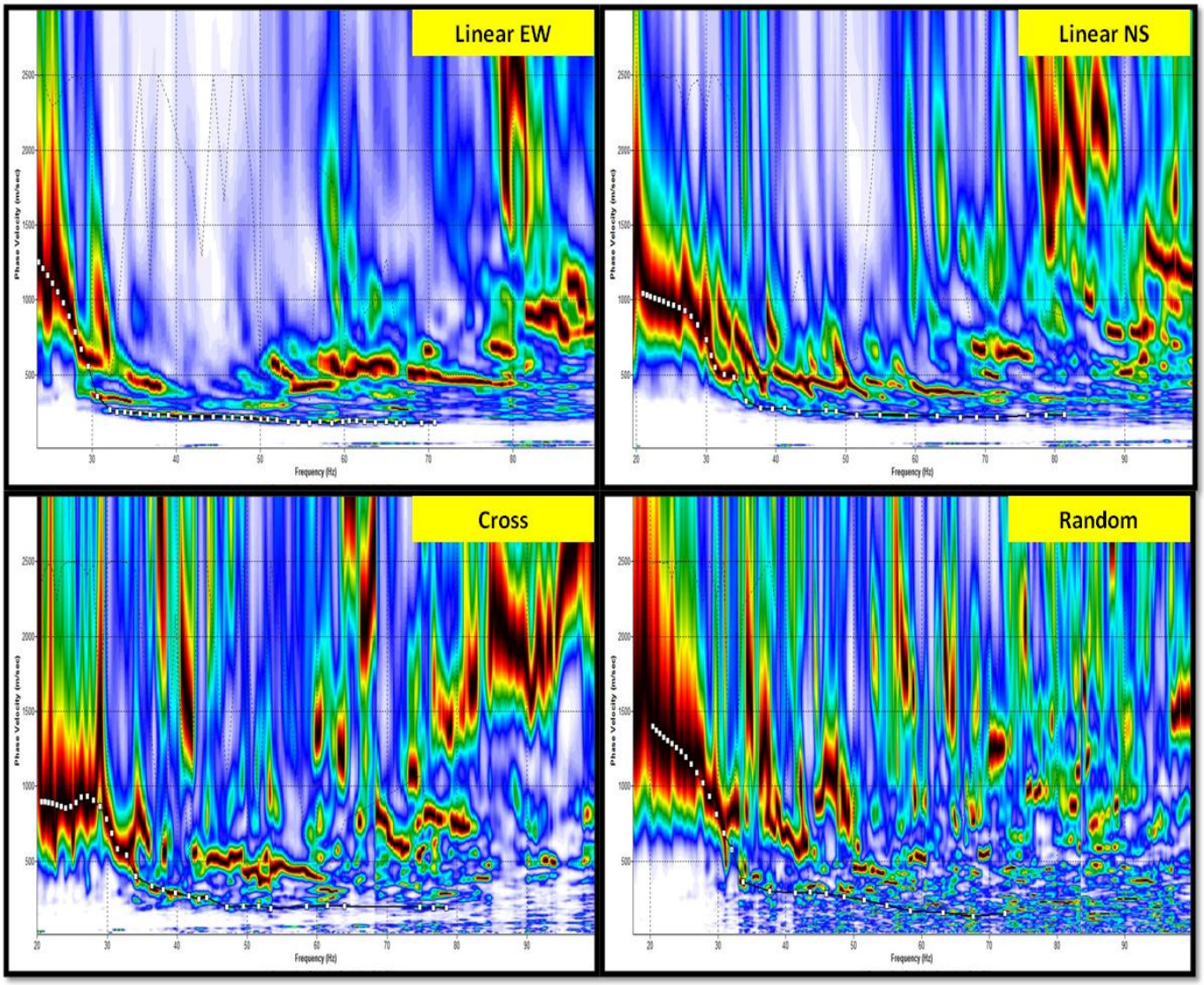


Figure 48. Dispersion images obtained from shot gathers for various receiver arrays in Figure 8.3. The x-axis represents the frequency (Hz) and y-axis represents the phase velocity (m/s). The white dots on the dispersion image represent the fundamental mode picks for various receiver arrays.

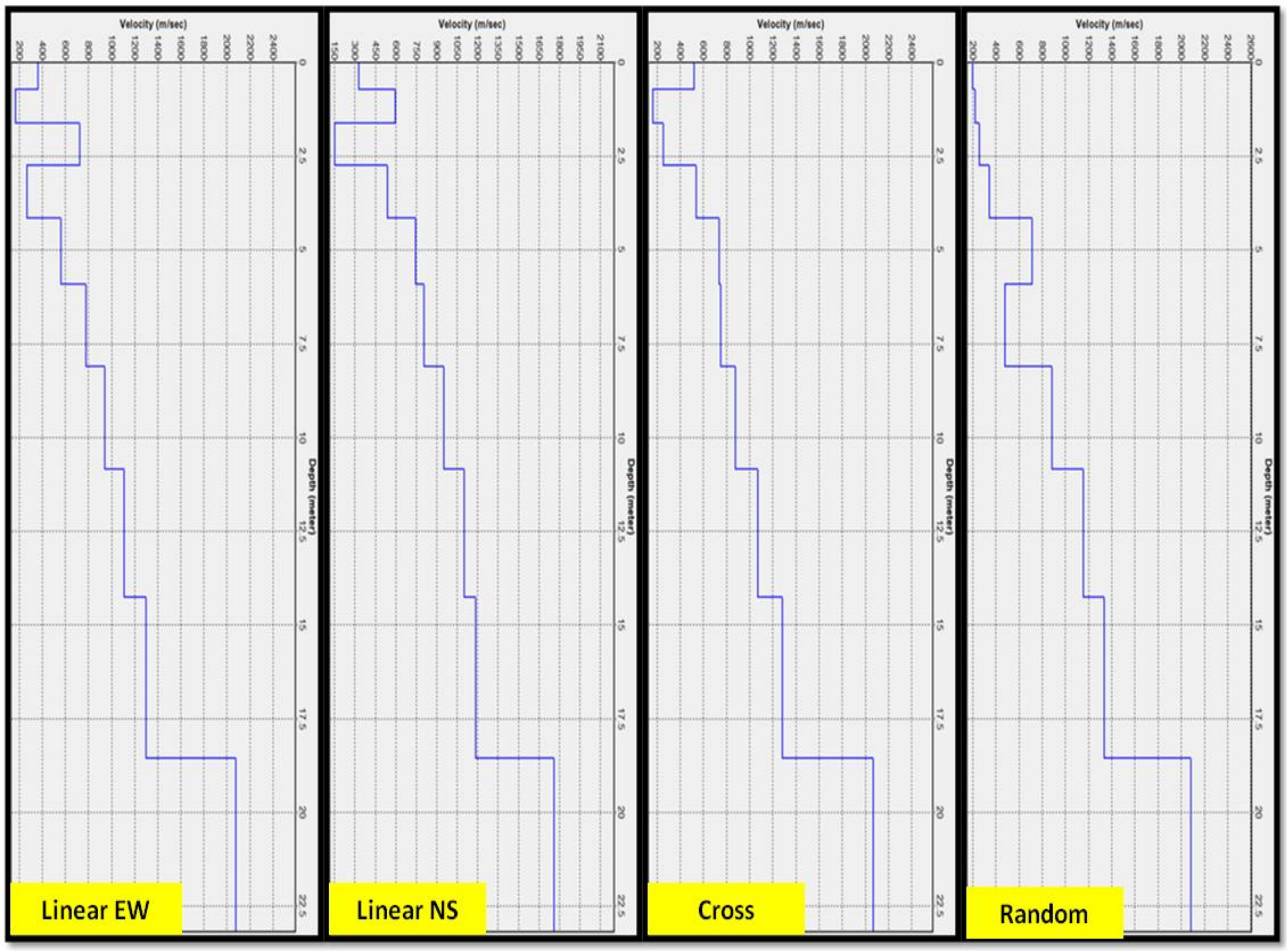


Figure 49. The 1-D shear wave velocity profiles obtained from the dispersion curves extracted from the dispersion images in Figure 8.4. The x-axis represents the shear wave velocity (m/s) and the y-axis represents the depth (m).

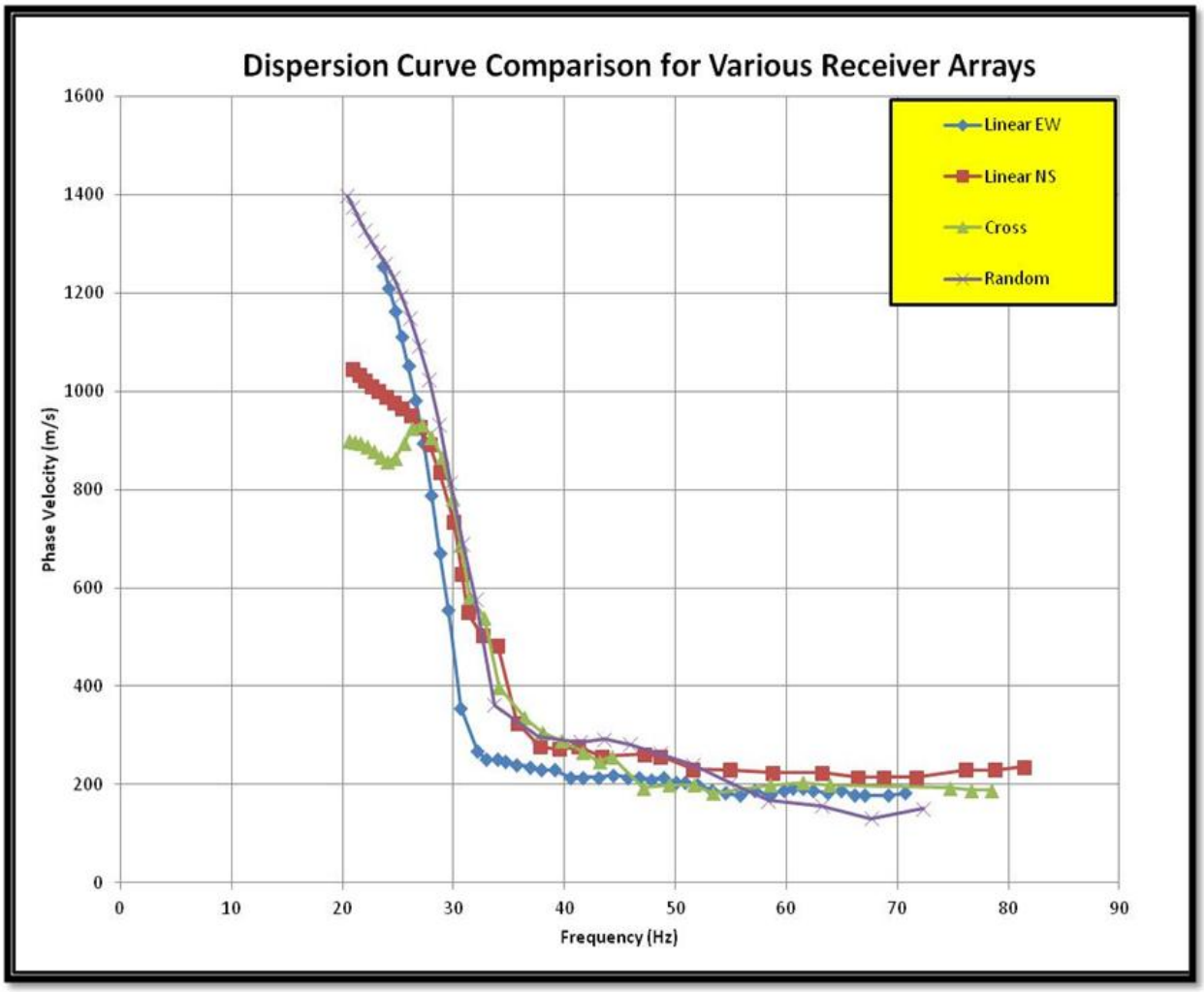


Figure 50. A graph comparing dispersion curves for various receiver arrays. The X-axis represents frequency (Hz) and Y-axis represents phase velocity (m/s).

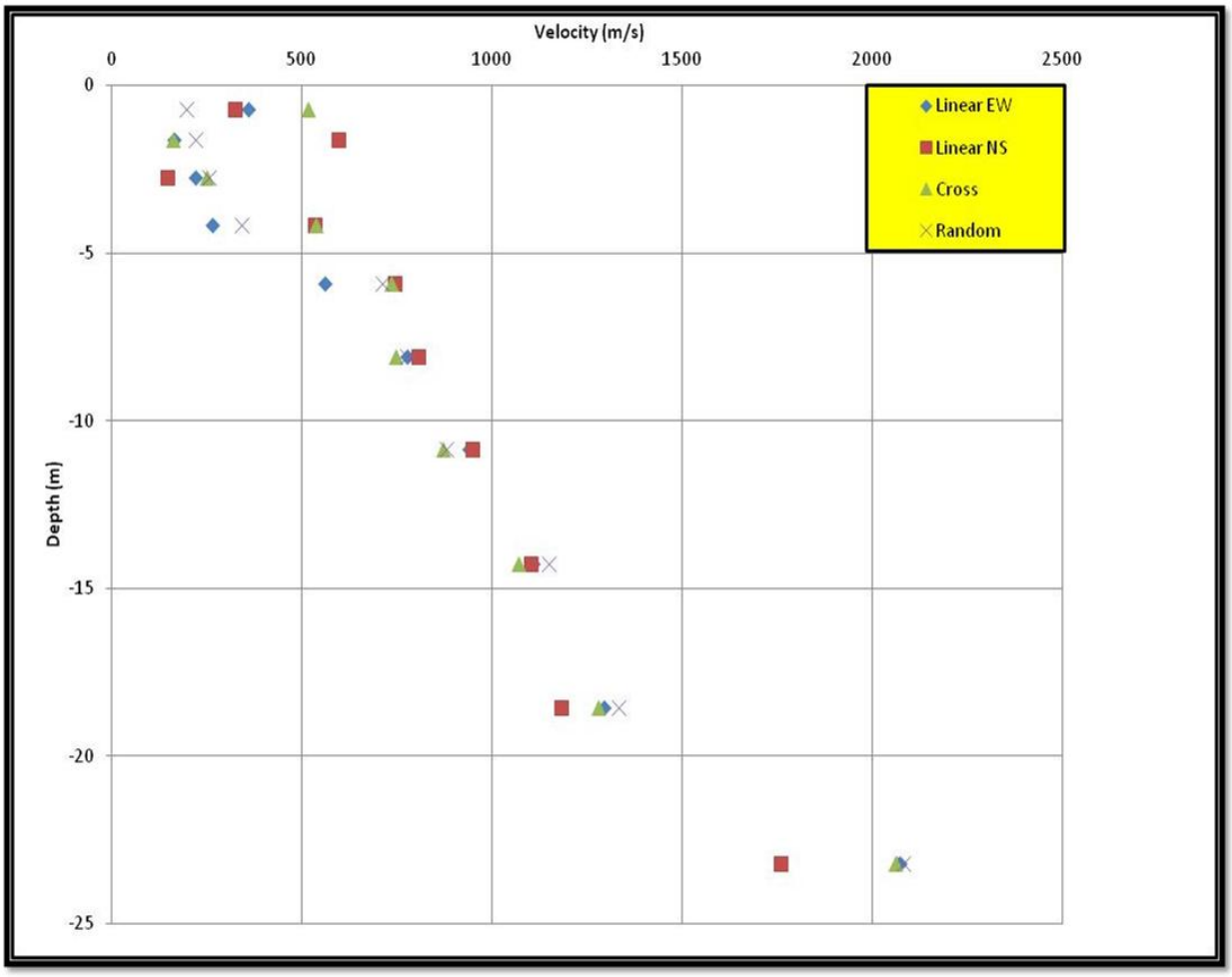


Figure 51. Velocity (m/s) versus depth (m) comparison for various receiver arrays. The X-axis represents shear wave velocity (m/s) and Y-axis represents depth (m).

8.4.4 Data Interpretation

The shear wave velocities along each survey line for each type of array are evaluated based on dispersion picks shown in **Figure 48**. A soil profile is created describing each layer (for upper 20m) based on shear wave velocity for each layers. **Figure 53** shows that on an average the shear wave velocities varies from 200 m/s to 2000 m/s for a linear array, 500 m/s to 2000 m/s for cross array, and 400 m/s to 2000 m/s for random array for up to a depth of 20m from ground level. It is observed from the obtained Vs values that there is a significant variation in soil types from ground level to 20m deep. And it is also apparent from the dispersion images that soil

thickness changes significantly even within a relatively narrow area. Since the dispersion image of the fundamental mode looks different in all kinds of arrays it may be inferred that the soil thickness below each array type may be different.

The top layer consists of very stiff soil having a velocity range of 250 m/s from 0 to 4 m deep. The geologic map of Arizona identifies this material to be Holocene to middle Pliocene basaltic rocks. Primary rock type found here is alkaline basalt that is mostly dark-colored basaltic lava and cinders young enough that some original volcanic landforms are still apparent. It includes basalt as the secondary rock type along with small amounts of andesite, dacite, and rhyolite. A layer of very dense soil with a velocity of 700m/s is found to be the second layer which extends up to a depth of 6m. The third layer is interpreted to be rocky material having a velocity ranging around 1000 m/s found at a depth ranging from 6 to 8 m. It is also observed that in this particular location, the hard rock (Vs > 2000 m/s) is found starting at a depth of 8 m and extending all the way up to 20 m. I interpreted this range to be the approximate depth to bedrock in that area.

Although more information from geotechnical borings are needed to better constrain the geologic units at various depths and also depth to bedrock, the estimated depth to bedrock map published by Arizona Geological Survey suggests that the approximate depth to bedrock at this site ranges anywhere between 5-15 m. The geologic unit associated with the bedrock at this site is the tertiary volcanic and sedimentary rocks.

The dynamic properties like the shear modulus and Poisson's ratio for the linear and random receiver arrays are calculated based on the shear wave velocity profiles and are tabulated in **Table 13**. From **Table 13**, it is observed that the shear modulus varies from 137 MN/ m^2 to 12800 MN/m^2 for linear array, and from 86 MN/ m^2 to 13000 MN/ m^2 for random. It is once

again observed here of how well these values correlate with each other for the conventional linear and newly developed random arrays.

8.5 CONCLUSIONS

This paper presents the MASW method, surveying and its application to a lunar analogue field site. It can be concluded from this study that random MASW method can be used effectively to measure the shear wave velocities and calculations of dynamic properties of materials on a lunar analog site. It is also concluded that random geophone arrangement yields results that are comparable with conventional arrays. This method can further be used in places that are inaccessible, in slopes, embankments etc. The dynamic properties thus measured using random array MASW can be used for structural design under various types of loading conditions.

Table 13. Dynamic properties of soil layers with depth at BPLF site measured using MASW method

Array type	Depth (m)	Vs (m/s)	Density (g/cc)	Shear Modulus (MN/m2)	Poisson ratio
Linear	0-2	261	2.0	137	0.30
	2.0-4.0	242	2.0	117	0.30
	4.0-6.0	668	2.0	893	0.30
	6.0-8.0	1114	2.0	2481	0.30
	8.0-20	2070	3.0	12855	0.30
Array type	Depth (m)	Vs (m/s)	Density (g/cc)	Shear Modulus (MN/m2)	Poisson ratio
Random	0-2	208	2.0	86	0.30
	2.0-4.0	299	2.0	179	0.30
	4.0-6.0	743	2.0	1104	0.30
	6.0-8.0	1122	2.0	2516	0.30
	8.0-20	2082	3.0	13004	0.30

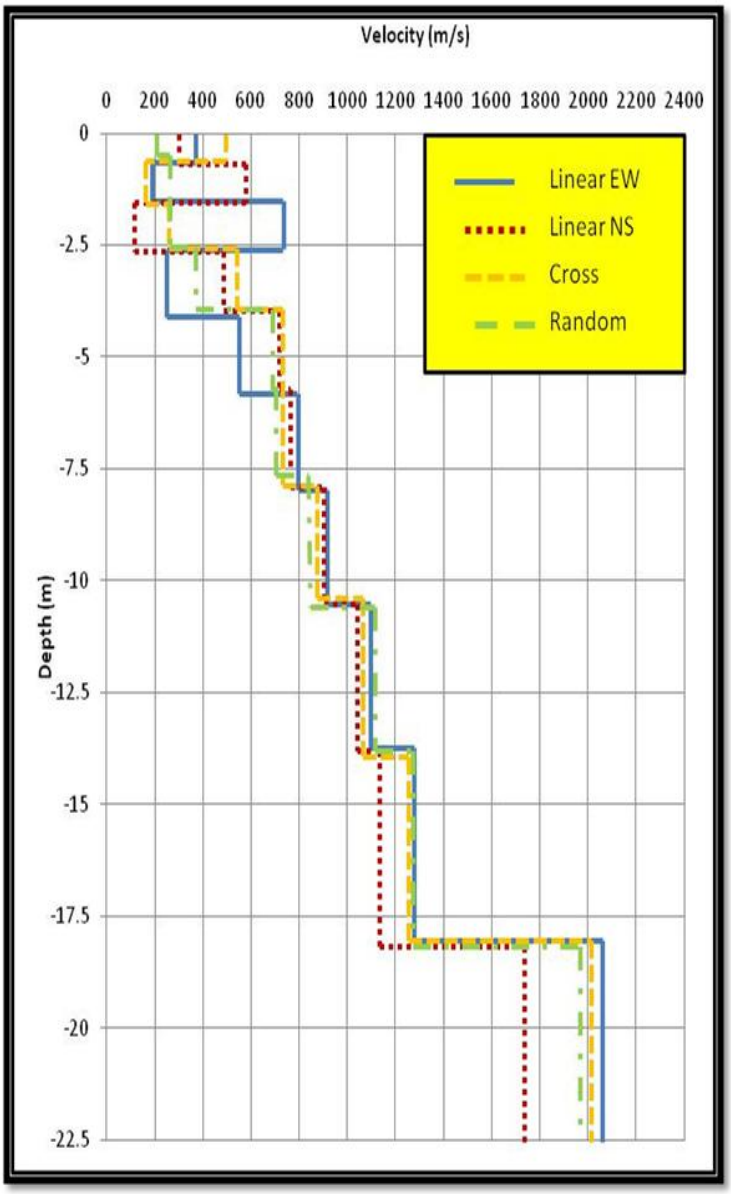


Figure 52. Graphical representation of Vs profiles for all receiver array types shown together in a single graph.

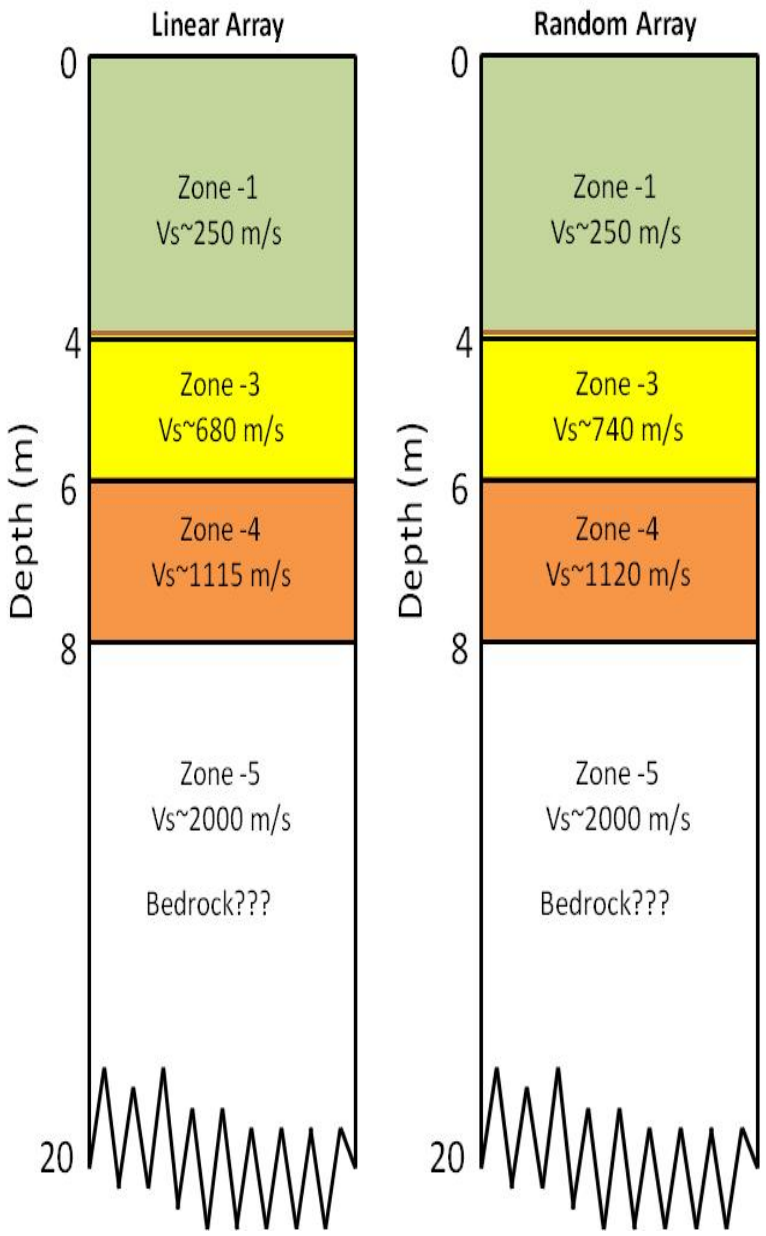


Figure 53. Interpreted soil profile as estimated for the conventional linear array and newly developed random array for up to 20 m depth.

Chapter 9

Summary, Conclusions and Future Work

9.1 SUMMARY AND CONCLUSIONS

This dissertation research introduces a new technique of using random arrangement of geophones instead of conventional arrays to delineate geotechnical properties within the upper 30 m of the subsurface using Multichannel Analysis of Surface Wave (MASW) technique. Such kind of arrangement (likely deployed from a mortar-type device) instead of a conventional linear array is found to be necessary for lunar exploration because of the logistical constraints involved in deploying a linear or circular array robotically or by astronaut. The main underlying concept behind this study is that based on the extreme logistics imposed by lunar exploration and the anticipated engineering needs of lunar exploration, information obtained on the moon using this technique should prove to be a critical component of data acquisition.

The dissertation contains several individual studies that are all intertwined by a common application of random geophone array to determine subsurface variations in physical properties that is hypothesized will be critical for future lunar explorations as they characterize the mechanical behavior of geotechnical materials under various types of loading. The introductory chapters include extensive research on surface wave theory, overall MASW procedure, and physical properties of the moon known till date. Followed by the introductory chapters (2,3, and 4), the fifth chapter introduces the random array concept for delineating subsurface properties within the upper 30 m. The sixth chapter then covers the comparison of the newly developed array with that of the conventional arrays to determine the accuracy of the random array. The seventh chapter covers some modeling experiments conducted to determine some key acquisition parameters pertaining to random array MASW survey. Finally, the eighth chapter covers the application of random array MASW method in determining dynamic properties of subsurface

within the upper 30m at a lunar analog site. Some of the preliminary results and conclusions of the four chapters are briefly summarized, and the overall impact and overarching implications of this research are presented.

9.1.1 Random Array Analysis

A new configuration of randomly-distributed receivers for estimating the S-wave velocity profile of subsurface soils was introduced. The experiment was performed by collecting active surface wave data at the University of Tennessee agricultural experimental field site, using random geophone arrangement. A total of 13 shot points were deployed while collecting the random data and the shot gather obtained for each shot point location was processed to study the azimuthal variations in the subsurface. The acquired data has been processed using SURFSEIS software, for dispersion curve extraction. The dispersion results obtained thus were compared to conventional linear array data that was acquired at the same location as the random data. The comparison indicates that the random array correlates fairly well with that of the linear array data. Some variations pertaining to the dispersion data were observed in the random data that could be due to azimuthal variations in the subsurface. Statistical analyses were performed on the data to study the variability in the range of velocity values within the grid. It was concluded that the variations in the velocity values may be due to the variations in the lithology of the subsurface. It is thus concluded from this study that random array MASW method can be used to obtain reliable dispersion images and thus 1-D shear wave velocity profiles that are comparable to conventional linear array and it can further be used to map subsurface geology to an acceptable level.

9.1.2 Comparison of Various Geophone Arrays

This study is mainly performed to compare the newly developed random array with four different types of MASW geophone arrays (Linear EW, Linear NS, cross and circular). For this, more active surface wave data were collected at the same site and location using different array configurations. All the data thus acquired were processed using SURFSEIS software and dispersion curves were extracted for each array type. The dispersion picks were further inverted to obtain 1-D shear wave velocity profiles which were used for comparison. Performed investigations have shown that they are all quite effective in determining shallow shear-wave velocity profiles and that the results obtained from random array are comparable with that of the conventional arrays. The depth to the bedrock could be successfully identified from the random array data. In order to further evaluate random array, four different random sets were collected each with different X and Y coordinates and it is observed that the more dispersive the geophones are in a random array, the better the resolution of the dispersion image, and thus the 1-D Vs interpretations. It can be concluded thus from the comparison of various receiver arrays, the estimated bedrock depths and proximal ground truth, that the interpretation of the 1-D MASW shear-wave velocity profiles from different array types is reasonably reliable and the random array profiles are quite comparable with that of the conventional to an acceptable level. The implication is that the dispersion curves from various conventional and random receiver arrays are also reliable. Therefore, it can safely be concluded from this study that random arrangement of geophones can be used to determine the geotechnical properties of the subsurface and are more advantageous than conventional arrays.

9.1.3 Forward-Modeling Experiments

Influence of random geophone array on the resolution of dispersion curve using forward modeling method in multichannel analysis of surface wave (MASW) surveys is described here on a theoretical perspective of the dispersion curve imaging method used during a normal implementation of MASW method. Parameters like clustered geophones, skewness of receivers, different receiver numbers, total number of traces and their influence on dispersion image are described in this study. It was concluded based on the modeling results that in order to obtain best dispersion data from a random array MASW survey the geophones a) should be as dispersive (less clustered) as possible, b) should be normally skewed around the grid (although right or left skewed data also yield reliable dispersion images, a normally skewed data yields high λ_{max}, which in turn gives more depth of penetration, and c) A higher number of traces results in high resolution dispersion image, however it is only necessary to increase the number of traces only if you are increasing the area of coverage.

9.1.4 Application of Random Array MASW

This study presents the MASW method, surveying and its application to a lunar analog field site. To achieve this goal, MASW data was collected at the Black Point Lava flow site (BPLF), Flagstaff, Arizona. The data was collected for four different geophone arrays (linear EW, Linear NS, cross, and random). The data was processed for dispersion curves which were in turn used to obtain the shear wave velocity profiles of the subsurface. The dynamic properties like the shear modulus and Poisson's ratio were calculated based on the shear wave velocity profiles for linear and random arrays and it was observed that the values correlate very well for the conventional linear and newly developed random array. It can thus be concluded from this

study that random MASW method can be used effectively to measure the shear wave velocities and calculations of dynamic properties of materials on a lunar analog site. The dynamic properties thus measured using random array MASW can be used for structural design under various types of loading conditions.

9.2 OVERALL CONCLUSIONS AND IMPLICATION OF RESEARCH

The overall theme of the research presented herein is that systematic use of random array MASW method is a viable technique for determining engineering properties of the subsurface within the upper 30 m. Although conventional array types have proven adept for delineating soil properties, the type of array that you choose is at least partially controlled by the site viability and other conditions. Thus, in some cases like the lunar surfaces, where there might be places that can be unreachable or it is simply not possible to arrange a systematic linear or circular array robotically (or by an astronaut) on the surface due to logistical reasons, a randomly distributed geophone array (likely to be deployed using a mortar-type device) will be most useful. Additionally there is information that can be obtained from random array like the azimuthal variations in the subsurface that are likewise difficult to determine using other geophone arrangements.

The random array MASW method is a novel approach, and provides reliable subsurface information that is comparable to the conventional arrays. The geotechnical properties obtained from this new technique can further be used in places that are inaccessible, in slopes, embankments etc.

\

9.3 FUTURE WORK

There are a number of additional investigative components—not conducted within the scope of this project—which could be expanded for future projects.

1. Further evaluation of random array can be performed in terms of dispersion curve analysis. Data can be collected with much larger grid dimensions using more number of geophones (of lower frequency) to see if we can obtain much deeper depth information. Also analysis of errors associated with dispersion picks or any other kind of computational artifacts during data acquisition or processing stage can be further evaluated by collecting more number of random arrays. Collecting random array data using passive sources (like traffic noise or wind) and then combining both active and passive data might result in much better dispersion analysis as in theory active data provides information at higher frequencies and passive data covers the lower part of frequencies in a dispersion image. Therefore looking at combined results would provide us more information about subsurface features.
2. Based on the modeling results effort can be made to collect real field data in order to study the effect of clustered array, skewness effect etc. Also further models can be generated to study the effect of passive source on random array data, or to analyze more on other offset related parameters like source-offset distance, receiver spacing, total length of the array, etc.
3. Apply the newly developed methodology to additional lunar analog sites and in other inaccessible areas like urban areas where in it is difficult to deploy a linear or circular array for further refining the methodology proposed in this research. And hopefully, this method can be applied on the moon and other planetary bodies during future missions.

REFERENCES

Abo-Zena, A.M. (1979). "Dispersion function computations for unlimited frequency values." Geophys. J. R. Astr. Soc., 58, 91-105.

Achenbach, J.D. (1973). Wave propagation in elastic solids, North-Holland, 425p.

Aki, K. (1965). A note on the use of microseismics in determining the shallow structures of the Earth's crust: *Geophysics*, *Vol 30, 665-666*

Aki, K., and Richards, P.G. (1980). Quantitative Seismology-Theory and Methods, Vol.1 and 2, Freeman Company, San Fransisco, 932p.

Aki, K., and Richards, P.G., 1980, Quantitative seismology:W.H. Freeman & Co. Mari, J. L., 1984, Estimation of static correction for shear-wave profilingusing the dispersion properties of Love waves: Geophysics, 49, 1169–1179.

Al-Hunaidi, M.O., and Rainer, J.H., 1995, Analysis of multi-mode signals of the SASW method, Proc 7th Int. Conf. Soil Dynamics and Earthquake Eng., p. 259-266.

Aouad, M.F., 1993, Evaluation of Flexible Pavements and Subgrades Using the Spectral-Analysis-of-Surface-Waves (SASW) Method, PhD thesis, Univ. of Texas at Austin, Texas.

About Analog Missions and Filed Tests. (2011). Retrieved June 11, 2012, from http://www.nasa.gov/exploration/analogs/about.html .

About NASA Desert-RATS program (news and features blog). (2012). Retrieved on June 11, 2012, from http://www.nasa.gov/exploration/analogs/desert_rats.html.

Arizona's Black Point Lava Flow Beckons NASA's Desert Rats. (2010). Retrieved on August 24, 2010, from http://spacecoalition.com/uncategorized/arizonas-black-point-lava-flow-beckons-nasas-desert-rats?doing_wp_cron.

Babuska, V., and Cara, M., (1991). Seismic anisotropy in the earth: Kluwer Academic Publishers.

Baker, G.S., Steeples, D.W., Schmeisner, C., 1999. In situ, high-resolution P-wave velocity measurements within 1 m of the Earth's surface: Geophysics, **64**, no 2, 323-325

Baker, G.S., Steeples, D.W., and Schmeissner, C, 2002, The effect of seasonal soil-moisture conditions on near-surface seismic reflection data quality: *First Break, 20,* no 1, 35-41

Bates R. L. and Jackson J. A., eds. (1980) The Glossary of Geology, 2nd Edition. American Geological Institute, Washington. 751 pp.

Bekker M. G. (1969) *Introduction to Terrain—Vehicle Systems*. Univ. of Michigan, Ann Arbor.

Bishop A. W. (1955) The use of the slip circle in the stability analysis of earth slopes. *Geotechnique, 5,* 7–17.

Bolt, B.A. (1993). Earthquakes, W.H.Freeman, New York, 331p.

Bullen, K.E. (1963). An introduction to the theory of Seismology: *Cambridge Univ. Press*.

Butler J. C. and King E. A. (1974) Analysis of grain size frequency distributions of lunar fines. *Proc. Lunar Sci. Conf.5th,* pp. 829–841.

Black Point Lava Flow, Arizona (Image). (2009). Retrieved on September 7, 2009, from http://earthobservatory.nasa.gov/IOTD/view.php?id=40076 .

Cadigan, R.A, 1962, A method for determining the randomness of regionally distributed quantitative geologic data: *Journal of sedimentary Petrology*, 32, 813-818.

Carrier W. D. III (1973) Lunar soil grain size distribution. *The Moon, 6,* 250–263.

Carrier W. D. III, Johnson S. W., Carrasco L. H., and Schmidt R. (1972a) Core sample depth relationships: Apollo 14 and 15. *Proc. Lunar Sci. Conf. 3rd,* pp. 3213–3221.

Carrier W. D. III, Bromwell L. G., and Martin R. T. (1972b) Strength and compressibility of returned lunar soil. *Proc. Lunar Sci. Conf. 3rd,* pp. 3223–3234.

Carrier, W.D., Olhoeft, G.R., and Mendell, W., 1991, Physical Properties of the Lunar Surface, Lunar Sourcebook, Heiken, G., Vaniman, D., and French, B.M, eds., Cambridge University Press, 475-594.

Cherkasov I. I., Vakhnin V. M., Kemurjian A. L., Mikhailov L. N., Mikheyev V. V., Misatov A. A., Smorodinov M. A., and Shvarev V. V. (1968) Determination *of* the physical and mechanical properties *of* the lunar surface layer by means *of* Luna 13 automatic station. In *Moon and Planets II* (A. Dollfus, ed.), pp. 70–76. North-Holland, Amsterdam.

Christensen E. M., Batterson S. A., Benson H. E., Chandler C. E., Jones R. H., Scott R. F., Shipely E. N., Sperling F. B., and Sutton G. H. (1967) Lunar surface mechanical properties—Surveyor 1. *J. Geophys. Res., 72,* 801–813.

Choate R., Batterson S. A., Christensen E. M., Hutton R. E., Jaffe L. D., Jones R. H., Ko H. Y., Scott R. F., Spencer R. L., Sperling F. B., and Sutton G. H. (1968) Lunar surface mechanical properties. In *Surveyor Project. Part 1: Project Description and Performance,* pp. 137–194. JPL Tech. Rpt. 32–1265, Jet Propulsion Laboratory, Pasadena.

Croft S. K. (1980) Cratering flow field: Implications for the excavation and transient expansion stages of crater formation. *Proc. Lunar Planet. Sci. Conf. 11th,* pp. 2347– 2378.

Dobrin, M.B., Savit, C.H. (1988). Introduction to Geophysical Prospecting.

Dorman, J., and Ewing, M., 1962, Numerical inversion of seismic surface wave dispersion data and crust-mantle structure in the New York–Pennsylvania area: J. Geophys. Res., 67, 5227, 5241.

Ewing, W. M., Jardetzky, W. S., and Press, F. (1957). *Elastic waves in layered media* McGraw-Hill, New York. 380p.

Folk R. L. (1968) *Petrology of Sedimentary Rocks.* Hemphill's, Austin. 170 pp.

Fonquinos Mera, R., 1995, Dynamic nondestructive testing of pavements, PhD thesis, Univ. of Texas at Austin, Texas.

Foti, S., 2000, Multistation methods for geotechnical characterization using surface waves: PhD thesis, Politecnico di Torino, Italy.

Gabriels, P., Snider, R., and Nolet, G., 1987, In situ measurements of shear-wave velocity in sediments with higher-mode Rayleigh waves: Geophys. Prospecting, 35, 187-196.

Ganji, V., Gucunski, N., and Nazarian, S., 1998, Automated inversion procedure for spectral analysis of surface waves, J. Geotech. Engrg., ASCE, v. 124, n. 8, p. 757-770.

Gehrels T., ed. (1979) *Asteroids.* Univ. of Arizona, Tucson. 1181 pp.

Graff, K.F. (1975). Wave motio in elastic solids, Dover Publications, New York, 649p.

Grant, H., David, V., and Bevan, M.F (1991): Lunar source book, a user's guide to the moon: *Cambridge Univ. Press*.

Gucunski, N., and Woods, R.D., 1992, Numerical simulation of the SASW test, Soil Dyn and Earth-quake Engrg. J., v. 11, n. 4, p. 213-227.

Halajian J. D. (1964) *The Case for a Cohesive Lunar SurfaceModel.* Grumman Research Dept. Report ADR 04–40–64.2,Grumman Aircraft Engineering Corp., Bethpage, New York.

Haskell, N. A. 1953, The dispersion of surface waves on multilayered media, *Bull. Seismological Soc. of Am., v. 43, n. 1, p. 17-34.*

Haskell, N.A. (1953). "The dispersion of surface waves in multilayered media.' Bulletin of the Seismological Society of America,43, 17-34.

Heiken G. (1975) Petrology of lunar soils. *Rev. Geophys. Space Phys.,* 13, 567–587.

Heisey, J.S., Stokoe II, K.H., and Meyer, A.H., 1982, Moduli of pavement systems from Spectral Analysis of Surface Waves, Transp. Res. Rec., v. 852, Washington D.C, p. 22-31.

Hilterman, F, 1990, Is AVO the seismic signature of lithology? A case history of ship Shoal South Addition: *The Leading Edge*, 9(6), 15-22.

Hiltunen, D.R., and Gucunski, N., 1994, Annotated bibliography on SASW, in Geophysical character-ization of sites, ISSMFE Technical Committee #10, edited by R.D. Woods, Oxford Publishers, New Delhi.

Hisada, Y. (1994). "An efficient method for computing Green's functions for a layered half-space with sources and receivers at close depths." *Bulletin of the Seismological Society of America*, 84(5), 1456-1472.

Hisada, Y. (1995). "An efficient method for computing Green's functions for a layered half-space with sources and receivers at close depths (Part 2)." *Bulletin of the Seismological Society of America*, 85(4), 1080-1093.

Horz, Friedrich., Grieve, RR., Heiken, G., Spudis, P., and Binder, A. (1991): Lunar Surface Processes, *Lunar Source book., Cambridge University Press, Cambridge, pp. 61-120*.

Houston W. N., Moriwaki Y., and Chang C.-S. (1973) Downslope movement of lunar soil and rock caused by meteoroid impact. *Proc. Lunar Sci. Conf. 4th,* pp. 2425– 2435.

Houston W. N. and Mitchell J. K. (1971) Lunar core tube sampling. *Proc. Lunar Sci. Conf. 2nd,* pp. 1953–1958.

Hudson, J.A., 1980, Overall properties of a cracked soild: Math. Proc. Camb. Phil. Soc., 88, 371 384.

Ivanov, J., Park, C.B., Miller, R.D., and Xia, J., 2000a, Mapping Poisson's Ratio of unconsolidated materials from a joint analysis of surface-wave and refraction events: Proceedings of the Symposium on the Application of Geophysics to Engineering and Environmental Problems, Arlington, Va.,February 20-24, 2000

Jaffe L. D. (1964) Depth and strength of lunar dust. *Eos Trans. AGU, 45,* 628.Jaffe L. D. (1965) Strength of the lunar dust. *J. Geophys.Res., 70,* 6139–6146.

Jones, R., 1955, A vibration method for measuring the thickness of concrete road slabs in situ, Magazine of Concrete Research, v. 7, n. 20, p. 97-102.

Jones, R., 1962, Surface wave technique for measuring the elastic properties and thickness of roads: Theoretical development, British Journal of Applied Physics, v.13, p. 21-29.

Jones, R.B. (1958). "In-situ measurement of the dynamic properties of soil by vibration methods." Geotechnique, 8(1), 1-21.

Joel, S.W., (1966): Investigation of *in situ* Physical Properties of Surface and Subsurface Site Materials by Engineering Geophysical Techniques, Annual Report, Retrieved on July 22, 2011,from http://ntrs.nasa.gov/archive/nasa/casi.ntrs.nasa.gov/19660028076_1966028076.pdf .

Kausel, E., and Roesset, J.M., (1981). "Stiffness matrices for layered soils." Bulletin of the Seismological Society of America, 71(6), 1743-1761.

Kennet, B. L. N. (1974). "Reflections, rays, and reverberations." *Bulletin of the Seismological Society of America*, 64, 1685-1696.

Kennet. B. L. N., and Kerry, N. J. (1979). "Seismic waves in a stratified half space." *Geophysical J. Royal Astronomical Society*, 57, 557-583.

Khan, A., Connolly, J.A.D., Maclennan, J., and Mosegaard, K, 2007, Joint inversion of seismic and gravity data for lunar composition and thermal state: *Geophysical Journal International*, **168**, 243-58.

Khan, A., Mosegaard, K and Rasmussen, K.L (2000): A new seismic velocity model for the moon from a Monte Carlo inversion of the Apollo Lunar seismic data: *Geophysical Research Letters, Vol 27, No.11, 1591-1594*

Khan, A., Mosegaard, K., and Rasmussen, K.L, 2000, A new seismic velocity model for the Moon from a Monte Carlo inversion of the Apollo Lunar seismic data: *Geophysical Research Letters*, **27**, 1591-1594.

Kleine, T.; Palme, H.; Mezger, K.; Halliday, A.N. (2005). "Hf–W Chronometry of Lunar Metals and the Age and Early Differentiation of the Moon". *Science* **310** (5754): 1671–1674. Bibcode 2005Sci...310.1671K. doi:10.1126/science.1118842. PMID 16308422

Koch G. S. Jr. and Link R. F. (1970) *Statistical Analysis of Geological Data.* Wiley, New York. 75 pp.

Kuiper, G.P., ed., 1960, Photographic Lunar Atlas: University of Chicago.

Lai, C.G. (1998). Simultaneous inversion of Rayleigh phase velocity and attenuation for near-surface site characterization, PhD dissertation, Georgia Institute of Technology, 370p.

Lambe T. W. and Whitman R. V. (1969) *Soil Mechanics.* Wiley, New York. 553 pp.

Langevin Y. (1982) Evolution of an asteroidal regolith: Granulometry, mixing and maturity. In *Workshop on LunarBreccias and Soils and Their Meteoritic Analogs* (G. J. Taylor and L. L. Wilkening, eds.), pp. 87–93. LPI Tech. Rpt. 82–02,Lunar and Planetary Institute, Houston.

Leonovich A. K., Gromov V. V., Dmitriyev A. D., Penetrigov V. N., Semenov P. S., and Shvarev V. V. (1974a) The main peculiarities of the processes of the deformation and destruction of lunar soil. In *The Soviet American Conference on Cosmochemistry of the Moon and Planets,* pp. 735–743. NASA SP-370 (1977); also available in NASA Technical Translation F-16034 (1974)

Leonovich A. K., Gromov V. V., Semyonov P. S., Penetrigov V. N., and Shvartov V.V. (1975) Luna 16 and 20 investigations of the physical and mechanical properties of lunar soil. In *COSPAR Space Research XV,* pp. 607–616. Akademie-Verlag, Berlin

Lucey, P., Randy, L.K., Jeffrey, J.G., Larry, A.T., et.al., (2005): Understanding the Lunar surface and space-moon interactions*, Review in mineralogy and geochemistr, Vol.60, 83-219.*

Luco, J. E. and Apsel, R. J. (1983). "On the Green's function for a layered half-space." Part I*, Bulletin of the Seismological Society of America*, 73, 909-929.

Mahmood A., Mitchell J. K., and Carrier W. D. III (1974a) Grain orientation in lunar soil. *Proc. Lunar Sci. Conf. 5th,* pp. 2347–2354.

Martin R. T., Winkler J. L., Johnson S. W., and Carrier W. D. III (1973) Measurement of conductance of Apollo 12 lunar simulant taken in the molecular flow range for helium, argon, and krypton gases. Unpublished report.

Martincek, G., 1994, Dynamics of pavement structures, E & FN Spon and Ister Science Press, Slovak Republic.

Maxwell D. E. (1977) Simple Z model of cratering, ejection and the overturned flap. In *Impact and Explosion Cratering* (D. J. Roddy, R. O. Pepin, and R. B. Merrill, eds.), pp. 1003–1008. Pergamon, New York.

Mckay D.S., Fruland .M., and Heiken G.H.(1974) Grain size and evolution of lunar soils. Proc. Lunar Sci. Conf. 5th, pp. 887-906.

Mckay D.S., Heiken G.H., Basu A., Blanford G., Simon S., Reedy R., French B.M., and Papike J. (991). Lunar Sourcebook, a user's guide to the moon. New York: Cambridge University Press. P.736.

McMechan, G. A., and Yedlin, M. J., 1981, Analysis of dispersive waves by wave field transformation: *Geophysics*, **46**, 869-874.

Miller, R.D., Xia, J., Park, C.B., and Ivanov, J., 1999, Multichannel analysis of surface waves to map bedrock, *The Leading Edge*, **18,** no. 12, 1392-1396.

Miller, R.D., Xia, J., Park, C.B., and Ivanov, J., 1999, Multichannel analysis of surface waves to map bedrock, The Leading Edge, 18, no. 12, 1392-1396.

Mitchell, J.K., Carrier, W.D., Costes, N.C., Houston, W.N., Scott, R.F., and Hovland, H.J., 1973, Soil Mechanics: Apollo 17 Preliminary Science Report, NASA SP-330.

Mitchell J. K., Houston W. N., Scott R. F., Costes N. C., Carrier W. D. III, and Bromwell L. G. (1972d) Mechanical proper-ties of lunar soil: Density, porosity, cohesion, and angle of friction. *Proc. Lunar Sci. Conf. 3rd,* pp. 3235–3253

Mitchell, J.K., Houston, W.N., Carrier, W.D., and Costes, N.C., 1974, Apollo Soil Mechanics Experiment S-200, Final report NASA Contract NAS 9-11266, *Space Sciences Laboratory Series* **15**, no. 7, University of California.

Mitchell J. K., Houston W. N., Carrier W. D. III, and Costes N. C. (1974) *Apollo Soil Mechanics Experiment S-200.* Final report, NASA Contract NAS 9–11266, Space Sciences Laboratory Series 15, Issue 7, Univ. of California, Berkeley.

Multichannel Analysis of Surface Waves (MASW). (2007). Retrived on May 2009 from http://www.masw.com/index.html.

Nakamura, Y., Lammelein, D., Latham, G., Ewing, M., Dorman, J., Press, F and Toksoz, N (1973): New seismic data on the state of the deep lunar interior, *Science, Vol 181, No. 4094, 49 51.*

Nakamura, Y., Lammlein, D., Latham, G., Ewing, M., Dorman, J., Press, F., and Toksoz, N., 1973, New Seismic Data on the State of the Deep Lunar Interior: *Science*, **181**, 49-51.

Nazararian, S., Stokoe II, K.H., and Hudson, W.R., 1983, Use of spectral analysis of surface waves method for determination of moduli and thickness of pavement systems: *Transportation Research Record* No. **930**, 38-45.

Nazararian, S., Stokoe II, K.H., and Hudson, W.R., 1983, Use of spectral analysis of surface waves method for determination of moduli and thickness of pavement systems: Transportation Research Record No. 930, 38-45.

Nazarian, S. (1984). Insitu determination of elastic moduli of soil deposits and pavement systems by Spectral-Analysis-of-Surface-Waves method, PhD dissertation, Uni. Of Texas of Austin. Okada, H. (2003). The microtremor survey method, SEG, 135p.

Nazarian, S., Stokoe II, K.H., and Hudson, W.R. (1983): Use of spectral analysis of surface waves method for determination of moduli and thickness of pavement systems: *Transportation Research Record No.930, 38-45*.

Neukum G., Konig B., Fechtig H., and Storzer D. (1975) Cratering in the Earth-Moon system: Consequences for age determinations by crater counting. Proc. Lunar Sci. Conf. 6th, pp. 2597–2620

O'Neill, A., 2003, Full-waveform reflectivity for modeling, inversion and appraisal of seismic surface wave dispersion in shallow site investigations, Ph.D. thesis, The University of Western Australia, Australia.

Orphal D. L. (1977) Calculations of explosive cratering—II: Cratering mechanics and phenomenology. In *Impact and Explosion Cratering* (D. J. Roddy, R. O. Pepin, and R. B. Merrill, eds.), pp. 907–918. Pergamon, New York.

Papike J. J., Simon S. B., and Laul J. C. (1982) The lunar regolith: Chemistry, mineralogy, and petrology. *Rev.Geophys. Space Phys., 20,* 761–826.

Park, C. B., Ivanov, J., Miller, R. D., Xia, J., and Ryden, N., 2001a, Multichannel analysis of surface waves (MASW) for pavement: Feasibility test: 5th SEGJ Int. Symposium, Tokyo, Japan, January 24-26, 2001.

Park, C.B., Miller, R.D., and N.Ryden, 2006, Roadside seismic survey utilizing traffic noise: *Proceedings of the NDE conference on Civil Engineering, St. Louis. MO, August 14-18, 317-324.*

Park, C.B., Miller, R.D., and Xia, J., 1998, Ground roll as a tool to image near-surface anomaly: [Expanded Abstract*]: Soc. Explor. Geophys. 874-877.*

Park, C.B., Miller, R.D., and Xia, J., 1998, Imaging dispersion curves of surface waves on multi channel record: [*Expanded Abstract*]: *Soc. Explor. Geophys*., 1377-1380.

Park, C.B., Miller, R.D., and Xia, J., 1999, Multi-channel analysis of surface waves (MASW): Geophysics, v. 64, no. 3, p. 800-808.

Park, C.B., Miller, R.D., and Xia, J., 2001, Offset and resolution of dispersion curve in multichannel analysis of surface waves (MASW): Proceedings of the SAGEEP 2001, Denver, Colorado, SSM4.

Park, C.B., Miller, R.D., N.Ryden., Xia,J., and Ivanov, J. 2005: Combined use of active and passive surface waves: *Journal of Environmental & Engineering Geophysics, Vol 10, No.3, 323 334*.

Peeples W. J., Sill W. R., May T. W., Ward S. H., Phillips R. J., Jordan R. L., Abbott E. A., and Killpack T. J. (1978) Orbital radar evidence for lunar subsurface layering in Maria Serenitatis and Crisium. *J. Geophys. Res., 83,* 3459–3468.

Penumadu,D. and C.B.Park. 2005. Multichannel analysis of surface wave (MASW) method for geotechnical site characterization: Proceedings of the Geo-Frontiers conference, Austin, Texas, January 23-26, 2005.

Pike R. J. (1977) Apparent depth/apparent diameter relation for lunar craters. *Proc. Lunar Sci. Conf. 8th,* pp. 3427–3436.

Ramos-Martinez, J., Ortega, A.A., and McMechan, G.A., 2000, 3-D seismic modeling for cracked media: shear-wave splitting at zero offset, Geophysics, 65, 211-221.

Rayleigh, L. (1885). "On waves propagated along the plane surface of an elastic solid." London Mathematical Society, 17, 4-11.

Richart, F.E. Jr., Hall, J.R., and Woods, R.D. (1970). Vibrations of soils and foundations, Prentice-Hall, Inc., Englewood Cliffs, New Jersey, 414p.

Rix, G.J., Lai, C.G., Orozco, M.C., Hebeler, G.L., and Roma, V. (2001b). "Recent advances in surface wave methods for geotechnical site characterization." 15th ICSMGE Conf. Schwab, F., and Knopoff,L. (1970). "Surface-wave dispersion computations." Bulletin of the Seismological Society of America,60, 321-344.

Rix, G.J., Stokoe II, K. H., and Roesset, J.M., 1991, Experimental study of factors affecting the Spectral Analysis of Surface Waves method, Research report 1123-5, Center for Transportation Research, The University of Texas at Austin.

Robert Benfield, Lori McDowell & Andy Kenst – Fall 2003; Geology and physiography of the UT Plant Science Farm Hydro Teaching Site.

Robinson, E.A., and Treitel, S., 1980, Geophysical Signal Analysis: Prentice-Hall, Inc. Yilmaz, O., 1987, Seismic data processing: SEG, Tulsa, Oklahoma.

Roesset, J.M., Chang, D.W., Stokoe II, K.H., and Auoad, M., 1990, Modulus and thickness of the pave-ment surface layer from SASW tests, Transp. Res. Rec., v. 1260, p. 53-63.

Ryden, N., C.B. Park, and P. Ulriksen, 2004, A framework for inversion of wavefield spectra in seismic non-destructive testing of pavements: Proceedings of the 2nd International Conference on Site Characterization (ISC-2), Porto, Portugal, September 19-22, 2004.

Ryden, N., Park, C., Miller, R., Xia, J., and Ivanov, J., 2001: High frequency MASW for non destructive testing of pavements: Proceedings of the Symposium on the Application of Geophysics to Engineering and Environmental Problems (this issue), Denver, Colorado, March 4-7, 2001.

Schwab, F. A., and Knopoff, L., 1972, Fast surface wave and free mode computations, in Bolt,B. A., Ed., Methods in computational physics: Academic Press, 87–180.

Scott R. F. and Zuckerman K. A. (1971) Examination of returned Surveyor III surface sampler. *Proc. Lunar Sci. Conf. 2nd,* pp. 2743–2751. Scott R. F., Carrier W. D. III, Costes N. C., and Mitchell J. K. (1971) Apollo 12 soil mechanics investigation. *Geotechnique, 21,* 1–14.

Sezawa, K., 1938a, Anomalous dispersion of elastic surface waves, Proc. Imp. Acad, v. 14, p. 246-249.

Sezawa, K., 1938b, Anomalous dispersion of elastic surface waves II, Bull. Earthq. Res. Inst., v. 16, p. 225-233.

Sheriff, R. E., 2002, Encyclopedic dictionary of applied geophysics: SEG Geophysical Reference Series No. 13, 4th Ed., Society of Exploration Geophysicists (SEG), Tulsa, Oklahoma, 429 pp.

Sheriff, R. E., and Geldart, L. P., 1985, Exploration seismology I: History, theory, and data acquisition: Cambridge Univ. Press.

Sheriff, R.E, and Geldart, L.P, 1983, Exploration Seismology, Vol.2. New York: Cambridge University Press.

Sheu, J.C., Stokoe,K. H., II, and Roesset, J. M., 1988, Effect of reflected waves in SASW testing of pavements: Transportation Res. Record, v. 1196, p. 51–61.

Shoemaker E. M. (1983) Asteroid and comet bombardment of the Earth. *Annu. Rev. Earth Planet. Sci., 11,* 15–41.

Stokoe, K. H., S. G. Wright, J. A. Bay, and J. M. Roësset, 1994, Characterization of geotechnical sites by SASW method. In: R.D. Woods, Editor, Geophysical Characterization of Sites, ISSMFE Technical Committee #10, Oxford Publishers, New Delhi (1994), 15-25.

Stokoe, K.H., and Santamarina, J.C. (2000). "Seismic-wave-based testing in geotechnical engineering." GeoEng 2000, November, Australia.

Stokoe, K.H., II, Wright, G.W., James, A.B., and Jose, M.R. (1994): Characterization of Geotechnical Sites by SASW Method, in Woods, R.D., Ed., *Geophysical Characterization of Sites: Oxford Publ.*

Stokoe, K.H., Wright, S.G., Bay, J.A., and Roesset, J.M., (1994). "Characterization of geotechnical sites by SASW method." XIII ICSMFE, New Delhi, India, Oxford & IBH Publishing, 15-25.

Sungsoo, Y. (2005). "Array-Based Measurements of Surface Wave Dispersion and Attenuation using Frequrncy-Wavenumber Analysis. PhD thesis 255p., Georgia Institute of Technology.

Taylor D. W. (1937) Stability of earth slopes. *Journal of the Boston Society of Civil Engineers.* Reprinted in *Contributions to Soil Mechanics 1925–1940,* pp. 337–386. Boston Society of Civil Engineers (1940).

Taylor D. W. (1948) *Fundamentals of Soil Mechanics.* Wiley, New York.

Taylor G. J., Warner R. D., Keil K., Ma M.-S., and Schmitt R. A. (1980) Silicate liquid immiscibility, evolved lunar rocks and the formation of KREEP. In *Proceedings of the*

Conference on the Lunar Highlands Crust (J. J. Papike and R. B. Merrill, eds.), pp. 339–352. Pergamon, New York.

Taylor L.A., and Taylor D.S. ((1997). Considerations for Return to the Moon and Lunar Base Site Selection Workshops. Journal of Aerospace Engineering, Vol. 10, No. 2, April 1997, pp. 68-79, doi http://dx.doi.org/10.1061/(ASCE)0893-1321(1997)10:2(68)

Telford, W.M., Geldart, L.P., Sheriff, R.E., and Keys, D.A., 1976, Applied Geophysics, Cambridge Univ. Press.

Thomson, W.T. (1950). "Transmission of elastic waves through a stratified solid." Journal of Applied Physics, 21, 89-93.

Tokimatsu, K., (1995). "Geotechnical site characterization using surface waves." Proc. Of the First Int. Conf. on Earthquake Geotech. Eng. Is-Tokyo '95, Tokyo, November 14-16, Balkema, Rotterdam, 1333 1368.

Tokimatsu, K., Tamura, S., and Kojima, H., 1992, Effects of multiple modes on Rayleigh wave dispersion characteristics, J. Geotech. Engrg., ASCE, v. 118, n. 10, p.1529-1543.

Terrestrial Analogue Sites (Space analogues). (2012). Retrieved on September 24, 2012, from http://en.wikipedia.org/wiki/Terrestrial_Analogue_Sites .

Tornabene, L.L., Moersch, J., Osinski, G.R., Lee, P., and Wright, S.P (2005). Spaceborne visible and thermal infrared lithologic mapping of impact-exposed subsurface lithologies at the Haughton impact structure, Devon Island, Canadian High Arctic: Applications to Mars: *Meteoritics and Planetary Science, Vol. 40, 1835-1858*.

Van der Pol, C., 1951, Dynamic testing of road constructions, J. appl. Chem., v. 1, July, p. 281-290.

Vaniman, D., Reedy, R., Heiken, G., Olhoeft, G.R., and Mendell, W. (1991): The Lunar Environment, *Lunar Source book., Cambridge University Press, Cambridge, pp. 27-60.*

Vidale, R.F., 1964, The dispersion of stress waves in layered media overlaying a half space of lesser acoustic rigidity, Ph.D. Thesis, Univ. of Wisconsin.

Viktorov, I.A (1957). Rayleigh and Lamb waves: physical theory and applications, Plenum Press, New York, 154p.

Watkins J. S. and Kovach R. L. (1973) Seismic investigation of the lunar regolith. *Proc. Lunar Sci. Conf. 4th,* pp. 2561–2574.

Watkins, J.S., Walters, L.A., and Godson, R.H., 1972, Dependence of in situ compressional wave velocity on porosity in unsaturated rocks: *Geophysics*, 37, 29-35.

Williams, T.P., and Gucunski, N., 1995, Neural networks for backcalculation of moduli from SASW test, J. Comp. In Civ. Engrg, ASCE, v. 9, n. 1, p. 1-8.

Wieczorek, M.A., Jolliff, B.L., Khan, A., Pritchard, M.E., Weiss, B.P., Williams, J.G., Hood, L.L., Righter, K., Neal, C.R., Shearer, C.K., McCallum, I.S., Tompkins, S., Hawke, B.R., Peterson, C., Gillis, J.J., and Bussey, B (2006): The Constitution and Structure of the Lunar Interior, *Reviews in Mineralogy and Geochemistry; Vol. 60;1, 221-364*.

Xia, J., R. D. Miller, and C. B. Park, 1999, Estimation of near-surface S-wave velocity by inversion of Rayleigh waves: Geophysics 64, 691–700.

Xia, J., R.D. Miller, C.B. Park, and G. Tian, 2003, Inversion of high frequency surface waves with fundamental and higher modes: *Journal of Applied Geophysics*, **52**, no. 1, 45-57.

Xia, Jhianghai., Xu, Yixian, Miller, R.D., 2007, Generating an image of Dispersive Energy by Frequency Decomposition and slant Stacking: *Pure and Applied Geophysics*, **164**, 1-16.

Xia, J., Miller, R.D., and Park, C.B., 1999, Estimation of near-surface shear-wave velocity by inversion of Rayleigh waves: *Geophysics*, v. 64, no. 3, p. 691-700.

Xia, J., Miller, R.D., and Park, C.B., 2000a, Advantages of calculating shear-wave velocity from surface waves with higher modes: [Exp.Abs.]: Soc.Expl.Geophys., p., **1295-1298.**

Yeluru, P., Baker, G., Park, C.B., and Taylor, L., 2008, New developments in seismic surface waves data acquisition and processing:Symposium on the Application of Geophysics to Engineering and Environmental Problems (SAGEEP 2008), Philadelphia, April 6-10, Proceedings on CD Rom.